

Technische Universität Dresden

Fakultät Naturwissenschaften und Mathematik
Institut für Angewandte Photophysik

**Metal Nanowire Networks as Transparent Electrode
for Small-Molecule Organic Solar Cells**

Dissertation
zur Erlangung des akademischen Grades
Doktor der Naturwissenschaften
(Dr. rer. nat.)

vorgelegt von
Christoph Sachse
geboren am 30. April 1984 in Rochlitz

Dresden 2013

Erstgutachter: Prof. Dr. Karl Leo

Zweitgutachter: Prof. Dr. Alexander Eychmüller

Tag der Einreichung: 09.09.2013

Tag der Verteidigung: 24.10.2014

Abstract

This work focuses on the development of metal nanowire networks for the use as transparent electrodes in small-molecule organic solar cells.

Broad adoption of organic solar cells requires inexpensive roll-to-roll processing on flexible, lightweight substrates. Under these conditions, traditional metal oxide electrodes suffer from significant drawbacks such as brittleness and cost. In contrast, metal nanowire networks provide properties more suitable for high-throughput processing and thus, are investigated here as an alternative. They combine the high-conductivity of metals with the advantage of optical transparency found in aperture-structured networks.

The process chain from nanowire deposition to cell integration is examined with silver and copper nanowire material. Two techniques are presented for deposition. While dip-coating is investigated in detail, including a discussion of the most important parameters, spray-coating is demonstrated as an alternative for large area applications. Since the nanowires are barely conductive after deposition, post-treatment steps are used to achieve a performance comparable to standard metal oxide films such as tin-doped indium oxide (ITO). The inherent roughness of nanowire electrodes is addressed by using a conductive polymer as a planarization layer. On top of optimized electrodes, small-molecule organic solar cells are deposited with a UHV thermal evaporation process. Completed cells are tested and performance is found to be comparable to the used standard transparent electrodes.

Additionally, a new approach to achieve aligned nanowire network structures is demonstrated. The additional degree of order is used to illustrate optical effects of silver nanowire networks. Furthermore, these aligned networks exhibit anisotropic conductivity. This effect is discussed and simulations are performed to reproduce the observations. The freedom of network design is used to achieve superior conductivity compared to standard random structures.

Kurzfassung

Im Fokus dieser Arbeit steht die Entwicklung von Metall-Nanodraht-Netzwerken für die Anwendung in transparenten Elektroden für organische Solarzellen. Eine breite Verwendung von organischen Solarzellen setzt eine kostengünstige Rolle-zu-Rolle Fertigung auf flexiblen und leichten Substraten voraus. Unter diesen Bedingungen leiden traditionell verwendete Metalloxid-Elektroden unter erheblichen Nachteilen, wie Brüchigkeit und Preis. Im Gegensatz dazu zeigen Metall-Nanodraht-Netzwerke deutlich bessere Eigenschaften und werden deshalb hier als alternative Elektroden untersucht. Die Netzwerke kombinieren die hohe Leitfähigkeit von Metallen mit einer hohen Transmittivität in Folge der netzwerkbedingten Apertur.

Die Prozesskette von der Nanodraht-Abscheidung bis zur Zellintegration wird für Silber- und Kupferdrähte untersucht. Zwei Techniken für die Abscheidung werden präsentiert. Ein Tauchverfahren wird detailliert untersucht und die zugehörigen Parameter werden diskutiert. Für große Flächen wird eine Sprühbeschichtung als Alternative aufgezeigt. Da die abgeschiedenen Netzwerke eine schlechte Leitfähigkeit besitzen, sind Nachprozessierungsschritte notwendig um gute Leitfähigkeiten im Bereich von üblichen Elektroden wie Indium-Zinn-Oxid (ITO) zu erreichen. Die Rauheit der Nanodraht-Elektrode wird mit Hilfe einer glättenden Polymerschicht behoben. Auf den optimierten Elektroden werden organische Solarzellen aus kleinen Molekülen in einem thermischen UHV-Prozess abgeschieden. Die Zellen werden getestet und zeigen Eigenschaften vergleichbar zu üblichen transparenten Elektroden.

Zusätzlich wird ein neuer Ansatz zur Herstellung von ausgerichteten Netzwerkstrukturen demonstriert. Der zusätzliche Grad an Ordnung wird für die Untersuchung von optischen Effekten an Silberdraht-Netzwerken genutzt. Weiterhin zeigen diese ausgerichteten Netzwerke eine anisotrope Leitfähigkeit. Dieser Effekt wird diskutiert und Simulationen werden durchgeführt, um die Beobachtungen zu verifizieren. Die Freiheit in der Netzwerkstruktur wird für eine Verbesserung der Leitfähigkeit genutzt.

Contents

1	Introduction	1
2	Organic Solar Cells	5
2.1	Solar Cells	5
2.2	Organic Semiconductors	9
2.2.1	Conjugated π -System and Organic Solids	9
2.2.2	Optical Properties and Charge Carrier Separation	11
2.2.3	Charge Carrier Transport	13
2.2.4	Doping	13
2.3	Organic Solar Cells	15
2.3.1	Structure of Organic Solar Cell Devices	15
2.3.2	Ohmic and Schottky Contacts	16
2.3.3	Optical Effects in Organic Solar Cells	18
2.3.4	Characteristics of Solar Cells	19
3	Transparent Electrodes	23
3.1	Transparent Electrodes and their General Requirements	23
3.2	ITO and Other Metal Oxides	25
3.3	Alternative Transparent Electrodes	27
3.4	Nanowire Electrodes	28
4	Fundamentals of Nanowire Networks	31
4.1	Percolation Networks	31
4.1.1	Cluster-Percolation and Conductivity	31
4.1.2	Percolation in Transparent Nanowire Electrodes	33
4.2	Metal Nanowires	35
4.2.1	Growth Mechanisms	35
4.2.2	Properties of Nanowire Structures	37

5	Experimental	45
5.1	Electrode Preparation	45
5.2	Solar Cell Preparation	50
5.3	Electrode Characterization	53
5.4	Solar Cell Characterization	57
6	Silver Nanowire Electrodes for Organic Solar Cells	59
6.1	Deposition	59
6.1.1	Dip-Coating	60
6.1.2	Influence of Air Humidity	64
6.1.3	Spray-Coating	67
6.2	Post-Treatment	70
6.3	Performance	72
6.4	Solar Cell Integration	73
6.4.1	Planarization	73
6.4.2	Structuring	77
6.4.3	ZnPc:C ₆₀ Solar Cells with Varied HTL Thickness	80
6.5	Conclusion	83
7	Copper as Nanowire Material	85
7.1	Synthesis and Deposition	85
7.1.1	Synthesis Approaches	85
7.1.2	Mohl-Synthesis	86
7.1.3	Wiley-Synthesis	88
7.2	Contact Issues, Post-Processing and Resulting Performance	89
7.2.1	Pressing	89
7.2.2	Annealing	90
7.2.3	Post-Processing with Various Nanowire Diameters	93
7.3	Solar Cell Integration	94
7.3.1	PEDOT:PSS Application	94
7.3.2	F ₄ ZnPc:C ₆₀ Solar Cell Deposition	96
7.3.3	Degradation	97
7.4	Conclusion	99
8	Anisotropic Nanowire Networks	101
8.1	Dip-Coating and Anisotropy	101
8.1.1	Network Generation and Anisotropy	101
8.1.2	Transmittance Spectra of Nanowire Networks	105

8.2	Resistance Effects and Application	112
8.2.1	Conductivity and Percolation Behavior	112
8.2.2	Electrical Simulation	115
8.2.3	Optimized Network Structure and Application	120
8.3	Conclusion	120
9	Conclusion and Outlook	123
	Bibliography	127
	List of Abbreviations and Symbols	144
	Danksagung	149

Chapter 1

Introduction

In the last 150 years fossil fuels like oil, gas and coal have powered the development of mankind. The huge amount of accessible (chemically-bound) energy allowed to realize more ideas than would ever be possible without. Although other causes had also an influence on the progress, cheap energy cannot be overrated. This fact explains the importance and the crucial role of energy in our daily lives. Though only 1/2 of the earth's population are consuming the majority of the exploitable energy, already 540,000 PJ per year are required to keep the society running.^[1] A huge share, about 200,000 PJ, is used to generate 18,500 TWh of electrical power^A since electricity is widely used and of high importance in many processes.^[1] Moreover, earth's population is growing and more people in developing countries become part of the excessive-consumption side. In consequence, the need for energy is growing continuously.^[2]

This situation is causing many challenges these days. 'Easily' extractable resources are shrinking which increases their related prices.^[3] Although higher prices lead to an evolution of extraction techniques and enable economical usage of 'new' deposits, the environmental impact is enormous (*e.g.* mining tar sands in the province of Alberta, Canada^[4]). Additionally, the widely discussed issue of climate change has to be emphasized and a drastic decrease in the emission of global greenhouse gases has to be imposed.^[5]

Solar energy could serve as an alternative

for energy sources with a high environmental impact. The irradiation energy of the

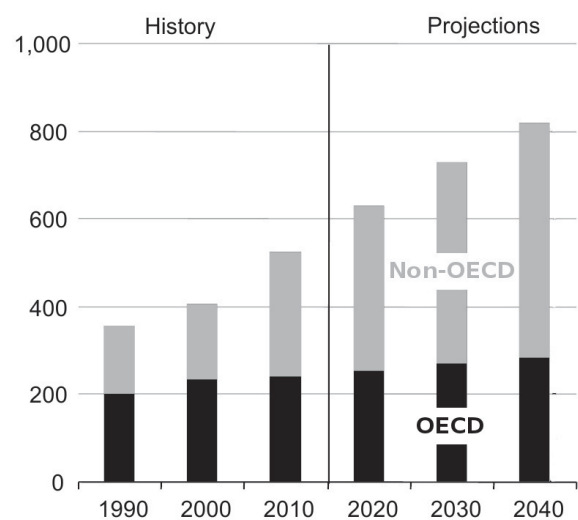


Figure 1.1: Development of the world energy consumption, 1990–2040 (quadrillion Btu).^[2]

^A Assuming 33% transfer efficiency from primary energy sources.

sun impinging on the earth ground in one hour is about as large as the total human consumption per year.^[6] Although this is just a theoretical value, the easily accessible potential of solar power is still significant and worth to be harvested, as calculations by the Desertec Foundation illustrate.^[7] The photovoltaic effect in solar cells provides the opportunity to generate advantageous electrical power directly from sunlight. In the last decade, the solar cell production showed a tremendous increase up to a yearly production capacity of about 60 GWp dominated by wafer-based silicon solar cells.^[8] However, growth is still originating mainly from subsidies and, regarding the environmental footprint (energy payback time: $\approx 1\text{--}4$ years^[9]), improvements are desirable.

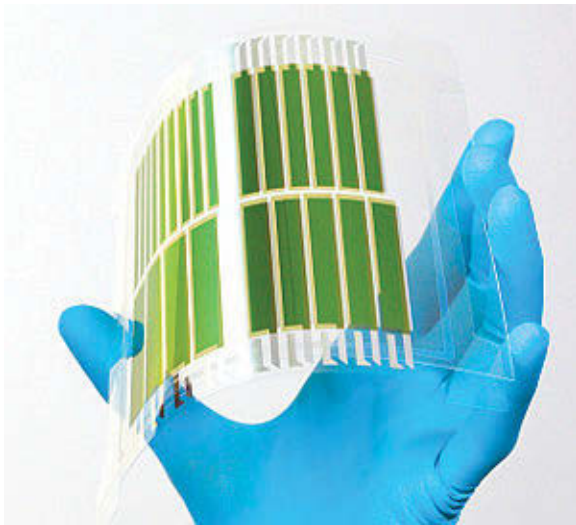


Figure 1.2: Organic solar cell on a flexible polymer foil. © Heliatek GmbH

One possible approach to improve the situation are thin film photovoltaic devices consisting of organic materials, so called organic solar cells (OSCs). They are characterized by low temperature processing and low material consumption, which is a result of the device thickness in the range of hundreds of nanometer. In this field large steps forward in terms of efficiency and lifetime have been achieved in the last 5 years. Today many researchers publish power conversion efficiencies around 10% while some even have reached the level of 12%.^[10,11] The diversity of organic chemistry is a great advantage for the future development of this photovoltaic type. Ongoing research will certainly lead to molecule design improvements followed by an increasing solar cell performance.

Although industrial production of OSCs was announced already years ago and start-up companies claimed that 10% efficiency and 5 years of lifetime would be sufficient to enter the market, the fast price reduction in the conventional silicon solar cell industry made the plan more challenging. This becomes even more relevant considering the higher prices of new approaches because of the small scale-production at the beginning. Therefore, the first products have to find niche markets and new unique applications in order to enter the already saturated solar cell market. An opportunity to stand out against wafer-based silicon technology might be the inherent flexibility of thin film solar cells. Despite delamination effects at the interfaces, the thin organic layers are indeed extremely flexible.

Towards flexible devices mainly challenges in the device periphery have to be solved. Apart from encapsulation issues, the transparent electrode is a crucial part of a solar cell when it comes to substrate bending. Commonly used metal oxide electrodes reveal a brittle nature so that causes cracks in the film and thus lead to device failure. In consequence, there is a great demand for flexible, low-cost transparent electrodes with sufficient performance.

In this thesis, metal nanowire networks are investigated as an alternative transparent electrode approach. This approach perfectly combines the high conductivity of metal with the high area aperture of a network structure.

This work addresses the whole process chain from nanowire synthesis and deposition towards device integration. Single steps are investigated more in detail to seek for improvements. In addition, the spatial structure of the network is examined and general properties are discussed.

Before focusing on the results, Chapter 2 to 4 provide the basic knowledge of this thesis. Chapter 2 serves as an introduction to the field of organic solar cells. Starting with a general description of the fundamental physics of photovoltaic devices and the basics about organic semiconductors, the operation principle and main characteristics of organic solar cells are mentioned. In Chapter 3 facts about transparent electrodes are gathered. General requirements are presented, followed by a view on the state-of-the-art technology and a discussion of alternative approaches including a literature review on nanowire electrodes. In Chapter 4 major points concerning nanowires and their networks are discussed. Along with the nanowire production, this includes sections on stick percolation, nanoscale conductivity, and nanoscale optics. As a first result, Chapter 6 illustrates the way to implement a silver nanowire electrode into an organic solar cell. The single steps from the deposition of the nanowires to the layer sequence of the solar cell are examined and enhancements are presented. In Chapter 7 the nanowire material silver is substituted with the alternative copper. The consequences regarding efficiency, handling and degradation are discussed. One focus is the oxidation behavior of copper which strongly influences the results. In Chapter 8 anisotropic AgNW networks are investigated. The special type of order allows a detailed examination of the optical effects of silver nanowire networks. Furthermore, the aligned structure results in an anisotropic conductivity. The effect is explained and simulations are presented to reproduce the behavior. In the last Chapter 9 the work is summarized followed by a short outlook.

Chapter 2

Organic Solar Cells

The following chapter provides selected basic knowledge to understand organic solar cells as a type of optoelectronic devices. In the first section the light conversion in solar cells is introduced in a more general and theoretical manner. The second section deals with the organic semiconductors as material of choice before structure and properties of an organic solar cell (OSC) are presented in the last section. In addition, this third section includes characterization parameters for the evaluation of solar cells.

2.1 Solar Cells

The photovoltaic effect, which allows the direct conversion of light into electricity, was first observed in the mid 19th century by A. E. Becquerel.^[12] It lasted almost 100 years until a physical explanation could be formulated with the up-coming wave-particle dualism at the beginning of the 20th century.

A detailed description of the theory causing light conversion and transport in solar cells can be found in the thesis of Riede^[13] based on the books of Würfel^[14] and Sze.^[15] The following paragraph provides a short summary based on these publications. Although this model is derived for inorganic semiconductors (SC), the part presented is also valid for their organic counterparts.

The scheme in Figure 2.1 illustrates the energy level diagram around the Fermi energy E_F for an intrinsic semiconductor without illumination. The bands represent regions with a large number of electronic states which are a direct result of the atomic binding situation^A. The conduction band E_C is related to the unoccupied anti-binding

^AThe constitution of the bands strongly depend on the material and its crystallinity. Therefore, pronounced deviations are observed between organic and inorganic semiconductors which are stressed in Section 2.2.

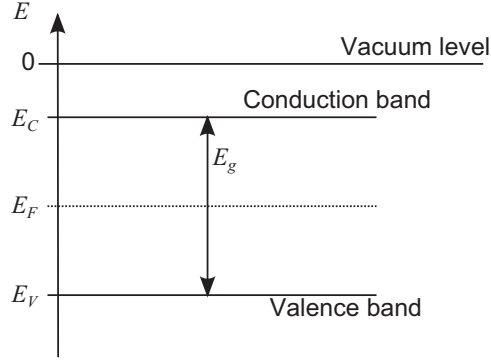


Figure 2.1: A simplified energetic scheme of the band structure near the Fermi level is depicted for an intrinsic SC. E_V , E_C and E_F are marked and the vacuum level (defines the zero point of the energy scale) is included for orientation.

states whereas the valence band E_V is formed by the occupied binding states. The Fermi level E_F is located between conduction and valence band within the state-free energy gap E_g .

In thermal equilibrium in the dark, the probability for an occupation of an electronic state is determined by the Fermi-Dirac distribution

$$f_F(E) = \frac{1}{\exp\left(\frac{E-E_F}{k_B T}\right) + 1} \quad (2.1)$$

whereas at the Fermi energy E_F a state has a probability of 1/2 to be occupied. E_g has to be much larger than $k_B T$ (at room temperature around 30 meV) up to a few eV to allow semiconductor behavior. Therefore, in an intrinsic (undoped) semiconductor, E_F is several $k_B T$ away from E_V and E_C . Thus, as an approximation the Fermi-Dirac distribution can be replaced by the Boltzmann distribution.

$$f_B(E) = \exp\left(-\frac{E - E_F}{k_B T}\right) \quad (2.2)$$

The carrier density for the electrons in the conduction band can then be calculated by combining Equation 2.2 and the density of states $D_e(E)$.

$$n = \int_{E_C}^{\infty} D_e(E) f_B(E) dE \approx N_C \exp\left(-\frac{E_C - E_F}{k_B T}\right) \quad (2.3)$$

The equation can be simplified with an effective density of states N_C . Likewise the missing electrons (referred as holes) in the valence band can be estimated with

$$p \approx N_V \exp\left(-\frac{E_F - E_V}{k_B T}\right). \quad (2.4)$$

In an intrinsic semiconductor, all electrons in the conduction band are causing holes at the valance level and therefore, the relationship $n = p = n_i$ (n_i is defined as intrinsic charge carrier density) is valid. As a result with inserting Equation 2.3 and 2.4 the Fermi energy is assumed to be

$$E_F = \frac{1}{2}(E_V + E_C) + \frac{1}{2}k_B T \ln \frac{N_V}{N_C}. \quad (2.5)$$

Hence, at low temperatures or with $N_C \approx N_V$ the Fermi level E_F is located in the middle of the band gap.

When the semiconductor is now illuminated with light of energy $\hbar\omega > E_g$ the equilibrium is lost. The photons are absorbed by the electrons and consequently excited to the conduction band. Thus, the same number of holes has to be generated in the valance band.

Under excitation, the Fermi level E_F can be split into two quasi-Fermi levels — $E_{F,C}$ focusing on the electrons with a corresponding charge carrier density

$$n = N_C \exp\left(-\frac{E_C - E_{F,C}}{k_B T}\right) \quad (2.6)$$

and the analog — $E_{F,V}$ for the holes with a density

$$p = N_V \exp\left(-\frac{E_{F,V} - E_V}{k_B T}\right). \quad (2.7)$$

The gap between electron and hole quasi-Fermi level

$$E_{F,C} - E_{F,V} = E_g + k_B T \ln\left(\frac{np}{N_C N_V}\right) \quad (2.8)$$

represents the maximum amount of energy which can be extracted from a semiconductor with excited electron-hole pairs. This energy is denoted as chemical potential — the semiconductor possesses potential energy. In consequence, an increasing illumination generates more pairs, the quasi-Fermi levels split and therefore, the potential for the extraction of energy is increased. Nevertheless, the splitting can never reach E_g due to the presence of recombination processes. The recombination rate \mathcal{R} per unit volume is described by the expression

$$\mathcal{R} = r(np - n_i^2) \quad (2.9)$$

whereas r is the recombination constant. The intrinsic charge carrier density n_i has to be subtracted, because only charge carrier densities exceeding the thermal equilibrium

value result in recombination.

As already mentioned, the absorbed light is stored as chemical potential energy in the semiconductor. In order to complete the solar cell, two contacts have to be attached for charge extraction. The contacts have to fulfill two requirements to avoid undesirable losses at the interface.

1. Each contact has to be permeable for only one type of charge carriers.
2. The Fermi levels of the contacts have to match the quasi-Fermi levels of the corresponding charge carrier type.

By considering these two requirements the quasi-Fermi level splitting depends only on the generation rate, the recombination rate and the extraction of charge carriers. Hence, the continuity equation for the stationary case can be written as

$$0 = \frac{\partial n}{\partial t} = \frac{\partial p}{\partial t} = \mathcal{G} - \mathcal{R} - \nabla \cdot j \quad (2.10)$$

The solution of this term for the ideal case (using Equation 2.8 and 2.9)

$$\nabla \cdot j = \mathcal{G} - rn_i^2 \left(\exp \left(\frac{E_{F,C} - E_{F,V}}{k_B T} \right) - 1 \right) \quad (2.11)$$

represents the fundamental relation of photovoltaics, plotted in Figure 2.2. The depicted curve illustrates the relation between the extracted charge carriers ∇j and the quasi-Fermi level splitting. The curve defines the amount of power, which can be extracted from the cell at a certain voltage. This curve is reflected by the current-voltage curve of a real solar cell during a voltage sweep, as it is discussed in Section 2.3.4.

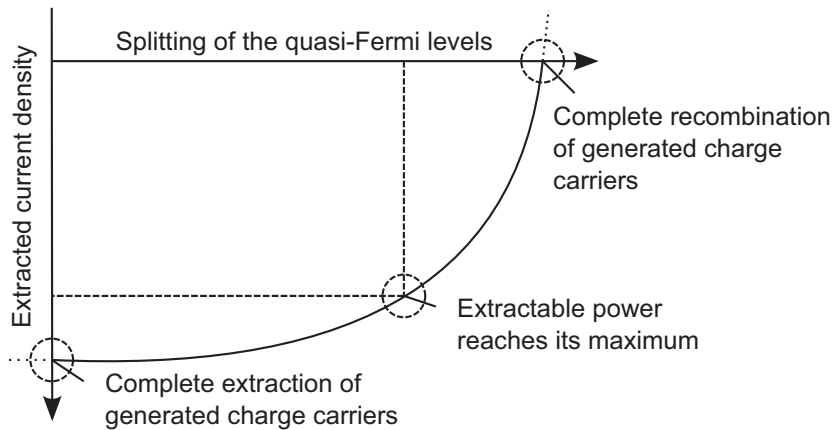


Figure 2.2: The graph resulting from Equation 2.11 is presented. A similarity to the current-voltage curve of a real solar cell can be observed, as visible in Figure 2.12 of Section 2.3.4.

2.2 Organic Semiconductors

In contrast to inorganic semiconductors, the organic counterparts consist mainly of carbon-hydrogen based molecules. The semiconductor behavior of organic materials was first observed about a century ago.^[16] While in the 60s the first conductive polymers were found,^[17] in the 70s this material class gained a larger attention with the doping investigations on polymers done by Heeger, Shirakawa and MacDiarmid.^[18] Over the last decades various conducting organic structures were found, among these were the “Small Molecules“, which represent the main field of research of the ‘Institut für Angewandte Photophysik‘ at the TU Dresden.

In the following sections, major aspects of this material class are presented. Additional information on that matter can be found, for instance, in several comprehensive books.^[19-21]

Organic semiconductors possess some structural characteristics which have a huge effect on the properties and therefore explain the deviations to inorganic semiconductors:

1. conjugated π -systems in the single molecule, which set the intra-molecular electronic properties,
2. weak binding between the molecules, which is responsible for the poor inter-molecular transport,
3. strongly bound electron-hole pairs as a result of light absorption, the so-called Frenkel excitons.

2.2.1 Conjugated π -System and Organic Solids

The electronic and optical properties of organic semiconductors are mostly dominated by the unique binding properties of carbon atoms. In an unbound state, the four valence electrons of a carbon atom have a standard electron configuration of $2s^2 2p^2$. However, due to energy minimization in a bound state, various molecular orbital configurations, so-called hybridizations, are possibly depending on the participating atoms and their orientation. The sp^2 -hybridization is demonstrated in Figure 2.3(a) with the sp^2 -orbital oriented in plane and the p_z -orbital perpendicular to the plane. In this configuration σ -bonds can be formed between the sp^2 -orbitals of the two atoms. The energy gap between an occupied binding and an unoccupied anti-binding level of σ -bonds is high. The value is far above visible light absorption, as presented in the energy level structure Figure 2.3(b). In addition, the two p_z -orbitals form a weaker, so-called π -bond. Here, the gap between unoccupied and occupied states is much smaller. Since the energies of the π -orbitals are located between the σ -orbitals, the anti-binding π^* -orbital is denoted

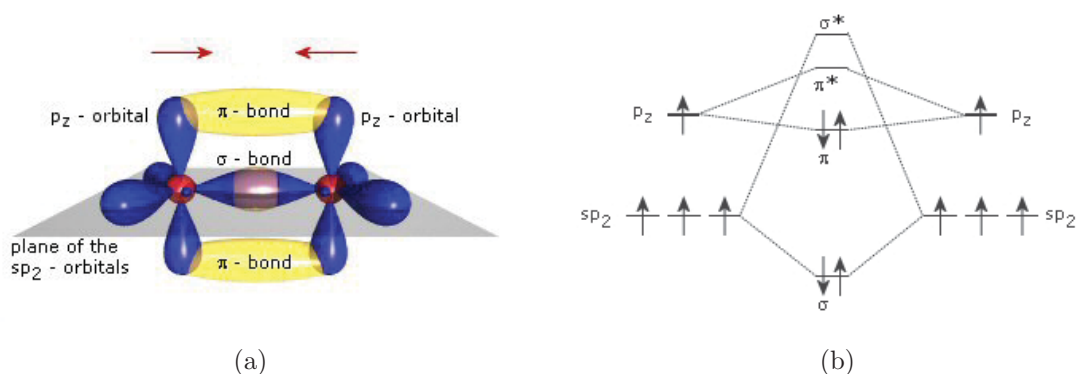


Figure 2.3: a) The different molecular orbitals (blue) of a sp^2 -hybridization are demonstrated for an ethene molecule. The p_z -orbitals form a π -bond. b) The corresponding energy diagram shows the energetic levels of the various bonding states. The π -levels are located between the σ -levels. Source: ‘Orgworld.de’^[22]

as lowest unoccupied molecular orbital (LUMO) and the occupied π -orbital as highest occupied molecular orbital (HOMO).

If more carbon atoms are linked together, depending on the orientation, the atomic p_z -orbitals might overlap and form a delocalized molecular π -orbital, denoted as conjugated π -system. With extension of the π -system, the gap between HOMO and LUMO level decreases. A well-known structure with conjugated π -system is the benzene ring, as depicted in Figure 2.4. Larger undisturbed π -systems are easily achieved, for in-



Figure 2.4: The hexagonal carbon based benzene ring is shown. Additionally, all molecular orbitals are depicted and particularly the delocalized conjugated π -system is marked in yellow. Source: ‘Orgworld.de’^[22]

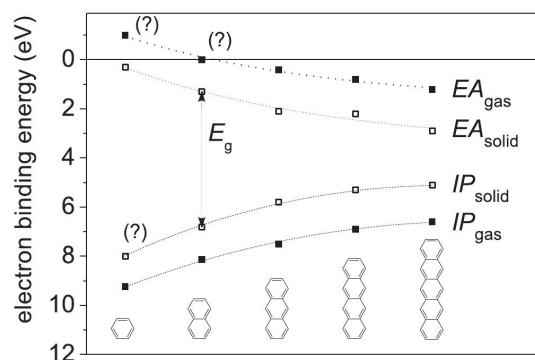


Figure 2.5: Electron affinity (EA) and ionization potential (IP) are shown for a bunch of organic molecules (from benzene to pentacene) with increasing π -system extension. The differences between gas and solid state are presented. Source: thesis of Falkenberg,^[23] based on Karl.^[24]

stance, by coupling benzene-like carbon rings, as demonstrated in Figure 2.5.

When a larger amount of organic molecules are clustering, a so-called organic solid is formed. Since organic solids typically consist of neutral molecules with full occupied

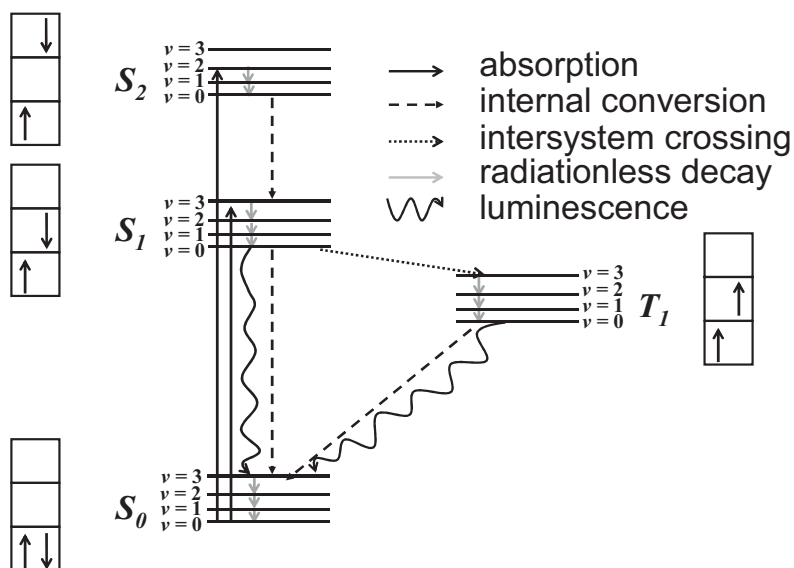


Figure 2.6: A Jablonski band diagram is depicted to illustrate the possible optical transitions between the different electrical and vibrational energy levels of an organic molecule.

molecular orbitals, the inter-molecular forces are weak. Such fluctuating van-der-Waals forces (*e.g.* dipole-dipole-bonding) are 1–2 orders of magnitude lower than typical intra-molecular covalent bondings.^[25] In consequence, the materials are characterized by a small dielectric constant, a low melting or evaporation temperature and a rather low conductivity compared to inorganic semiconductors.

Additionally, the low-force molecular interaction has a major effect on energy levels, absorption, charge carrier separation and charge carrier transport. In the following two sections these consequences are briefly discussed.

2.2.2 Optical Properties and Charge Carrier Separation

As the inter-molecular forces are weak, the optical properties are dominated by the single molecules. Thus, optical interactions with the semiconductor can be illustrated in a Jablonski diagram, depicted in Figure 2.6. In this graph, the existing energy states of a molecule and the possible transitions, which either can be radiative or non-radiative, are marked.

In the equilibrium without illumination, the molecule is located in the ground singlet state S_0 ($v = 0$). Incident light with sufficient energy leads to the absorption of photons which excite the molecule to a higher state, for instance the first excited singlet state S_1 . The time-scale of this process is within the range of 10^{-15} s and the

spin remains unchanged. Due to the Franck-Condon-principle^B, an electrical transition typically ends in a state of higher vibrational excitation ($v > 0$). The vibronic state decays non-radiative within 10^{-12} s in an internal conversion process to $v = 0$. Since the decay occurs quickly after transition and much faster than the lifetime of the excited state, vibrational losses cannot be avoided. Subsequently, the molecule can, from state S_1 ($v = 0$), return to S_0 ground state by a radiative fluorescence process (typically within 10^{-9} s to 10^{-7} s) while keeping its spin constant. Transitions from singlet S_n to triplet states T_n are forbidden in the ideal case, due to non-allowed spin transition. However, the presence of spin-orbit coupling^C increases the probability of such an incident. In this case an inter-system-crossing from an excited singlet to a triplet state can be observed. The decay from such a triplet state T_n to ground state S_0 is named phosphorescence, and due to low transition probability, the state has a rather long lifetime in the range of 10^{-6} s up to hours. A direct excitation from ground singlet to triplet (not depicted) is unlikely because of the small transition matrix element. Finally, it has to be mentioned that the radiative emission always has to compete with radiation-less internal conversion processes.

Because of the strong overlap between the wave-function of the ground state and the lowest excited state in the $\pi \leftarrow \pi^*$ transition,^[26] in general, the absorption coefficient α of organic semiconductors

$$\alpha = \frac{4\pi k}{\lambda} \quad (2.12)$$

is high with values larger than 10^{-5} cm^{-1} .^[27,28] As a result thin layers < 100 nm absorb already a large share of the light. Therefore, organic absorbers are qualified for the application in solar cells.

However, in contrast to inorganic semiconductors, the absorption of a photon does not result in free charge carriers. Instead, a Frenkel-like exciton is generated — an uncharged and still bound electron-hole-pair.^[29] As the charge carriers are not yet separated, they would recombine after a short lifetime and the molecule would relax to the ground state. The neutral exciton stays unaffected by electrical fields and therefore the corresponding diffusion lengths are rather small in the range of ≈ 3 –70 nm.^[26–28] In order to obtain free charge carriers, a separation junction is necessary which can be realized by a donor-acceptor interface (heterojunction interface). Because of energy level differences (HOMO, LUMO) of the materials, hole and electron are separated from each other, as is further stressed in Section 2.3.

^BThe electrical transition always takes place between states of large wave-function overlap.

^CThe spin-orbit coupling is more pronounced for molecules including heavy metals or showing a strongly twisted out-of-plane structure.

The separation process from a bound excitonic state towards free charge carriers is accompanied by various loss mechanisms. Details on these mechanisms can be studied in the works of Brütting or Schwörer.^[19,21]

2.2.3 Charge Carrier Transport

Subsequently, the free charge carriers can drift and diffuse to the respective electrode. This process (resulting in a current density j) is affected by the charge carrier mobility μ and the electrical field F , as determined by

$$\vec{j} = e\mu n\vec{F} + eD\vec{\nabla}n \quad (2.13)$$

with the elementary charge e , the charge carrier density n and the diffusion constant D .

The charge carrier transport in inorganic SCs can be described by band transport, which is a consequence of the strong inter-atomic bonding and the rigid structure.

As aforementioned, the inter-molecular forces in organic semiconductors are, in contrast to inorganics, extremely weak. Therefore, pure band transport just occurs in highly ordered structures like organic crystals. However, due to the weak orbital overlap compared to inorganic structures, the transport states are rather narrow and the mobilities are low with values in the range of 1 to 10 cm²/(V s).^[21,30]

It is noteworthy that organic devices are mainly consisting of amorphous materials. Under these conditions the interaction is too small for band-like transport. Instead of that, the transport can be described as a hopping process. The dependency can be summarized to

$$\mu(F, T) \approx \exp(-\Delta E_A/k_B T) \cdot \exp(\beta\sqrt{F}/k_B T) \quad (2.14)$$

illustrating the influence of the temperature T and electrical field F . Typical mobilities for amorphous organic semiconductors at room temperature are ranging from 10⁻⁶ to 10⁻³ cm²/(V s),^[21] whereas Si reaches 1 cm²/(V s)^[31] in amorphous phase.

2.2.4 Doping

Conductivity is defined as the product of mobility, elementary charge e and the number of charge carriers n .

$$\sigma = \mu \cdot n \cdot e \quad (2.15)$$

Since the number of charge carriers in an intrinsic organic SC is orders of magnitude below that of inorganic materials, low conductivities are observed in pure organic materials.^[21,31] Therefore, charge carrier transport of more than 100 nm is inefficient.

In order to realize layers with better transport properties, charge carrier density has to be increased^D. One possible approach is the (electrochemical) doping^E, which can be achieved by introducing single atoms, Lewis-bases or acids, and even larger organic molecules. In small-molecule organic layers the latter results in stable doped films, since the molecule size hinders diffusion and therefore the degradation process.^[31]

Figure 2.7 is demonstrating the energetic level scheme for n- and p-doping without (a) and with (b) thermal activation to illustrate the mechanism. Doping can increase

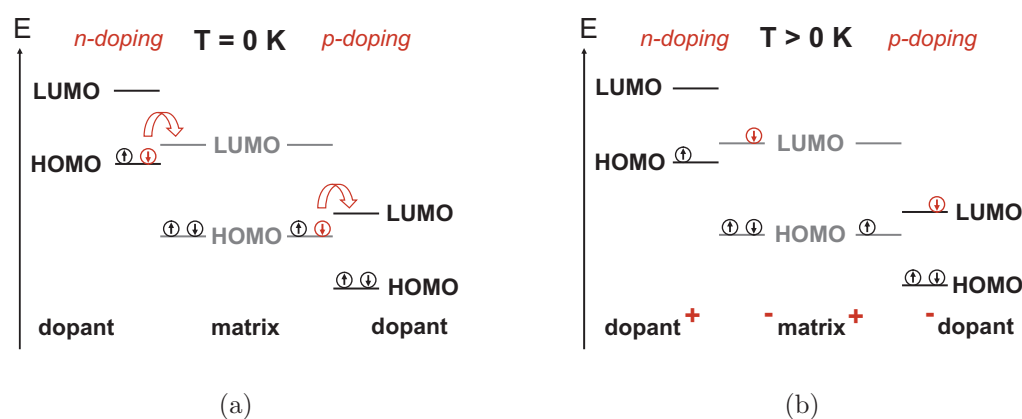


Figure 2.7: In order to dope a matrix material, a corresponding dopant has to be introduced which allows energy level matching. The HOMO of the n-dopant has to match the LUMO of the matrix and the p-dopant LUMO fits to the matrix HOMO. The left figure a) demonstrates the $T = 0$ case, where the electrons are still bound to the molecule of their origin. Figure b) shows the real electron distribution for $T > 0$.

the conductivity of amorphous organic films by orders of magnitude to values up to 10^{-2} S/cm^[31–33] and for certain materials like C₆₀ even above 1 S/cm.^[34]

The mentioned high conductivity provides more freedom for device design. For instance, transparent transport layers for optimizing optical properties and exciton-, hole- or electron blocking layers can be integrated. Furthermore, doping is important for a barrier-free contact between semiconductor and electrode contact, as explained in Section 2.3.2.

^DSince the mobility depends mainly on the material type and the crystallinity, it cannot be easily influenced.

^EAs an alternative, the charge carrier density can be increased by injection from the contacts, photo-generation or field-effect doping.

2.3 Organic Solar Cells

2.3.1 Structure of Organic Solar Cell Devices

Since Tang published the first reasonably efficient organic solar cell in 1986^[35] great strides forward have been made in this field. In the last decade, an impressive increase in cell efficiency to more than 10% has been achieved.^[11]

In general, organic solar cells are classified as thin film devices. In contrast to the first organic cell, for which only two layers were necessary, today's OSCs consist of many thin layers in the range of a few to hundreds of nanometers. The typical structure of a single junction organic solar cell is depicted in Figure 2.8.

Although the structure of today's OSC is much more complex, Tang's cell — which consists of an electron donor and acceptor layer — already demonstrates the crucial mechanism enabling the harvesting of light generated free charge carriers from organic absorbers. Besides mobility, doping concentration and absorption behavior, the necessity of exciton separation represents the main difference compared to inorganic solar cell approaches.

As aforementioned, the absorption of a photon with appropriate energy results in a bound exciton state. Because of the properties of organic materials, high energies far above $k_B T$ are necessary to separate the exciton and generate free charge carriers. The separation is achieved *via* the donor-acceptor heterojunction interface introduced by Tang.^[35] Therefore, the donor-acceptor layer is often denoted as active layer because both absorption and exciton separation takes place in this layer.

Unfortunately, the exciton diffusion length is small compared to the absorption length of the light. Since the exciton has to reach the interface within the diffusion length (see Figure 2.9), instead of utilizing a planar structure (A), a mesh structure (B) would be ideal. Such nanoscale structures are complicated to produce and thus a blend structure denoted as bulk heterojunction (BHJ) structure (C) is used instead. With this approach the layer thickness can be enlarged whereas the exciton travel distance stays small.

The donor-acceptor stack is extended in order to further optimize the device. Layers to block the excitons or to minimize the material diffusion can be added. In addition, a large efficiency impact can be obtained by the introduction of hole and electron transport layers (HTL/ ETL) which provide more freedom in stack design, as presented in Figure 2.8. Since the transport layers are produced by doping, these devices are named pin (p-doped — intrinsic — n-doped) devices.^[36] In order to allow transport without energy barriers or energetic losses at the absorber interface, the energy levels of the transport layer and the respective active material have to match properly, as is

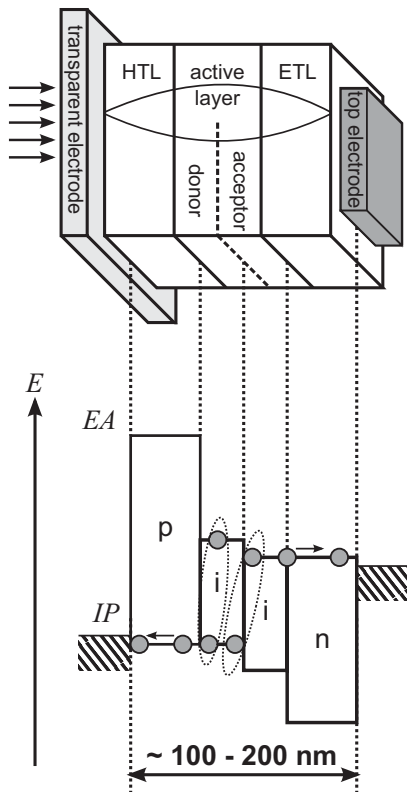


Figure 2.8: The standard structure of a pin organic solar cell is shown with its corresponding energy level scheme.

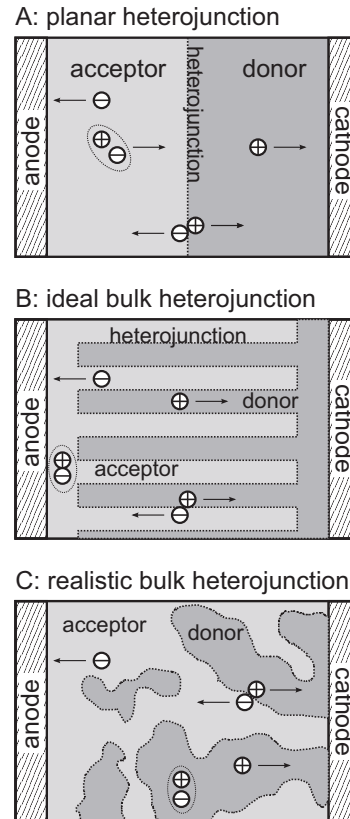


Figure 2.9: Donor-acceptor OSC with planar heterojunction (A), ideal mesh junction (B) and bulk heterojunction (C).

presented in the energy level scheme of Figure 2.8. Otherwise barriers occur or energy losses are observed, since the transport levels set the energy levels of the solar cell.^[37] If transport materials are highly transparent^F ($E_g > 3\text{eV}$), they can be applied as window-layers to tune the optics inside the cell, as further addressed in Section 2.3.3. In tandem devices the transport layers are used as recombination contact to achieve a serial connection between the subcells.^[38] Finally, because of the high doping concentration, they can be used to generate a proper metal-semiconductor contact as mentioned in the following Section 2.3.2.

2.3.2 Ohmic and Schottky Contacts

As already indicated in Section 2.1, highly conductive contacts (anode and cathode) have to be attached in order to extract the charge carriers. Since the required semi-permeability is fulfilled by the donor-acceptor heterojunction (electrons and holes are separated spatially), only the level alignment of the contacts remain an important

^FIf they are not transparent parasitic absorption leads to minimization of the photo current.

requirement. For instance, in the energy scheme of Figure 2.8 the work function matches properly even without the introduced transport layers^G. Nevertheless, finding appropriately matching materials is, in general, rather complicated. The work function of the active layer is fixed according to the utilized materials^H. Thus, an appropriate contact material has to be found. However, due to other requirements, the freedom is rather limited. Moreover, the work function of the conductor (*e.g.* ITO) might depend on the processing parameters, and degradation might affect the reproducibility.^[39] In order to avoid such instabilities and tuning the work function on purpose, injection or extraction interlayers (*e.g.* PEDOT:PSS,^[40] MoO₃,^[41] TiO₂^[41] or self-assembled-monolayers^[42]) are typically introduced.

As an alternative, the doped transport layer approach with pin cell structures offers a possibility to circumvent these contact problems.

If a doped SC is brought into contact with a conductor, at equilibrium the Fermi-level has to be equal all over the connected system. Depending on the work function position, charge carriers diffuse from one to another material until the diffusion is balanced by an opposite force (electrical field induced by charging effect). As a consequence band bending, charge carrier depletion and accumulation can be observed. A detailed description of the physics at the organic-conductor interface can be found in the thesis of Tress.^[43] In general, three distinct conditions exist for the interface between conductor and doped semiconductor, which are depicted for the n-doped case in Figure 2.10.

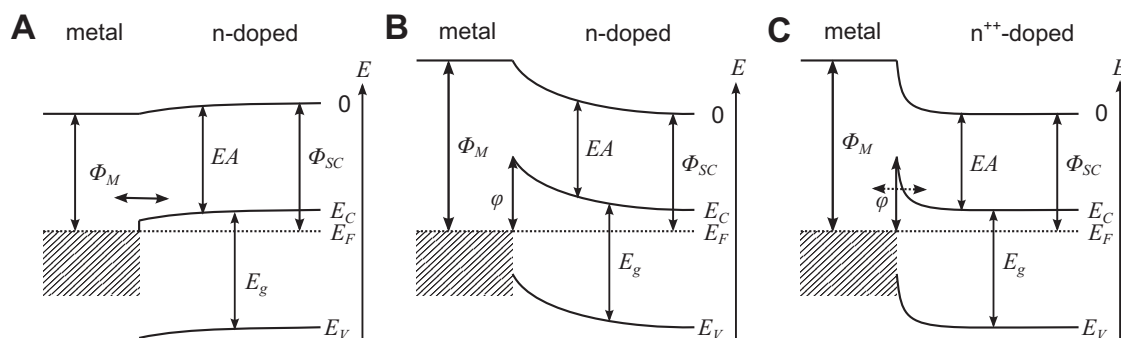


Figure 2.10: Different cases for a conductor-semiconductor contact are presented. For the n-doped case the formation of an ohmic (A), Schottky (B) and ohmic tunneling contact (C) is illustrated with the help of an energy level diagram.

^GIt is noteworthy that the transport layer often also serves as exciton blocking layer (hinders exciton quenching). In particular, for bulk heterojunction systems the simplified system would suffer strong losses.

^HThe active materials are optimized regarding transport and absorption properties. A change of the work function would counteract these purpose.

In case (A) the work function of the semiconductor (defined as the distance between Fermi and vacuum level) is large compared to the work function of the conductor ($\Phi_M < \Phi_{SC}$). Charge carrier diffusion leads to a junction which is rich in electrons. Therefore, the contact exhibits an ohmic behavior with a rather small voltage drop and is denoted as ‘ohmic contact’.

In the opposite case (B) ($\Phi_M \gg \Phi_{SC}$), the charge carrier re-distribution results in a band bending accompanied by the formation of a carrier depletion region in the semiconductor and a Schottky barrier is formed. The depletion zone in the SC leads to a rectifying behavior which can hinder the charge carrier extraction. Hence, this contact type has to be avoided in order to achieve a proper connection to the cell.

Since the doping concentration of the semiconductor influences the length of the depletion region and the band bending, a narrow barrier can be achieved at high doping concentrations. A short depletion zone increases the probability for charge carrier tunneling through the barrier. As a result, many carriers can pass the barrier and an ohmic behavior is observed (see Figure 2.10(C)). This case provides the opportunity to gain reliable contacts in the solar cell by increased doping. Therefore, highly doped transport layers are applied in this thesis to achieve a sufficient contact. As a consequence, the work function of the electrode metal is less important and, thus, not further discussed.

2.3.3 Optical Effects in Organic Solar Cells

An efficient incoupling and light-path manipulation is of great importance for all solar cell types. The various effects are illustrated in Figure 2.11.

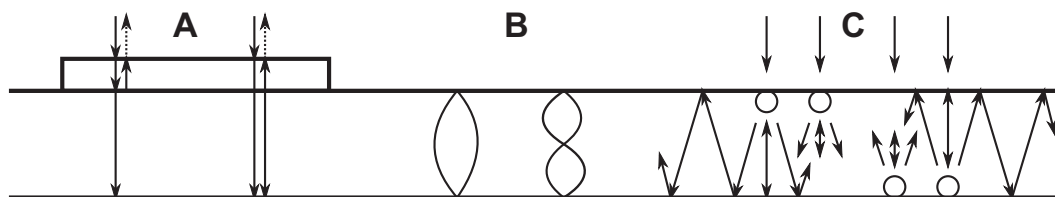


Figure 2.11: Optical effects of an organic solar cell — A: anti-reflection coating, B: cavity behavior, C: scattering.

Scheme (A) shows the principle of an anti-reflection coating. The left case is generally applied for thicker devices (cell thickness above the coherence length of sun light). With a correctly chosen coating thickness, the reflected light exhibits destructive interference and therefore the reflection is minimized. In thinner devices (right case) the whole cell can be optimized accordingly.

Organic solar cells are in general just about 100 to 400 nm thick, which is below the

wavelength and coherence length of sun light. Therefore, standing waves and a cavity behavior (B) can be observed. In particular, for highly reflective electrode systems (i.e. metals) this effect can dominate the light conversion performance. The transport layers (see Section 2.3.1) can be used to tune the cavity size, as shown in Figure 2.8. Thus, the spatial location of the field maxima can be shifted towards the absorption layer. The same procedure is used to avoid parasitic absorption in layers apart from the active area. For instance, the field intensity can be lowered at the position of the transparent metal electrode.^[44] The microcavities are preferentially and widely used in OLEDs for improving outcoupling of certain wavelengths.^[45]

In addition, light absorption can be enhanced by the elongation of the light path (C) in the absorber region. Scattering structures directly elongate the light path in the cell.^[46] Moreover, at large scattering angles and for layer stacks with properly adjusted refractive indices, light might couple to waveguide modes in the cell. This light, so that captured in the absorption region, is completely absorbed and high conversion efficiencies can be observed even for weak absorption coefficients.^[47]

2.3.4 Characteristics of Solar Cells

Current-Voltage Characteristic

Connecting an illuminated solar cell to an electrical circuit and performing a bias-voltage sweep a typical current-voltage curve (jV), as demonstrated in Figure 2.12, can be observed. The exponential behavior is fundamental, as demonstrated in Section 2.1. The graph in Figure 2.2 reveals a similar shape although derived from a more theoretical point of view. This fact illustrates the strong connection between the jV behavior and the inner physics of the cell. Therefore, the jV-curve is the major characterization method and in combination with various measurement conditions much information can be collected from these curves.

Furthermore, some key parameters — marked in Figure 2.12 — are defined to characterize and evaluate solar cells.

Without illumination (dotted line) the solar cell shows a curve with $J_{ph} = 0$. Being illuminated, extra charges ($J_{ph} > 0$) are generated and the curve shifts downwards (solid line). The main parameters can directly be obtained from this graph. The open-circuit voltage V_{oc} and the short-circuit current j_{sc} are represented by the intersections with the j- and the V-axis, respectively. The extractable power P is visible in the 4th quadrant of the jV-curve as a product of $j \cdot V$. Thus, the power value is always extracted in negative direction and $|P|$ has to be used. The largest amount of power can be extracted at the maximum power point P_{mpp} with the corresponding V_{mpp} and j_{mpp} .

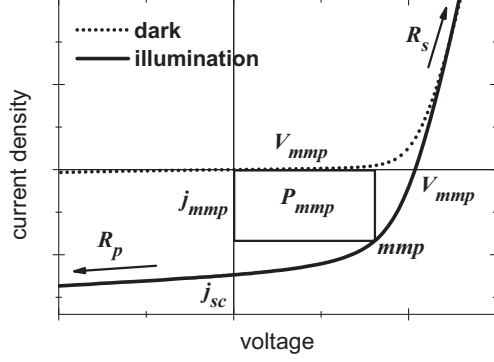


Figure 2.12: Current-voltage curve of a solar cell in the dark (dotted) and under illumination (solid). All important key-parameters are marked and the black rectangle demonstrates the maximum extractable power.

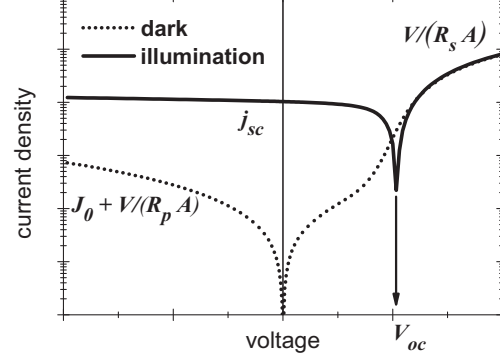


Figure 2.13: The semi-logarithmic plot of the jV-curve is presented with all parameters, which can be determined from this graph.

The ratio between P_{mpp} and the product of the maximum values $V_{oc} \cdot j_{sc}$ is defined as fill factor (FF).

$$FF = \frac{V_{mpp} \cdot j_{mpp}}{V_{oc} \cdot j_{sc}} \quad (2.16)$$

The power conversion efficiency η represents the ratio between the highest extractable power at the maximum power point P_{mpp} and the incoming illumination power P_{ill} .

$$\eta = \frac{P_{mpp}}{P_{ill}} = FF \cdot \frac{V_{oc} \cdot j_{sc}}{P_{ill}} \quad (2.17)$$

As illumination power P_{ill} typically an intensity of 1 sun with 100 mW/cm^2 and an AM1.5 spectrum^I is used for validation.

Serial and Parallel Resistance

The jV-curve can be modeled with an equivalent circuit, which roughly matches the cell behavior. The simplest system, which consists of a parallel connected diode and a current source, is already sufficient for the illustration of the exponential incline. The model is described by the corresponding Schottky Equation 2.18

$$j = J_0 \left(\exp \left(\frac{eV}{n_1 k_B T} \right) - 1 \right) - J_{ph} \quad (2.18)$$

with saturation current J_0 , ideality factor n_1 and photo current J_{ph} .

However, this picture is far too simple and a solar cell is affected by various other

^IThe AM1.5 spectrum corresponds to the black-body irradiation, originating from the sun after passing $1.5 \times$ the atmosphere (air mass) of the earth.

parameters. For instance, the parallel (R_p) and series resistance (R_s) have a strong influence on the shape. Therefore, both parameters are integrated into the equivalent circuit (see Figure 2.14) and

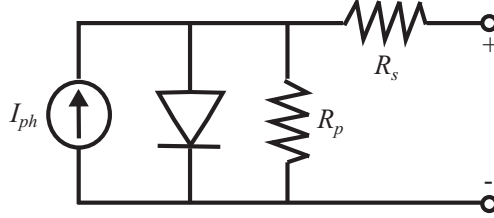


Figure 2.14: Equivalent circuit for a simple solar cell extended with parallel (R_p) and series resistance (R_s) contributions.

Equation 2.18 is extended to

$$j = \frac{1}{(1 + (R_s/R_p))} \left(J_0 \left(\exp \left(\frac{V - jR_s A}{n_1 k_B T / e} \right) - 1 \right) - \left(J_{ph} - \frac{V}{R_p A} \right) \right). \quad (2.19)$$

In addition to the resistance in the solar cell material, the electrode can have a large impact on both parameters. The series resistance R_s represents losses in the current transport (*e.g.* at the electrodes) due to a high resistance in the device. It is dominant at higher voltages and lowers the slope. The parallel resistance R_p is infinite for the ideal case. If the resistance is decreasing (*e.g.* due to leakage) the resistance shows an increased slope for small and negative voltages. Both, R_p and R_s affect the FF and thus have a strong influence on the efficiency.

Plotted in a semi-logarithmic graph, the jV -curve provides direct access to both resistance values, as demonstrated in Figure 2.13.

As an alternative, the fit of the slope for large positive and negative voltages in Figure 2.12 can also serve as evaluation parameter. Moreover, in this work the saturation value Sat is used for R_p evaluation, whereas the value is defined as $Sat = j(-1V)/j(0V)$.

Spectral Response and External Quantum Efficiency

The spectral response SR represents the ratio of the extracted electrical power *vs.* the incoming power depending on the wavelength.

$$SR(\lambda) = \frac{j_{sc}(\lambda)}{P_{ill}(\lambda)} \quad (2.20)$$

It can be obtained by illuminating with a wavelength range ($\lambda, \lambda + \Delta\lambda$) and measuring the corresponding current. More usual is the external quantum efficiency (EQE)

$$EQE(j_{sc}, \lambda) = \frac{j_{sc}(\lambda)}{e \cdot N_{ph}(\lambda)}, \quad (2.21)$$

which describes the ratio of electrons extracted per incoming photon *vs.* number of incoming photons N_{ph} for a specific wavelength range. When integrating the currents over all wavelengths and assuming an AM1.5 spectra the short circuit current

$$j_{sc}^{SR} = \int_0^{\infty} SR(\lambda) \cdot E_{AM1.5}(\lambda) d\lambda \quad (2.22)$$

should be achieved.

Among the interesting insight (spectral resolved current contribution), which can be reached with the help of this data, the method is crucial for calculating the correct efficiency value η for a solar cell. The intensity of the AM1.5 sun simulator spectrum is determined with a calibrated silicon reference diode, which is used to set the intensity to 100 mW/cm^2 . However, the artificial sun-simulator spectrum differs from the AM1.5 spectrum of the real sun. Since the calibration is carried out with a silicon reference cell, deviations in light absorption to the organic test cell would lead to an over or under-estimation of the cell performance. Thus, a spectral mismatch value

$$M = \frac{\int_0^{\infty} SR_{ref}(\lambda) \cdot E_{AM1.5}(\lambda) d\lambda \cdot \int_0^{\infty} SR_{test}(\lambda) \cdot E_s(\lambda) d\lambda}{\int_0^{\infty} SR_{ref}(\lambda) \cdot E_s(\lambda) d\lambda \cdot \int_0^{\infty} SR_{test}(\lambda) \cdot E_{AM1.5}(\lambda) d\lambda} \quad (2.23)$$

has to be determined for both cells before the power conversion efficiency can be calculated.

Chapter 3

Transparent Electrodes

This chapter serves as an introduction to the field of transparent electrodes. Starting with a variety of possible applications, the criteria for the implementation in solar cells are the main subject in the first section. The desired requirements are provided and figure of merit (FoM) models are presented for evaluation. The second section demonstrates the state of the art techniques, its problems and possible material substitutions. Subsequently, various alternative approaches are compared before, in the last part, nanowire networks are introduced as promising solution including a short literature review.

3.1 Transparent Electrodes and their General Requirements

Transparent electrodes are widely used in various industrial products where transparency and conductivity have to be combined. As examples switchable windows, display technologies, transparent electronics, lighting and photovoltaic applications can be mentioned. This work focuses on the latter one.

In general, the following paragraph is valid for all thin film solar cells. Since the used active solar cell materials are barely conductive, additional electrodes are necessary to extract charge carriers, whereas at least one has to be transparent to couple light into the optoelectronic device, as shown in Figure 2.8.

At first sight it seems to be simple — a material with high conductivity and transmittance represents a perfect transparent electrode. Unfortunately, tackling the required combination of sufficient current transport and visible light transmission is a challenging task, since both affect each other in a negative way.

In order to compare electrode systems concerning their performance, a few evaluation

models have been suggested in the past.^[48-51] The quotient of conductivity and absorption $\sigma/\alpha = \ln T_{\text{total}}/R_{sh} \approx 1/(R_{sh} \cdot A_{abs})$ with sheet resistance R_{sh} , absorbance A_{abs} and transmittance T_{total} is widely used in the community due to the simplicity.^[48] Nevertheless, the large number of alternative FoMs demonstrate how complicated it is to reduce the electrode to such a simple state. The σ/α -FoM is only valid for a particular electrode configuration (thickness, resistance, wavelength) and is therefore rather limited to deduce general statements concerning electrode performance. A more general FoM was suggested by De *et al.*^[52] based on theory of Dressel and Grüner.^[53] In this model the transmittance T_{total} (for a specific wavelength or wavelength range) is plotted against sheet resistance R_{sh} and by fitting with

$$T_{\text{total}}(\lambda) = 1 + \frac{188.5}{R_{sh}} \frac{\sigma_{Op}(\lambda)}{\sigma_{DC}} \quad (3.1)$$

the ratio of optical conductivity to electrical DC conductivity σ_{Op}/σ_{DC} serves as figure of merit.^[52] This performance value describes a transparent electrode material independent of thickness. It only depends on wavelength.

In order to choose an appropriate transparent electrode, the solar cell device structure has to be considered. For instance, the wavelength range for light conversion is important. Highly efficient OSCs demand for a high transmittance over the whole visible spectra and even values up to the NIR have to be taken into account^A. The required resistance depends on the active area size and the driving currents. For large areas with module size, the sheet resistance has to be $< 1 \Omega/\text{sq.}$ to neglect power losses.^[54] However, at sufficient transmittance such values are still far beyond available transparent electrodes and will not be reached within mid term research projects. Thus, current collecting bars are deposited as an alternative to decrease the long range resistance^[55,56] or the cells are split into smaller serial connected cells to gain a decreased current at higher voltage, which decreases the thermal power losses following $P = R \cdot I^2$. In all these cases shadowing effects or area losses have to be considered and a trade-off is needed regarding the transparent electrode performance. With typical technologies pixel sizes of 0.5–2 cm (or pitch of the grid) with sheet resistances of 10–40 $\Omega/\text{sq.}$ are industrial standard and guaranteeing acceptable losses.

Moreover, secondary requirements exist to obtain a suitable transparent electrode film. Meeting industrial demands, processability plays a major role. There is a large number of different deposition techniques even for the same material class. It is crucial

^AIn most of the publications an averaged transmittance value between 400 nm and 800 nm is used or the value is additionally weighted with the sun AM1.5 spectrum.

that a reliable outcome is guaranteed and that the process fits to the surrounding infrastructure of the whole solar cell production. Connected to the processability also costs have to be considered. Thus, fast deposition with a small step number at low temperatures is preferred. The goal regarding cost efficiency is a roll-to-roll machine in combination with flexible polymer or metal foil substrates.

Apart from production, material resources and related costs are important, since solar cells meant to be installed on large areas. If the resources of the used materials are strongly limited as for some metals or semiconductors, scaling up to GW output will cause material scarcity and therefore rising costs.

As a last point, due to health reasons, toxic materials should be avoided. At some point future regulations might limit the use of such materials, especially since solar cells are an end-consumer product.

3.2 ITO and Other Metal Oxides

Metal oxides have had a long history and were explored as a transparent conductive material over 100 years ago.^[57] Due to their outstanding performance they still dominate the market for transparent contacts.^[58]

Optical properties of this material class are mostly affected by the large band gap of $E_g \approx 3 \text{ eV}$ and by its plasma frequency in the NIR range. Thus, a large transmittance region is formed between UV and NIR, which is of interest for solar cell application.^[59] Although pure metal oxides exhibit a high electrical gap and thus are insulators, the conduction band can be populated by doping with various atoms. As a side effect, the increased free charge carrier density has an influence on the transmittance spectra and the on-set of NIR reflection shifts towards the visible range.^[60] Unless active materials with strong NIR absorption are used, this has a minor affect on the suitability for solar cells.

In principle, the most common transparent conductive oxides (TCOs) such as SnO_2 , In_2O_3 and ZnO achieve similar optical and electrical properties (see Figure 3.1), whereas conductivities as low as $1 \cdot 10^{-4} \Omega \text{ cm}$ are reached. This corresponds to sheet resistances of about $10 \Omega/\text{sq.}$ at 90% transmittance.^[61–63]

At present, for current-driven applications in industrial scale mostly tin doped indium oxide ($\text{Sn}:\text{In}_2\text{O}_3$ or ITO) is utilized. In contrast to other TCOs, ITO reaches appropriate conductivity values also *via* large scale sputtering processes. Furthermore, ITO shows an industrial compromise in hardness, process stability, etchability, morphological stability and it requires lower processing temperatures. Therefore, over the previous decades ITO became the industrial standard of transparent electrodes for displays and

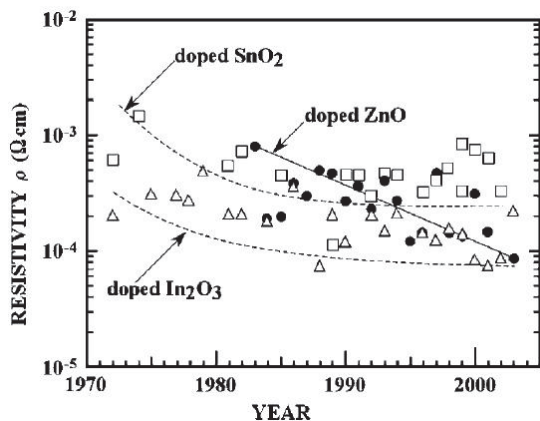


Figure 3.1: Development of the resistivity values for impurity-doped TCO films (ZnO: circle, SnO₂: square, In₂O₃: triangle). Source: Minami *et al.*^[63]

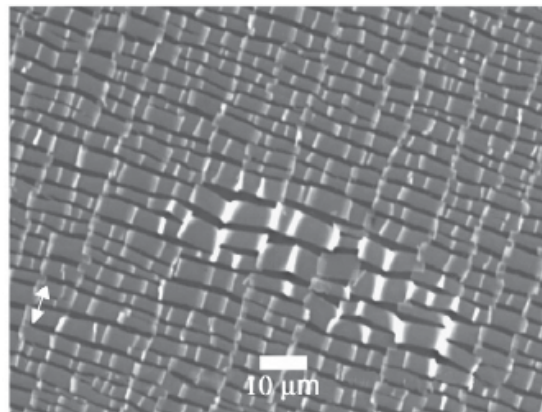


Figure 3.2: Picture of an ITO electrode on PET after applying tensile stress at 6% strain. Source: Sierros *et al.*^[64]

optoelectronic devices.

However, in the recent years, the strongest drawback of ITO became more pronounced — its scarcity. Because of the rise of TFT displays and the beginning of large area solar cell production, the indium price is of permanent concern. Since indium is mainly a by-product^B in the mining process of zinc, an economic increase of the production volume is not possible. Hence, rather the prices in combination with zinc have to be considered. Limited mining and growing demand lead to an increased and strongly fluctuating price.^[66] Furthermore, there are also concerns about the limited resources, which have to be sufficient for GW up-scaling of solar cell production.^[67] Companies respond to the scarcity issue by expanding research and development on alternative TCOs to achieve the same performance and reliability as for ITO.^[68] Therefore, in thin film photovoltaic industry aluminum doped zinc oxide (both materials exhibit high abundance) has already been introduced into production in the last years.

However, TCOs have also some general disadvantages, which are more or less valid for all combinations. High conductivities for TCOs can only be achieved with highly crystalline films, which require higher substrate temperatures during deposition. Particularly, on polymer foils this causes problems. Although some research was done on this issue, experiments at moderate temperatures below 200 °C still reveal low conductivity values.^[69] Along with other minor effects, this is the reason of the low performance of TCOs on plastic foils. In contrast to glass substrates, it is a challenge to reach 10 Ω/sq. at acceptable transmittance values.^[70–72]

^BThe indium concentration in the geosphere is as low as for silver at about 0.1 ppm.^[65] In contrast to silver, indium containing ores are extremely rare (low concentrations) and therefore do not play a role in earth crust exploitation.

In addition, the required high crystallinity is also responsible for the brittle nature of the material class. Bending a highly conductive TCO film leads to cracks (see Figure 3.2) and therefore to immediate device failure. Even for less crystalline films the bending radius is strongly limited.^[70,73]

3.3 Alternative Transparent Electrodes

Since flexible optoelectronic devices are meant to be a future market and bare metal oxides are not appropriate for these applications, much effort has been spent on the research of alternative electrode systems in the last years.

Among utilizing ignoble metals in an oxidized state also thin noble metal films can be applied as stand-alone electrode or in stacked dielectric-metal-dielectric systems. Although such Ag and Au films have been present for almost 100 years, there is still a lot of room for improvement. The films are produced under vacuum in sputter or thermal evaporation chambers. The crucial issue is a homogeneous film growth without large clusters to avoid plasmonic absorption.^[74,75] Furthermore, the stability of such thin films is of permanent concern, especially in operating devices.^[76,77] Because the metal films are very shallow, an optical tuning in dielectric-metal-dielectric stacks minimizes the absorption and gains a high transmittance.^[76] Values of $20 \Omega/\text{sq.}$ at transmittance of 80% can be achieved.^[75]

Besides, there are various organic electrode materials which are in general quite strain resistant and do not suffer from resource limitations. Within these, doped conductive polymers are the oldest approach by taking advantage of the π -orbital backbone transport in extended organic molecules.^[78] Originally, they were mainly used as antistatic coating. However, since the demand for large area transparent electrodes is growing, companies and research facilities try to push the conductivity to a higher level.^[79–81] The most common material poly(styrenesulfonate) doped poly(3,4-ethylenedioxythiophene) (PEDOT:PSS) is currently achieving values of $50 \Omega/\text{sq.}$ at 80% transmittance, which is still too low for a stand-alone electrode. Nevertheless, it can be used in combination with narrow metal grid systems to extract charges.^[82]

As an alternative, carbon nanotubes (CNTs) were discovered in the early 90s and a lot of research has been done on this promising material.^[83–85] The tubes are grown by chemical vapor deposition, laser ablation or arc-discharge and various methods exist to transfer them subsequently to the desired substrate.^[86,87] In order to obtain high conductive films, also a doping step is necessary. Although single tubes reveal amazing conductivities far above the ones of metal, the performance of networks is worse than expected. The efficiency is strongly limited by the contact resistance and values

of $80 \Omega/\text{sq.}$ at 75% have been achieved.^[48] Thus, large improvements are necessary to reach the specifications for a stand-alone electrode for photovoltaic application. Without such a breakthrough the material is limited to applications with lower resistance requirements (*e.g.* touchscreens).

Nevertheless, another fully carbon based electrode attracted a lot of attention in the last decade. Graphene, which consists of thin layers of carbon-based benzene rings^C, was produced for the first time in 2004.^[88] In following experiments the material revealed amazing properties^[88–91] both from a basic research and technological point of view. As for CNT films a stable doping and reliable deposition is the main obstacle. However, suitable transparent electrodes with $20 \Omega/\text{sq.}$ at 90% transmittance on large areas were already obtained.^[92] However, there is still a large demand for on-going research to obtain appropriate films on large areas *via* cheap industrial processes.

Finally, in the recent years a growing knowledge in nanostructuring and nanoparticle chemistry have made efficient nanostructuring of metals possible. Nanostructured metal networks, which combine high conductivity of metals with transmittance of the aperture in-between, were proposed as future transparent electrodes. The field can be divided into top-down and bottom-up approaches. The first represent accurate networks, which however suffer from complex and expensive lithography steps.^[93–95] The latter consist of random structures (*i.e.* nanowires grown from solution).^[96] The random approach is chosen in this research project, and the corresponding literature will be examined in the next section.

As a summary, performance examples for the mentioned electrode techniques are presented for comparison in Figure 3.3.

3.4 Nanowire Electrodes

This work focuses on nanowire networks consisting of single wires grown before deposition. However, there are also other representatives as directly reduced electro-spun networks^[98] and weaved meshes chemically grown directly on the substrate.^[99]

Nanowire networks as a transparent electrode were first suggested in a publication by Lee *et al.* in 2008.^[96] Within the paper of Lee, optical simulations showed that thin narrow silver lines present superior performance compared to the ITO standard material. Instead of realizing this kind of regular grid with imprint or lithography technologies, a simple solution based process with nanowire dispersions was utilized.

In general, the applied high aspect ratio nanowires (less than 100 nm thick and more

^COriginally graphene is meant to be a single layer of connected benzene rings. However, due to the difficulty in production, multi-layer structures up to 10 layers are called the same.

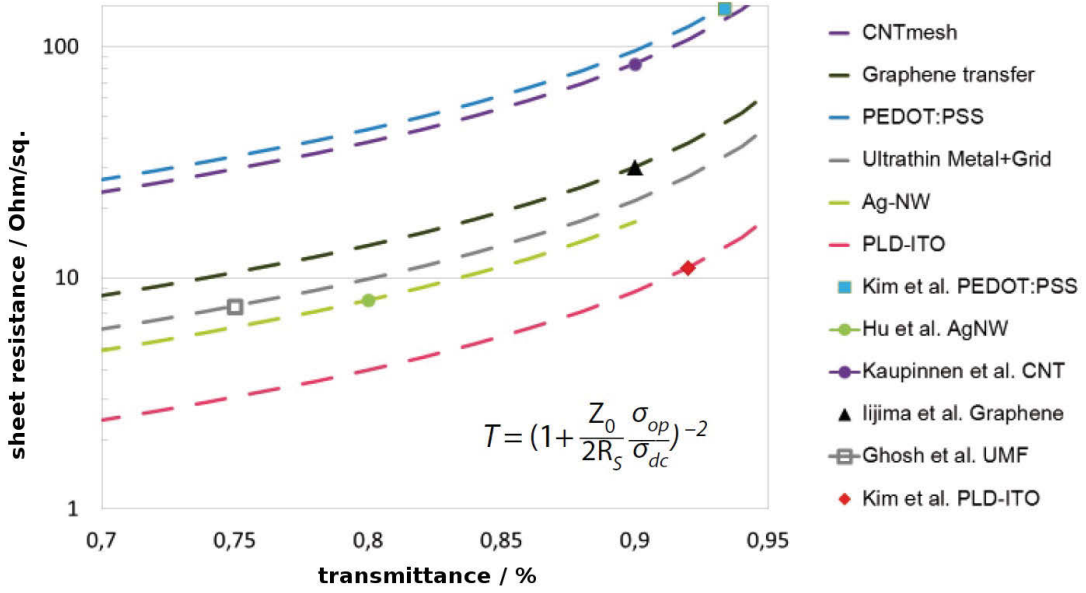


Figure 3.3: The transmittance-resistance plot for various transparent electrodes are presented including FoM-plots (described in Section 3.1) for a rough comparison. Source: Müller-Meskamp *et al.* in “Vakuum in Forschung und Praxis“.^[97]

than 10 μm long) are grown in solution (more details are presented in Section 4.2.1). Afterwards, it is usual that a solvent exchange takes place to simplify the application. Whereas in the first years a lack of scalable and reliable deposition methods had been present,^[52,96] in the last 3 years various methods, most of them scalable, have been published resulting in homogeneous films on glass and polymer substrates.^[70,100–102]

If the amount of deposited nanowires is large enough, the percolation limit is reached and the network gets conductive (see Section 4.1). Since the wires are mostly crystalline and reveal bulk like performance, the conductivity is mainly limited by the contact resistance between the wires.^[100] Different strategies were developed to enhance the contact by heating,^[96] pressing,^[70] ion-exchange,^[100] plasmon welding^[103] and matrix assisted densification.^[104] After post-treatment an ITO-like performance could be demonstrated,^[100] and the conductivity remains stable even when the substrate is extremely bent.^[52,105]

The major drawback of this electrode type becomes relevant when it needs to be integrated into an electrical device. Compared to thin films, the nanowires reveal high topography steps and therefore show an inherently rough surface. Since the active layers of an organic device are thin, the rough electrode results in short cuts between anode and cathode. Hence, the device integration has been a major goal of research, and various methods have been published in literature to avoid this problems. For instance, the rough surface can be planarized with a conductive covering layer as proposed in 2008 by Lee *et al.*^[96] Along with our work some other groups were able to

improve this method by optimizing the nanowire composite^D.^[41,101,106]

In order to avoid the additional absorption of this planarization layer, a transfer method can be used to flip over the nanowire composite. The method provides direct contact between solar cell and nanowires, which makes the requirement for a conductive planarization layer obsolete and therefore, the layer can be optimized for high transmittance.^[107] However, alongside with the complicated processing, which might be hard to scale up, the low conductivity in the area between the grid could be unfavorable for the current collection.^[106] A similar result can be obtained with a method presented by Gaynor *et al.*^[70] There the wires are deposited on a polymethylmethacrylate (PMMA) coated substrate and subsequently pressed into this soft layer at high pressures and elevated temperatures. Hence, mainly the critical high junctions are buried in the polymer and the roughness can be decreased.

^DThe term was first used by Gaynor *et al.* and denotes a nanowire electrode integrated into a matrix material by pressing.^[70] In this thesis the name is used more in general as a synonym for the nanowire-matrix system.

Chapter 4

Fundamentals of Nanowire Networks

In this chapter some general facts and properties of metal nanowire networks are shown to understand this electrode type. Since the networks consist of single stick-like objects and hence exhibit percolation behavior, corresponding effects are explained in the first section. Furthermore, an alternative figure of merit model for percolative transparent electrodes is presented. In the second section, the nanowire as nanoobject is introduced. After the presentation of various synthesis methods, special electrical and optical characteristics of single nanowires and their networks are addressed.

4.1 Percolation Networks

4.1.1 Cluster-Percolation and Conductivity

Percolation, derived from the Latin word *percolare* — to filter or trickle through, can be observed in many processes from physics^[108] to society^[109] or biology^[110] and can even have a huge impact regarding the scientific workday (*e.g.* making coffee^[111]). In general, it describes the formation of connected pathways inside a volume of arbitrarily distributed single objects.

The corresponding mathematical percolation theory, which describes such phenomena in an abstract graph, was devised in the middle of the 20th century and enabled a deeper insight in real percolation processes.^[112,113] An approach to describe such a problem mathematically is the bond-percolation model.^[114] Herein, $m \times m \times m$ points, as depicted in Figure 4.1 in 2D, have a probability of p (whereas $0 < p < 1$) to form a connection with a next-neighboring point and accordingly $1 - p$ for a disconnection. In such a graph for $p \ll 1$, only small connected finite clusters are formed. However,

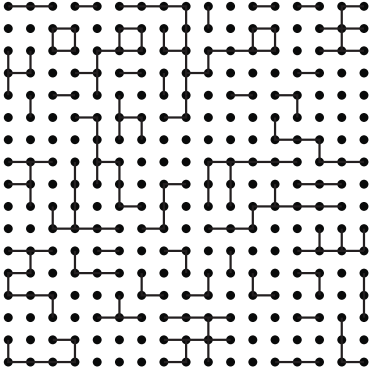


Figure 4.1: 2D illustration of a 17×17 bond-percolation problem. The sites are marked as black dots, while there is a probability of p so that a connection between neighbors exists.

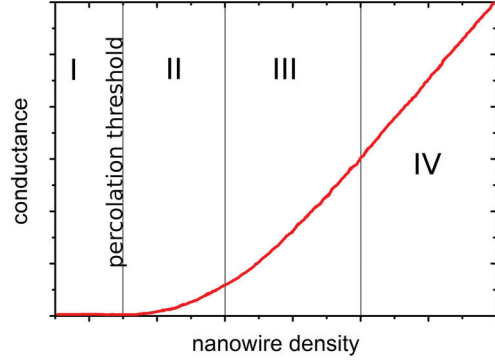


Figure 4.2: Conductance of a percolation network is depicted against wire density. Four different conductivity regions are marked.

with increasing p the clusters are growing and at a certain critical probability p_c (percolation threshold) an infinite cluster is obtained, which extends all over the volume. The final probability $P(p)$ at which a point belongs to the infinite cluster is accordingly defined as

$$P(p) \propto (p - p_c)^\beta \quad (p > p_c) \quad (4.1)$$

whereas β is the percolation exponent depending on the percolation type and system. $P(p)$ shows a power law behavior and is denoted as strength of the network.^[113]

The resistance of electrical networks is a typical field of application for such mathematical models, while Monte-Carlo investigations can be used to solve the problems.^[108,113] The combination of this statistical percolation with Kirchhoff's current law follows again a power law.

$$\sigma \propto (p - p_c)^\mu \quad (p > p_c) \quad (4.2)$$

However, as observed in experiment and simulation, the curves describing conductivity σ and $P(p)$ near the percolation threshold differ and therefore the exponent β for the percolation problem is not equal to the exponent μ for the electrical conductivity behavior.^A^[108,113,115,116] For larger values of p the behavior of σ deviates from the model formula. The search for a general relation between β and μ is a topic still open for further research.

^AIn a simple picture this fact can be illustrated as follows: right after the percolation threshold is passed, large connected clusters will occur. However, there are many open paths, which although belonging to the network, do not contribute to the conductivity. Only by adding further connections the conductivity shows an accelerated increase.^[113]

Instead of theoretical sites and points, in general extended particles of various shapes can also be calculated.^[117–120] In particular, sticks attracted a lot of attention due to their high aspect ratios.^[121,122] In simulations they are often handled as lines neglecting the particle volume, which simplifies the operation at small errors.^[123] Pike *et al.* firstly introduced this system to the community, calculating a critical percolation threshold density

$$N_c = f/l^2 \quad (4.3)$$

depending on the square of the length l and the critical factor f , which is supposed to be 5.71^B for random orientation.^[121] Considering the object density N as percolation probability p , Equation 4.2 transforms into

$$\sigma \propto (N - N_c)^\mu \quad (N > N_c) \quad (4.4)$$

and represents the fundamental relation of stick percolation. The critical exponents were calculated by Balberg *et al.* to $\beta = 0.14 \pm 0.02$ for the cluster percolation and $\mu = 1.24 \pm 0.03^C$ for the conductivity.^[116]

Besides, no percolation exponents were found regarding anisotropic or aligned stick orientation. All parameters are given for film-like 2D networks but of course also values for 3D exist.^[122]

4.1.2 Percolation in Transparent Nanowire Electrodes

For various alternative transparent electrodes, percolation behavior can be observed. For example, thin metal films evaporated on high surface tension sublayers show a strong clustering effect.^[75] When the density is increased, the islands start to connect and percolation behavior might be observed.^[125] CNTs exhibit a typical stick-like percolation behavior, which was intensely investigated in the last decade.^[126–128]

Metal nanowires show a similar threshold and for the percolation of metal nanowires in polymer matrices moderate research was already performed.^[125,129,130]

However, transparent electrodes, which possess a percolative density region, cannot completely (for all coverage ratios) be described by Equation 3.1 introduced in Section 3.1.

The conductivity behavior of a percolation network can be distinguished into four different regions, as presented in Figure 4.2.

In the first region I, isolated wires are present without large connected areas and the

^BMore recent results show a value of 5.637 .^[124]

^CMore recent results show a value of $\mu = 1.280 \pm 0.014$.^[124]

conductance is zero.

After the percolation threshold density N_c is passed, the aforementioned percolation behavior based on the power law in Equation 4.1 can be observed. The conductance in this region II is growing fast because each wire enables new paths in the network. The electrical properties depend strongly on the density so that instable results occur. Furthermore, right after passing the percolation threshold the conductivity of the film is rather low (see Section 4.1.1). Therefore, the current transport in this density region is inefficient and the network is not sufficient for a highly conductive electrode.

Region III is reached for densities N , much larger than the percolation threshold density ($N \gg N_c$). Here the growth rate of the conductivity slows down and as a result the increase of the slope in the conductance graph is going down as well (second derivative decreases). This region is more stable and conductivity approaches the high bulk value. Thus, proper nanowire networks can be achieved. In order to describe and evaluate the performance of transparent percolation networks within this region, De *et al.* suggested a model.^[125] Instead of the density, a film thickness d can be defined proportional to N . The conductivity in this region can then be described by

$$\sigma = \sigma_{\text{bulk}} \left(\frac{d}{d_{\text{bulk}}} \right) \quad (4.5)$$

whereas d_{bulk} , the thickness above bulk-like conductivity σ_{bulk} (denoted later on as region IV), is achieved. With the relation $R_{sh} = (\sigma d)^{-1}$ and Equation 3.1, a formula for the transmittance T_{total} depending on the sheet resistance R_{sh} can be derived.

$$T_{\text{total}} = \left[1 + \frac{1}{\Pi} \left(\frac{377}{R_{sh}} \right)^{1/(\mu_1+1)} \right]^{-2} \quad (4.6)$$

The factor Π

$$\Pi = 2 \left[\frac{\sigma_{\text{bulk}}/\sigma_{\text{Op}}}{(377d_{\text{min}}\sigma_{\text{Op}})^{\mu_1}} \right]^{1/(\mu_1+1)} \quad (4.7)$$

represents a figure of merit, which is used to evaluate the percolation network performance^D. Better performance causes a higher value, as can be seen in De *et al.* where also comparative data can be found.^[125] Equation 4.7 perfectly describes the performance curve of a transparent nanowire network with the percolation regime as shown for some examples in Figure 4.3(a). Moreover, the model can be proven by a semi-logarithmic ($T_{\text{total}}^{1/2} - 1$) plot in Figure 4.3(b) which exhibits a clear linear shape in the valid region.

Finally, when d_{bulk} is reached, the percolation behavior vanishes and additional wires

^DExponent μ_1 represents a special percolation exponent with unclear dependency.

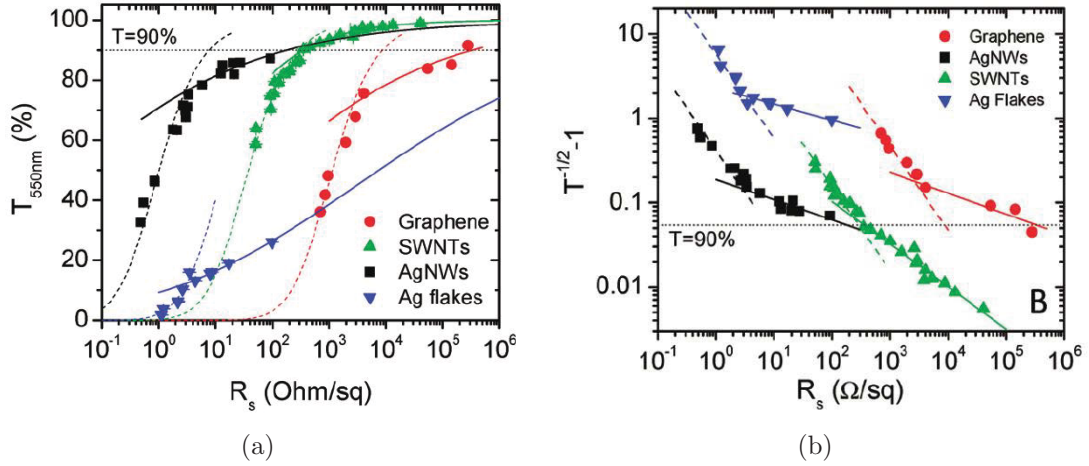


Figure 4.3: Fit of the bulk (with Equation 3.1; dotted line) and the percolation regime (with Equation 4.7; solid line) for various materials in a: normal $T_{\text{total}}-R_{sh}$ plot and b: $(T_{\text{total}}^{1/2} - 1)$ plot. Source: De *et al.*^[125]

just add some extra material. Thus, in the bulk region (IV) conductance is rising with a constant slope while the conductivity remains at σ_{bulk} . Because of the bulk behavior, this region can be described by Equation 3.1 for transparent conductive films, as introduced in Section 3.1. The model can be validated again with the behavior in Figure 4.3(b). As for the percolation regime, a linear fit matches the data.

Therefore, the $(T_{\text{total}}^{1/2} - 1)$ plot can be used to distinguish between the regions and classify the network. Whereas for CNT films the relevant sheet resistance values are located rather in the bulk regime,^[127,131,132] metal nanowire electrodes (Figure 4.3 shows fit for silver wires) are commonly described by the percolation regime.

It has to be mentioned that this is a qualitative discussion focusing on the introduction of the necessary models. While the critical density for percolation threshold and bulk onset is fixed, the transient from region II to III is not discussed here.

4.2 Metal Nanowires

4.2.1 Growth Mechanisms

There are various methods to produce metallic nanowires. In general, they can be classified as either bottom-up or top-down approaches.^[133–136] The latter one was already refused (see Section 3.4) due to the required expensive nanostructuring processes (*e.g.* nanolithography,^[137,138] nanoimprint^[139] or electro-spinning^[98]). On short term basis, large scale production will not be possible with such precise, but rather expensive methods.

In a bottom-up process, the nanowire is formed directly out of single atoms, whereas

self-assembly processes are utilized. There is a distinction between template-free and template-based methods, while the resulting nanowire has to be always self-sustained^E.^[140] The former are extremely rare since the confinement is based completely on self-assembly. Most famous is the vapor-liquid-solid (VLS) reaction,^[141] which belongs to the chemical vapor deposition methods. However, it is not usable for metals and the process is quite slow. Alternative template-free methods are rather exotic (*e.g.* methods for magnetic materials, where a wire is induced due to a magnetic field^[142,143]) and work only for selective materials.^[140]

More usual are template-assisted methods which can be divided in physical-template and soft-template processes.

A typical representative for the former is the anodized aluminum oxide (AAO) template in combination with an electro-deposition step.^[140,144] It can easily be adopted for various metals. However, due to the complicated and high number of template steps (*e.g.* template has to be removed afterwards), the approach is not appropriate for scaling-up nanowire production, in particular for long nanowires up to micrometers.

The scaling issues can be avoided by using soft-templates, because, commonly, the synthesis is done in a flask. On one side small stand-alone self-assembly structures like DNA-strands^[145] or block-copolymers^[146] can provide a possible framework.

As an alternative, capping agents connecting to the nanowire material, can serve as template. A plausible explanation of the self-assembly process for the mostly used polyol synthesis of AgNWs was proposed by Sun *et al.*^[147] A scheme of the growing procedure is illustrated in Figure 4.4 from left to right. At the beginning metal salt, solvent, capping agent and reducing agent are mixed together (A). At elevated temperatures, the solution is brought to an instable situation. The metal is reduced and precipitates, which leads to the formation of growing metal clusters (B). The capping agent adsorbs to the surface of the metal and has the potential to block the growth process. However, the adsorption strength of the agent depends on the crystal plane type and therefore varies all over the cluster (B). As a consequence, the growth exhibits an anisotropic behavior, and a confined nanowire structure is formed at the plane of weaker bonding (C, D). The resulting wires appear to be crystalline. Still, due to surface energy minimization in the early nanoclusters, various crystal structures (see Figure 4.4) appear depending on the synthesis conditions. Not all of them enable the formation of nanowires. For the AgNW synthesis the growth process results in twinned crystals, which finally can cause different nanowire shapes.^[148]

Up to now, most examinations were performed on silver nanowires grown by the before

^ESelf-sustained structures can exist without underlying substrate. In principle a transfer to other substrates is possible.

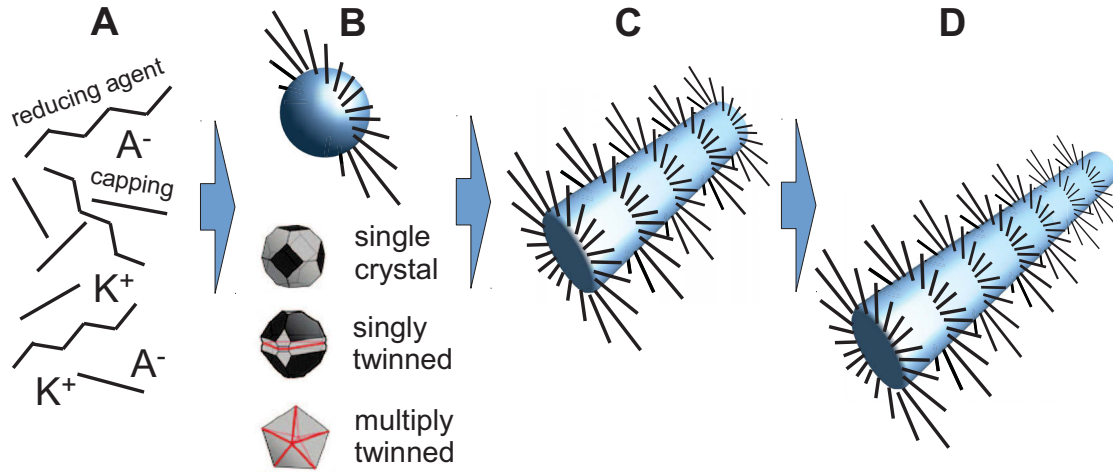


Figure 4.4: Growth scheme of a long metal nanowires *via* a capping agent method. Depending on the synthesis parameters differing crystalline structures can be formed. For the polyol synthesis, the 5-times twinned structure dominates causing wires of pentagonal shape.^[148]

mentioned polyvinylpyrrolidone (PVP) capping (polyol method),^[149] but also other synthesis approaches for Ag,^[150–152] Ni,^[153] Cu,^[154–157] Au,^[158] or mixtures of these^[159] were published. Whereas most methods result in isolated nanowires, others show a rather connected network.^[99]

Since the plane-dependent capping bonding is a quite sensitive process, specific capping agents have to be found for each material. Furthermore, the process is affected by various parameters (*e.g.* material amount, pressure, temperature). However, once a working method is found, large NW amounts can easily be synthesized.

4.2.2 Properties of Nanowire Structures

In general, the soft-template growth utilizing capping agents can result in very long wires in the high μm -regime with diameters from a few nanometers^[151,160] up to more than 100 nm.^[161] In the following paragraphs, the unique electrical and optical properties of these nanoobjects are discussed.

Electrical Characteristics

As aforementioned the nanowires exhibit a highly-crystalline structure, which strongly influences the conductive behavior and results in low resistivity near the bulk value ρ_{bulk} . In general, the nanowire can be approximated by a conductive cylinder and

therefore the resistance R should follow

$$R = \frac{\rho \cdot \text{length}}{\text{area}} = \frac{\rho_{\text{wire}} \cdot l}{\pi r^2} \quad (4.8)$$

with the resistivity ρ_{wire} of the nanowire. However, the small diameters below 100 nm cause confinement effects in two dimensions, which can lead to an increase in resistivity ($\rho_{\text{wire}} > \rho_{\text{bulk}}$). Hence, additional issues have to be considered to estimate the nanowire resistance.

If the diameter reaches the electron mean free path (emfp) of the applied material, the surface scattering gets more pronounced and the resistivity ρ_{wire} increases. Therefore, the resistance of a single nanowire increases much faster than expected from Equation 4.8, by assuming a stable ρ_{wire} .

The corresponding electron mean free path for bulk copper and silver (both are discussed in this thesis) can be estimated by calculating the average time between two collisions from the resistivity ($\rho_{\text{Ag}} = 1.51 \mu\Omega \text{ cm}$; $\rho_{\text{Cu}} = 1.56 \mu\Omega \text{ cm}$).^[162] Subsequently, together with the Fermi velocity, emfp values of $l_{\text{emfp,Ag}} = 50 \text{ nm}$ and $l_{\text{emfp,Cu}} = 40 \text{ nm}$ can be assumed^F.

A reasonable semi-theoretical equation to describe the increase of the resistivity in thin cylindrical wires was suggested by Dingle,

$$\rho_{\text{wire}} = \rho_{\text{bulk}} + \rho_{\text{bulk}}(1 - q) \frac{l_{\text{emfp}}}{d_m} \quad (4.9)$$

whereas q describes the scattering strength from 0 (diffuse — high losses) to 1 (specular — no losses).^[163] The term $(1 - q)l_{\text{emfp}}$ is denoted as critical length l_c and indicates the point where the onset of dimension problems can be expected.

The scattering factor was determined to be about 0.5 for crystalline AgNWs^G with a corresponding l_c of about 15 nm.^[164,165] Thus, down to diameters of 15 nm the effect of surface scattering is not pronounced and in experiments a resistivity increase by a factor of only 2 was observed compared to the bulk value.^[148,165]

Additional experimental literature data for the conductivity in AgNWs can be found for both soft-template-based synthesis^[100,149,166] and for crystalline e-beam evaporated self-assembly wires^[167]. All of them gave similar values.

There is less data available for crystalline copper nanowires. For example, Bid *et al.* investigated copper nanowires together with silver. They observed a similar behavior

^FThe full formalism can be found in the Ashcroft/Mermin.^[162]

^GThe value is as high as obtained for perfect single crystalline films at 4 K, which demonstrates the low defect density at the surface of such wires.

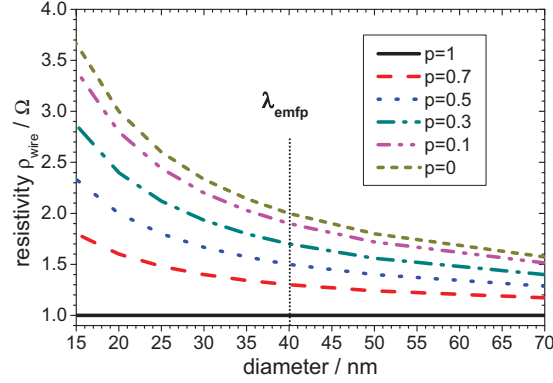


Figure 4.5: Plot of Equation 4.9 for various scattering ratios q ($\rho_{\text{bulk}} = 1$, $l_{\text{emfp}} = 40$ nm).

and, as for silver, the conductivity drop for nanowires down to 15 nm was just about a factor of 2 compared to the bulk value.^[165] Detailed surface scattering values were not presented. Other publications suggest for Cu specular scattering factors between 0.3 and 0.5.^[168]

Although the surface scattering might depend on synthesis and material, the similarity in the mentioned publications^[148,165,168] (all applied different production methods) suggest that the presented parameters seem to be reliable. Therefore, only moderate losses are expected by the surface.

Moreover, even for a defect-rich surface with scattering parameter $q = 0$ the deviations in resistivity for nanowires down to 15 nm are rather moderate, as can be seen in Figure 4.5. The curves for various q -values are calculated from Equation 4.8. In addition, comparing the increase of resistivity with the geometrical losses for shrinking radius in Equation 4.9, the impact of the resistivity change can be neglected.

As already emphasized, the crystalline structure is crucial for a high conductivity. The conductivity behavior for poly-crystalline conductor lines produced by e-beam^[169] and photo-lithography^[170] is completely different. In these lines the scattering at grain boundaries is limiting conductivity and, thus, overlaying the resistivity increase at small diameters. The distinction between grain-boundary and surface scattering is difficult.^[168,171] However, it is noteworthy that twinned-crystal-boundaries, which are also present in wires grown *via* capping agent, exhibit a low scattering potential and do not affect conductivity.^[165]

As a consequence drawn from the literature data, our crystalline nanowires should follow the Fuchs-Sondheimer theory^H which only includes surface scattering as

^HThe theory of Fuchs and Sondheimer is describing the surface scattering of thin metal films. They derived a formula similar to Equation 4.9.^[172] The theory assumes a constant scattering parameter q independent of the thickness.

additional loss-mechanism in the region below l_{emfp} .^[172–174] Therefore, resistivity losses are negligible for diameters above 20 nm.

In order to get a complete picture, the quantum confinement has also to be mentioned. When it comes to very thin wires below 10 nm, quantum mechanics have to be taken into account.^[175] Conductivity is strongly influenced by the quantum confinement effects until completely channel like behavior is observed.^[176] Such thin systems can also be grown *via* soft-template (*e.g.* DNA-template-synthesis^[145] or capping-substance^[151]) processes.

However, both surface scattering and quantum confinement only become effective at diameters below 20 nm. The wires used in our studies exhibit larger diameters and therefore the confinement effects can be neglected.

Optical Characteristics

A metal nanowire network consists of metal lines defining an aperture where light can pass through. However, nanowires exhibit in two dimensions a length below wavelength of incident light. Hence, nanometer-scale optical effects have to be considered. Such metal nanostructured objects can have a huge impact on the device performance.^[177]

Although parts of the sub-wavelength optical theory go back to the early 20th century,^[178] the topic has attracted growing attention with the development of controlled generation and analysis techniques for nanometer-sized objects at the beginning of the 21th century. However, mostly single objects and regular structures have been investigated due to simplicity. Therefore, although silver nanowires have been a major research object, the prediction of exact optical spectra for large ensembles of randomly distributed nanowires is still complicated. As no detailed established explanation for the spectral effects of a metal nanowire network has been found in the literature, and even controversial explanations were published in journals recently,^[179,180] the following paragraph will present an overview on possible effects. The spectrum of a nanowire network is analyzed in the results of Section 8.1.2.

Two different optical effects for films consisting of metal nanoobjects are worth considering. In the first place, the inelastic light interactions have to be mentioned. The effects are a result of light absorption and re-emission, while the processes are described by quasi-particles denoted as plasmons^I. These plasmons will be excited, if

^IPlasmons are quasi-particles which arise from the quantization of plasma (electron cloud) oscillations.

the conditions match as is briefly explained in the following paragraph.

When a metal nanoparticle with radius $r \ll \lambda$ (valid for all axes in 3D) is placed in an electro-magnetic field, coupling can occur as illustrated in Figure 4.6. The electron gas

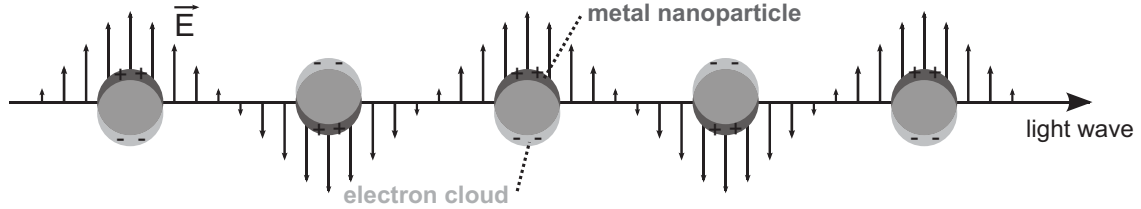


Figure 4.6: The scheme shows an in-phase oscillation of nanoparticle and electro-magnetic wave. When frequency matches the eigen-oscillation of the particle, strong absorption occurs denoted as LSPR.

in the nanoparticle follows the electrical field oscillation. At a certain frequency (depending on material, environment and particle dimension) a strong resonance can be observed causing large absorbance cross sections of the nanoparticle.^[181,182] These electron oscillations are named localized surface plasmon resonances (LSPR). For spherical particles a theoretical description can be laid out *via* Mie theory,^[178] utilizing size-dependent dielectric functions.^[183] In spheres an increasing particle size leads to the following effects:^[177,181,184,185]

- LSPR frequency shifts towards longer wavelengths
- absorbance cross section increases
- scattering cross section (radiative damping) increases ($\propto \text{volume}^2$)
- non-radiative damping^J (absorption cross section) increases ($\propto \text{volume}$)

Therefore, larger particles exhibit a stronger elastic scattering behavior at the LSPR frequency.

In addition, the environment affects the LSPR resonance concerning strength and frequency.^[181] As a result, it is highly relevant how much of the particle surface is covered with material. Thus, the substrate also affects the LSPR^K. Moreover, the environment can have an impact on re-emission characteristics. An emission enhancement is observed towards the surrounding material with the higher dielectric constant ϵ (refractive index n for susceptibility $\mu \approx 1$).^[188–191]

^JLoss mechanisms are a result of inter- and intra-band transitions.^[186]

^KThe corresponding parameter shift can be described with an approximation applying an averaged refractive index of substrate and air.^[187]

Other shapes show deviations in the LSPR spectra since higher (quadrupole, octupole, ...) modes of the oscillation occur and therefore various resonances can be found.^[183,191–193] From a qualitative point of view, the behavior of such particles stays the same. In an elliptical particle, the resonance frequency splits into a long and a short axis resonance showing the same behavior as derived for a sphere.^[152,181] In general, for complicated shapes (triangle, pentagon, cube) and inhomogeneous environments, simulations are necessary to predict the exact behavior.

Long nanowires ($l \gg \lambda$) are unique particles since the confinement is limited to two dimensions (1D object). Perpendicular polarized light (\vec{E} perpendicular to the nanowire — transverse electric (TE) polarization) results in LSPR-effects.^[194] The exact LSPR shown by a nanowire network is hard to determine due to the various mostly complicated shapes (round, hexagonal, etc.)^[152,195], coupling effects between the wires,^[196,197] and substrate interactions depending on the distance to the substrate.^[198]

For parallel polarized light (transverse magnetic (TM) polarization) the LSPR can be neglected. In long wires far above $1 \mu\text{m}$ just weak high modes can be excited in the visible light regime, since strong low order modes shift quickly towards IR.^[152,192,193] Thus, for very long nanowires only a weak white back-reflection without plasmon features can be observed.^[199,200]

Noteworthy regarding the absorption are surface plasmon polaritons (SPP) — another plasmonic effect. SPPs denote propagating electro-magnetic confined waves (coupled to electron plasma) moving along a metal-dielectric interface. This effect can be observed at metal thin films (2D) and along the length-axis of nanowires (1D object). In contrast to LSPRs, where strong re-emission is observed, the excited SPP modes are strong loss-mechanisms. The coupling between incident light and plasmon modes however is way more complicated than for the LSPR. In order to couple TM light (TE corresponds to the LSPR behavior) into SPP modes along the nanowire, a momentum mismatch^L has to be overcome.^[181,201] Without special incoupling structures — nanowire incoupling can only be observed at extended surface defects (*e.g.* ends of a single nanowire)^[148,202] — the effect can be neglected for long nanowires. It is worth mentioning that light diffraction can provide correct momentums to enable incoupling, as discussed in the next paragraph.^[179,203]

Alongside inelastic effects, the elastic interaction has to be considered. In this respect, the transmittance and reflectance are affected, whereas no absorption occurs.

^LThe wave vector \vec{k} of an electro-magnetic wave in the dielectrics is always smaller than that of an SPP. As long as k_x (along the interface, here along the nanowire) does not match to the SPP wavevector, in-phase incoupling is prohibited.

If the distance between two nanowires is small enough, a vertical metal-insulator-metal waveguide will be formed. The slit hinders aperture transmission for TE polarized light, which is a typical effect in metal line gratings (cut-off behavior). The strength of the effect depends on wavelength, distance, structure height (diameter), and shape. Due to the fact that in random networks the pitch is randomly distributed, rather broad-band effects are expected for irregular structures. For TM polarization, such transmittance problems are not observed and incident light can pass.^[179,180]

Furthermore, the abrupt spatial variation of the refractive index results in diffraction. At regular structures (*e.g.* metal gratings) this causes typical minima-maxima diffraction patterns, depending on angle and wavelength. The nanostructured layer behaves like an effective plasma media.^[204] However, in the case of arbitrarily distributed structures, the objects act as single scattering centers. Therefore, no diffraction patterns are visible and a rather homogeneous scattering (independent on angle and wavelength) is expected.

As aforementioned, diffraction can lead to SPP momentum matching and therefore efficient absorption in SPP modes (inelastic effect). This transmittance loss is pronounced in regular gratings with special conditions. However, in the random case with homogeneous scattering, SPP modes are hardly excited because the lack of constrained diffraction orders hinders the coupling of large light amounts into the nanowire.^[179]

In conclusion, the optical feedback of metal nanowires is characterized by plenty of effects. In general, due to coupling, the electrical field distribution in random NW networks is complicated, as a simulation by Podolskiy *et al.* illustrates.^[205,206]

Chapter 5

Experimental

5.1 Electrode Preparation

Substrates and Dispersions

Schott borofloat-glass BK7 from Prinz Optics (1.1 mm thick) is used as substrate for the nanowire electrodes. The glass substrates are cleaned with two different procedures, either a 3 step process (acetone \rightarrow ethanol \rightarrow isopropanol) or a 2 step process (n-methyl pyrrolidone (NMP) \rightarrow ethanol). Each cleaning step is conducted in ultra-sonic bath for the duration of 15 min. As reference, ITO coated glass substrates, which are structured by an etching process, are purchased from Thin Film Devices Inc. They undergo the same cleaning procedure as for pure glass. In order to remove dust particles, a polymer cleaning step with ‘First Contact’ from Photonic Cleaning Technology is applied to the samples processed at the UFO system (see Section 5.2). As flexible substrate, the PET foil Melinex ST504 from DuPont Teijin Films is used. The respective cleaning procedure consists of ethanol and isopropanol, each 15 min in ultra-sonic bath. Before the deposition of material, the substrates are treated in oxygen plasma for some minutes (less than 1 h between treatment and deposition). In addition, the PET samples are heated to 140°C for some minutes directly before deposition, in order to minimize adsorbed water.

The commercial AgNWs are purchased from Bluenano Inc. (BN). Unfortunately, during this work the specifications of the dispersions changed. In general, the nanowire types SLV-NW-60 and SLV-NW-90 are ordered and named with batch numbers from 1 to 4. A detailed analysis of the quality is not performed and, therefore, just supplier specifications or rough estimations are given in the result sections.

Besides the commercial dispersions, Nelli Weiß synthesizes nanowires for our research in

a collaboration with the Physikalische Chemie at the TU Dresden. The three synthesis approaches ($1 \times$ AgNW, $2 \times$ CuNWs) are presented in the following sections.

CuNWs, based on Rathmell *et al.*

The synthesis is based on a publication presented by Rathmell *et al.*^[207] The amount of reactants is ten-times smaller.

Materials: Sodium hydroxide (NaOH, Aldrich), polyvinylpyrrolidone (55,000, Aldrich), ethylenediamine (EDA, 98%, VWR) anhydrous hydrazine (35%, Aldrich), and 2-propanol (VWR). All chemicals are used without further purification.

Synthesis: NaOH (200 mL, 15M), $\text{Cu}(\text{NO}_3)_2$ (10 mL, 0.2M), EDA (3 mL), and hydrazine (2.5 mL, 35 wt%) are added to a flask. Between each addition, the mixture is swirled by hand for 20 s. Subsequently, the solution is heated at 80 °C for 60 min while stirred at 200 rpm. Afterwards, the suspension is centrifuged at 4500 rpm for 5 min before the supernate is decanted from the NWs. Subsequently, the wires are dispersed in 3 wt% aqueous solution of hydrazine. The centrifugation and decantation are repeated three times with hydrazine as solvent. In order to enhance the dispersability of NWs, an additional step utilizing PVP is applied. The nanowires are dispersed in 16 mL deionized water (DI) and 16 mg PVP, using vortexing and sonication. Then, the dispersion is slowly added to a solution of 64 mL DI and 6.4 g PVP. After 20 min agglomerates settle down and the appropriate well-dispersed wires are skimmed off. Two NW batches are synthesized, one with and one without the PVP post-synthesis treatment step. As a final step before application, the nanowires are washed once with 2-propanol (dispersion and centrifugation step) and stored in 2-propanol.

CuNWs, based on Mohl *et al.*

The synthesis is based on a publication presented by Mohl *et al.*^[154] It is noteworthy that the reactant amounts are adjusted for a 250 mL autoclave. The recipe describes the synthesis of the CuNWs which are in focus of Chapter 7. However, some variations are tested in order to decrease the wire diameter. The corresponding changes and results are summarized in Section 7.2.3.

Materials: Copper(II) chloride (CuCl_2 , Aldrich), D-glucose ($\text{C}_6\text{H}_{12}\text{O}_6$, Aldrich), hexadecylamine ($\text{C}_{16}\text{H}_{35}\text{N}$, HDA, 95%, Aldrich), *n*-hexane (C_6H_{14} , 97%, VWR), and 2-propanol (VWR). All chemicals are used without further purification.

Synthesis: Copper chloride (0.17 g, 12.5 mM) and glucose (0.489 g, 2.7 mL) are dissolved in 100 mL DI. Then 1.8 g hexadecylamine are slowly added with a subsequent mixing (magnetic stirrer) over night until a light-blue emulsion is achieved. Afterwards, the emulsion is filled in a Teflon-lined steel autoclave of 250 mL capacity. At first, the

autoclave is heated at 120°C for the duration of 24 h under autogenous pressure and then cooled down to room temperature. Finally, the reddish brown solution is centrifuged (2000 rpm) and washed in a sequence of DI, *n*-hexane, and 2-propanol. The CuNWs are re-dispersed in 2-propanol in order to prepare them for further experiments.

AgNWs, based on Bergin *et al.*

The synthesis is based on a publication by Bergin *et al.*^[161] with a heating step of 4 h at 140°C.

Materials: Ethylene glycol (EG, Backer), polyvinylpyrrolidone (55,000 MW, Aldrich), NaCl, Fe(NO₃)₃, and AgNO₃ (Fluka).

Synthesis: At the beginning, 158.4 ml ethylene glycol are filled to a flask and pre-heated for 1 h at 140°C. Subsequently, 0.2 mL of a NaCl solution (0.257 g NaCl in 20 mL EG), 0.1 mL of a Fe(NO₃)₃ solution (0.081 g Fe(NO₃)₃ in 10 mL EG), 20.76 mL of a PVP solution (1.05 g PVP in 25 mL EG), and 20.76 mL of a AgNO₃ solution (1.05 g AgNO₃ in 25 mL EG) are added to the EG. The flask is stoppered, and the solution is heated for 4 h at 140°C. Subsequently, the solution is mixed and vortexed with acetone followed by a centrifugation step for 1 h at 2000 rpm. The supernatant is skimmed, dispersed in DI, and centrifuged once more. The washing-step is repeated with ethanol, resulting in the final dispersion ready for application.

Dip-Coating

Dip-coating is a typical lab technique for the deposition of thin films. The general process flow is illustrated in Figure 5.1. As first step, a substrate is immersed into a solution (A). When the substrate is pulled out, it is wetted with the solution (B). Due to gravity, some of the liquid runs off. At the same time, the remaining solvent starts to evaporate. During the drying process the non-volatile substances settle down on the substrate and form a thin layer (C).

In this thesis an automatic dip-coating machine is used, as shown in Figure 5.2. Immersion speed, pull-out speed, cycle number and break-times can be controlled by a computer program. In order to avoid cluster formation during the long dipping procedure, the dispersion is mixed by a magnetic stirrer or an ultra-sonic bath (during immersion no treatment is done). Moreover, the whole system is placed in a closeable bio-flowbox, which allows the control of air humidity. In general, most of the samples are produced at low humidity around 30%, achieved by silica gel as water absorber.

As dispersion reservoir a 25 ml beaker is used. Therefore, the substrate size is limited to about $2.5 \times 2.5 \text{ cm}^2$. Larger reservoirs would rise up the material consumption.

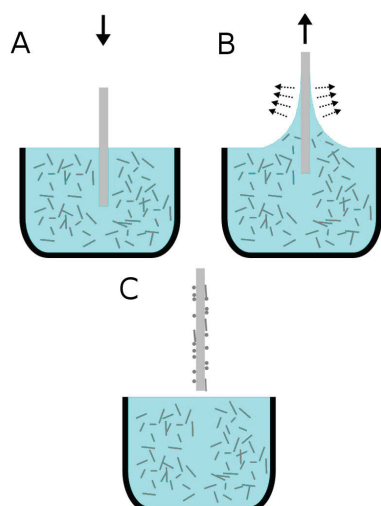


Figure 5.1: Process flow scheme for dip-coating into a nanowire dispersion.



Figure 5.2: Automatic dip-coating machine placed in a bio-flowbox.

The standard dip-coating parameters are immersion velocity 0.1 mm/s, pull-out velocity 0.1 mm/s, drying break 20 s and immersion-break 5 s. In general, the substrate is rotated by 90° after half of the cycles. Typically, the coating dispersions are freshly prepared before dip-coating and used maximal for 3 d. In order to decrease the number of agglomerates, some minutes of ultra-sonic treatment are required before deposition.

Spray-Coating

Spray-coating is a widely used industrial technique. In our experiments a x-y-z spray-coating robot F7300N is used with an attached 3-pressure nozzle SV1000SS both products from Fisnar Inc. The spray-coating head works similar to a perfume flacon — an air flow is passing a small needle valve which is connected to the material reservoir (cartridge). In addition, a material pressure, which is applied to the material reservoir, can be chosen arbitrarily to have more control of the deposition. The third pressure is used to switch a needle valve, which enables vertical spray-coating without dripping and clearing at the end of a coating session. In order to set the system under pressure, a standard nitrogen bottle is utilized, while the pressure is controlled by means of a reduction valve and a pressure control unit, which is synchronized with the coating-robot. The whole system is illustrated in Figure 5.3. The robot can steer arbitrary positions within our 20 by 20 cm set-up. A simple program is used to coat the required patterns automatically. Moreover, a hot-plate is mounted serving as heatable substrate holder. In order to avoid agglomerations, the material is stirred in the cartridge during coating. Instead of an over-pressure, the material cartridge is connected to a vacuum pump to decrease the deposition amount.

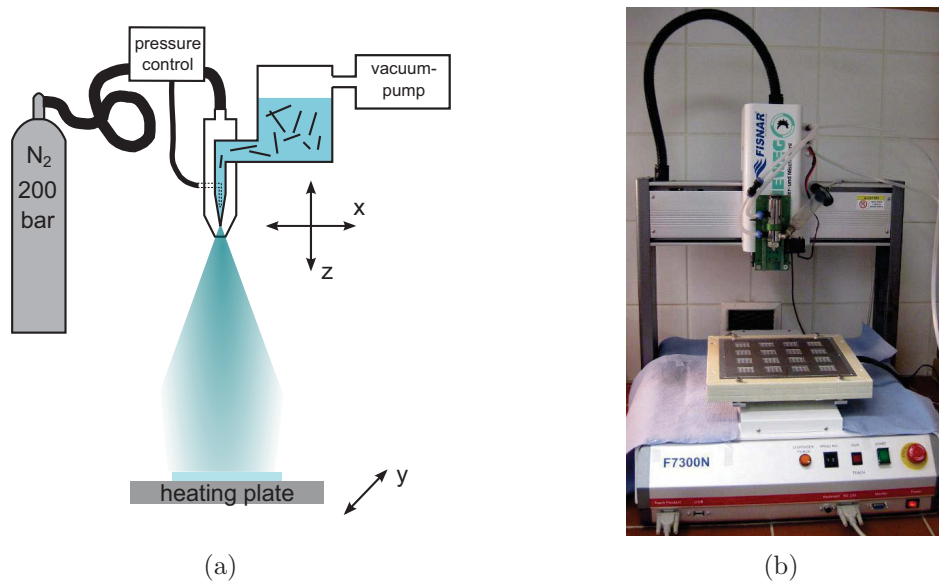


Figure 5.3: Scheme of the used spray-coating set-up (a) with the corresponding photo of the device (b) taken by F. Lehnert.

The standard values for deposition are z-position of 12.5 cm, cartridge pressure of $2 \cdot 10^4$ Pa below atmosphere, coating pressure of $2 \cdot 10^4$ Pa, velocity of 3 cm/s, line pitch of 0.8 cm, substrate temperature of 80 °C.

Planarization

The planarization layer is applied by spin-coating. This technique represents a typical lab method for obtaining thin homogeneous layers. In order to tune the layer thickness, the spin-speed is adjusted accordingly. In this work the water-based solution PEDOT:PSS Clevios PH1000 (by Heraeus) is used as standard planarization material (see Section 6.4.1). An extensive study of this solution can be found in the PhD thesis of Kim.^[208] The standard deposition parameters are taken from his work — spin-speed 2500 rpm, spinning-time 30 s and annealing temperature 120 °C. In order to achieve a highly conductive polymer, 10% ethylene glycol (EG) are added to the solution. When spin-coating on glass, a pre-treatment with oxygen-plasma is acted out. NW films are treated instead with argon as process gas.

Structuring

The IAPP possesses a well established infrastructure for the deposition and analysis of organic solar cells. Therefore, a general device layout (see Figure 5.4) is used in order to enable easy processing and measurement. In general, four pixels are placed on a square 2.5 cm (\approx 1 inch) substrate. The pixels are defined by the bottom-electrode

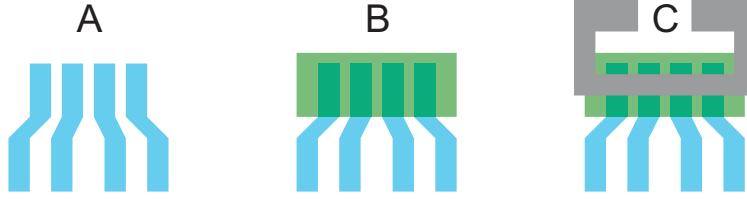


Figure 5.4: Structure scheme of the bottom-illuminated solar cell layout on a 2.5 by 2.5 cm substrate consisting of the transparent bottom contact fingers (A), the organic material area (B) and the top contact bar (C). Thus, the cell can be connected at the substrate edge.

finger width and a 2.5 mm wide perpendicular metal contact-bar which is evaporated through a mask. The bottom-electrode has to be structured before material deposition. The ITO reference substrates are structured by the supplier *via* an etching process. Therefore, the ITO finger width is fixed to 2.5 mm corresponding to a pixel size of 6.3 mm^2 . The structuring of the NW electrode (NW-PEDOT composite) is investigated in Section 6.4.2.

Most of the time, the electrode is structured with a 1064 nm Nd:YAG laser scribing system by ACI Laser GmbH (type: EconomyDiode with Workstation) with pulse duration = $3 \mu\text{s}$, velocity = 250 mm/s, repetition rate = 6000 Hz, power = 100%, and cycles = 2 for glass substrates. For PET foils values differ in power = 50% and repetition rate = 2000 Hz. The line width of the nanowire bottom-electrode is varied in order to achieve various pixel sizes ($2.5 \text{ mm} \times \text{bottom-contact width}$).

5.2 Solar Cell Preparation

The deposition of organic material stacks is carried out in ultra high vacuum chambers (UHV) at a base pressure of less than 10^{-8} mbar. An illustration of an evaporation unit can be seen in Figure 5.5. At the bottom of the chamber, a ceramic crucible is mounted. Its temperature (measured with thermocouple) can be increased up to about 600°C by resistive heating. At temperatures above the evaporation threshold, the material starts to evaporate so that the molecules leave the crucible up-wards with an angular \cos^x -distribution. The substrate is placed upside down above the crucible inside the molecule stream. Hence, the material is deposited on the cold substrate surface while shutters or masks can be used to control the deposition area. Additionally, a quartz monitor is placed in the stream to measure the evaporated material amount. This is done by registering the eigen-frequency shift of the quartz crystal caused by the added material layers. Thus, the material amount on the sample can be estimated when the tooling factor between quartz and sample is known. In order to enable co-evaporation (absorber blends or doped layers), more crucibles are

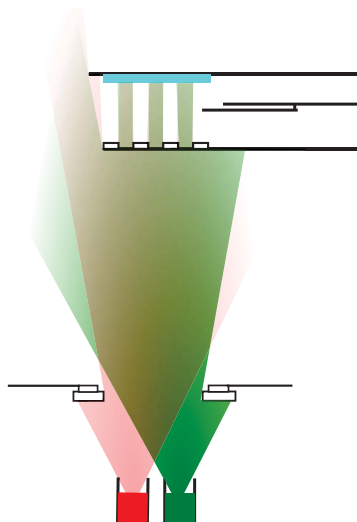


Figure 5.5: Scheme of a unit used for co-evaporation of organic materials.

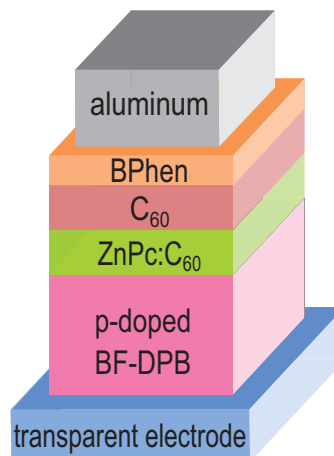


Figure 5.6: Layer structure of the deposited small-molecule organic solar cells.

necessary, which can be controlled independently. The metal evaporation is performed in a similar way. However, due to high evaporation temperatures tungsten boats are used for silver or even specialized crucibles (by Creaphys GmbH) have to be applied for aluminum.

Two different evaporation systems are used in this thesis. The so called ‘UFO’ is a multi-chamber system. A central handling chamber is surrounded by various chambers containing 3 - 6 crucibles or metal sources whereas the chambers are divided by valves. Each chamber is used for a certain material class to avoid contamination. The substrate size is limited to 1 inch.

In contradiction, the ‘Lesker’ tool is a single chamber system. More than 10 sources are placed in one large chamber. The system enables a homogeneous deposition on an area of $15 \times 15 \text{ cm}^2$, which requires higher material amounts. At the edges of the area larger deviations in film thickness (about 5% for the outer areas) have to be considered. The large deposition area can be used to produce 6 by 6 standard 1 inch layouts (on one $15 \times 15 \text{ cm}^2$ substrate) simultaneously. Instead, by using a special sample holder also single substrates can be processed. It is noteworthy that in this case the number decreases to 18 samples in one run. Moreover, during material evaporation shutters can be used to wedge the area and therefore, produce slightly deviating organic stacks. This provides the great opportunity to optimize the solar cell by tuning the stack structure. Furthermore, the system allows substrate heating during evaporation.

At both evaporation chambers a glovebox is mounted to avoid water and oxygen contamination during sample transfer into the vacuum. Moreover, the organic

materials are air-sensitive and therefore have to be measured or encapsulated (mostly introducing a getter material) under nitrogen atmosphere avoiding air contact.

Because of the well-controlled evaporation approach, thin material layers below 1 nm as well as thick films with hundreds of nanometer can be deposited with high accuracy. Therefore, complicated layer structures with various materials can be produced. In Figure 5.6 a p-i-i layer sequence is illustrated as typically applied in this thesis. The stack is chosen due to its similarity to more advanced structures, in terms of layer height, and wide relevance as model system at our institute.^[209,210] The structural formulas of the utilized materials are depicted in Figure 5.7.

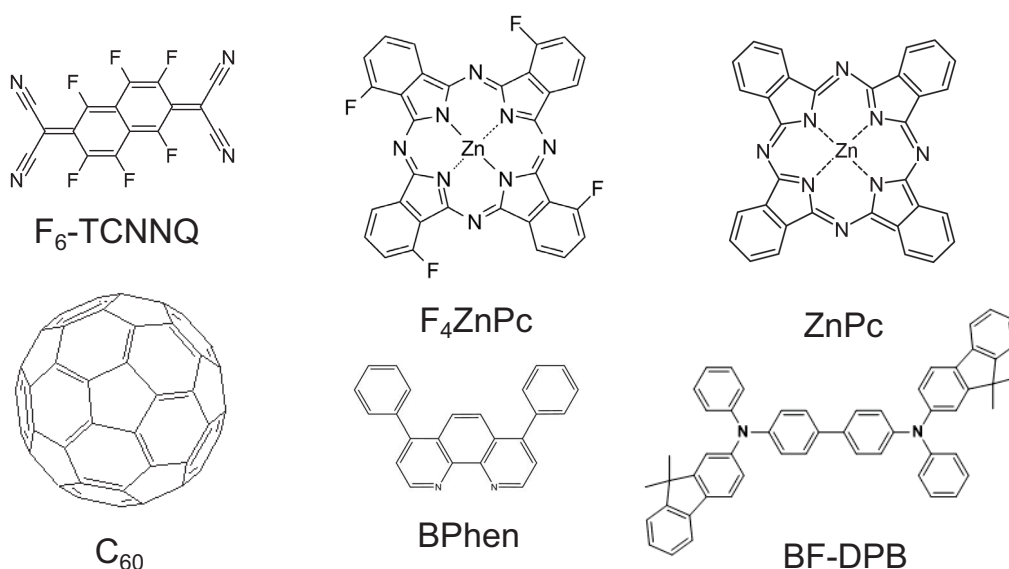


Figure 5.7: Organic materials used for the solar cell production. All materials are sublimated at least two times.

On the transparent bottom-electrode (ITO or PEDOT-NW composite) a thicker p-doped HTL is deposited with a 1 nm pure dopant layer underneath. In this case, a layer of N,N'-((diphenyl-N,N'-bis)9,9,-dimethyl-fluoren-2-yl)-benzidine (BF-DPB) is used, doped either with 10 wt% 2,2'-(perfluoronaphthalene-2,6-diylidene)dimalononitrile (F₆-TCNNQ) or with 5 wt% of the dopant NDP9 by Novald AG. On top of the HTL, the donor-acceptor blend (bulk heterojunction absorber) is applied *via* co-evaporation. Herein, the fullerene C₆₀ acts as acceptor material and as donor either zinc-phthalocyanine (ZnPc) or tetrafluoro-zinc-phthalocyanine (F₄ZnPc) are introduced. The F₄ZnPc blend is heated to achieve a desirable morphology. Subsequently, the blend is covered with a pure C₆₀ layer. Instead of an electron transport layer, a thin layer of 4,7-diphenyl-1,10-phenanthroline (BPhen) is used as exciton blocking layer and

diffusion barrier. Finally aluminum is used as evaporated top-contact.

5.3 Electrode Characterization

Sheet Resistance

The sheet resistance is a crucial parameter for transparent electrodes, since it describes the absolute resistance of a thin film. It represents the resistance value of a square film contacted on the full length of two opposite sides as illustrated in Figure 5.8. The

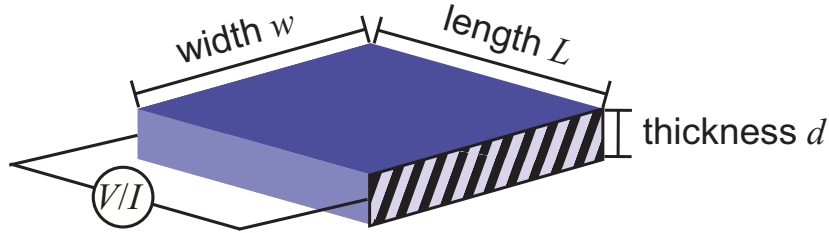


Figure 5.8: Scheme explaining the notation for the sheet resistance definition.

resistance R of a conductive cuboid follows

$$R = \frac{\rho L}{w \cdot d} \quad (5.1)$$

with resistivity ρ and the object dimension $w \times L \times d$. By assuming a square structure, Equation 5.1 can be simplified to

$$R = R_{sh} = \frac{\rho}{d} \quad (5.2)$$

whereas the resistance is defined as sheet resistance R_{sh} . Thus, the sheet resistance includes film thickness. Special geometries can be utilized to measure R_{sh} at thin films. In order to avoid contact resistance, a 4-wire set-up (here: measurement is performed with a source-measurement-unit 2400 from Keithley) has to be used. In this work, either a ‘302 resistivity stand’ by Lucas Labs or the van-der-Pauw method is applied as measurement system.

In the resistivity stand, four point contacts are aligned in one row with a constant distance (here: $s = 1.588$ mm), as illustrated in Figure 5.9. At the outer pins a constant current (here: $I = 1$ mA) is applied while the potential-drop V is measured between the inner ones. Geometrical calculations^[211] for homogeneous, thin and infinite films result in

$$R_{sh} = \frac{\pi}{\ln 2} \cdot \frac{V}{I} \quad (5.3)$$

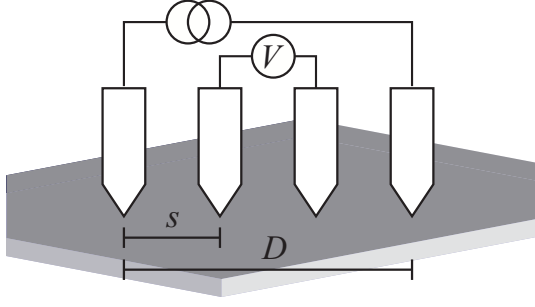


Figure 5.9: Scheme of a 4 point probe (4PP) resistivity stand.

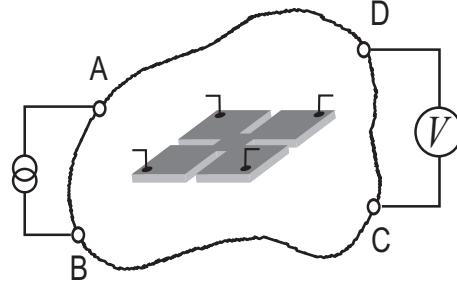


Figure 5.10: Scheme of the 4-wire connection in a van-der-Pauw measurement. In the center the clover-structure is illustrated.

containing the applied current I and the measured voltage V . The geometrical factor $\pi/\ln 2$ is only valid for infinite areas. The value has to be corrected for smaller areas (a corresponding curve can be found in literature^[211]) while the error increases for dimensions in the range of the contact pin distance ($L \approx D$). With our set-up, the measured area should not be smaller than 1 by 1 cm and for a coated $2.5 \times 2.5 \text{ cm}^2$ substrate the geometrical factor is ≈ 4.4 .

A more general method was published by L. J. van der Pauw.^[212] The theory describes how the resistivity of arbitrary thin films can be measured. Four point contacts have to be attached at the edge of the sample as illustrated in Figure 5.10. By measuring $R_{AB,CD} = V_{CD}/I_{AB}$ (demonstrated in the picture) and $R_{BC,DA} = V_{DA}/I_{BC}$, the sheet resistance can be calculated with

$$R_{sh} = C \cdot \frac{\pi}{\ln 2} \cdot \frac{R_{AB,CD} + R_{BC,DA}}{2} \quad (5.4)$$

whereas the correction factor C is depending on the deviations between the two resistance values. Factor C is a result of the asymmetric geometry in the set-up and can be achieved by a numerical calculation.^[213] In order to obtain the required point contacts at the sample edge, a clover-structure is scratched into the sample (see center of Figure 5.10). Thus, the contact area and the distance to the edge are less important and silver paste contacts can be utilized. With the van-der-Pauw method smaller areas can be measured. Moreover, contact problems can be avoided because of the extended and stable contact areas.

UV-vis Analysis

In order to fully analyze the transmittance behavior of a nanowire film, various values have to be measured. The transmittance T is defined as $T = 1 - R - A$ with reflectance R and absorption A , whereas the incident intensity I_0 is set to 1. Transmittance and

reflectance are defined here as total values ($R_{\text{total}}, T_{\text{total}}$), which consist of a specular part ($R_{\text{spec}}, T_{\text{spec}}$) and a diffuse part ($R_{\text{diff}}, T_{\text{diff}}$) representing the scattered light. Thus, the complete losses can be summarized by the equation

$$1 = \underbrace{R_{\text{diff}} + R_{\text{spec}} + A}_{\text{absorbance } A_{\text{abs}}} + T_{\text{diff}} + T_{\text{spec}} \quad (5.5)$$

while the affected part of the incident light beam is denoted as absorbance. The ratio of the scattered intensity *vs.* the total intensity is defined as HAZE-factor H

$$H_r = \frac{R_{\text{diff}}}{R_{\text{total}}} \quad H_t = \frac{T_{\text{diff}}}{T_{\text{total}}} \quad (5.6)$$

with H_r for the reflectance and H_t for the transmittance.

All mentioned values depend on the wavelength λ . Nevertheless, in this thesis, an averaged value between 400 and 800 nm is used because of the relevance in solar cells. Since AgNW networks exhibit a rather flat spectrum, sometimes certain values are taken instead (marked in the text).

The respective spectra are measured with the UV-vis spectrometers Shimadzu UV-3100 (including integration sphere unit MPC-3100) or a Perkin Elmer Lambda 900. Both spectrometers use a two beam set-up correcting lamp fluctuations. Therefore, the intensity of the measurement beam and the reference beam are compared to achieve the absorbance caused by the sample. For the transmittance measurement air is taken as reference and, thus, the substrate is included in the spectra. In the reflectance mode a strongly scattering barium oxide is used as reference.

In contrast to the specular transmittance, which can be measured in a rather simple straight forward set-up, for all other values an integration sphere is required. The corresponding measurement approaches are illustrated in Figure 5.11. It is noteworthy

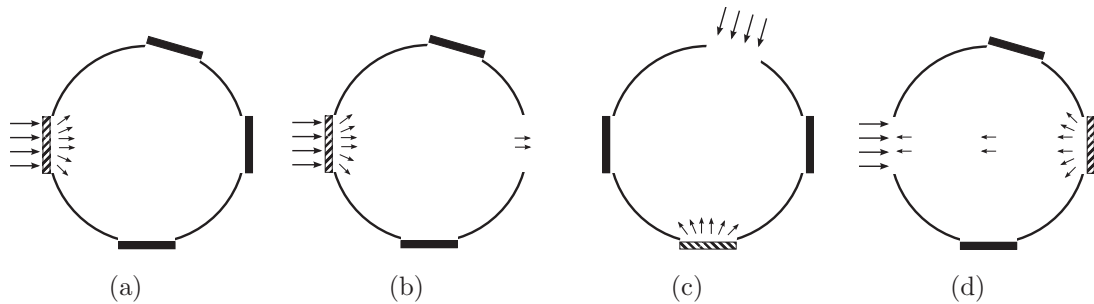


Figure 5.11: Scheme of the different modes of an integration sphere, whereas the sample (shaded) and a reflective BaO cap (black) are placed in the corresponding position for a) total transmittance, b) diffuse transmittance, c) total reflectance, and d) diffuse reflectance.

that all of them can be realized with the same sphere.

In order to achieve polarization dependent values, right in before the sample/ sphere a polarization filter is placed.

Fluorescence Spectrometer

The fluorescence measurements are performed at the Fraunhofer COMEDD with a FluoroMax-4 from Horiba Jobin Yvon applying a long integration time of 5 s. At the measured curve the background is subtracted and the excitation intensity fluctuations during measurement are corrected, as well. For an excitation wavelength of 530 nm an edge filter which is blocking $\lambda < 550$ nm is applied.

Micrographs and Microstructure

The atomic force microscopy (AFM) images are taken either by a Nanoscope IIIa from Veeco or an AIST Combiscope. In both devices silicon tips are used in non-contact mode.

Most of the scanning electron microscopy (SEM) pictures are taken with a FEI Phenom table top device. Up to a magnification of 24000 \times this device enables a fast view on the sample within less than 30 s. Since magnification is limited, no special handling (*e.g.* gold sputtering or contact stripes) becomes necessary.

The high resolution micrographs are taken with a Carl Zeiss DSM 982, which offers more opportunities to adjust the picture quality. All samples are grounded with copper tape and on badly conductive samples (*e.g.* low density CuNW films) a thin gold film is sputtered to minimize charging effects. Moreover, tilted images up to 90° are possible with this microscope.

Powder X-ray diffraction patterns (XRD) of the nanowire films are recorded using a Siemens D5000 diffractometer with Cu K_α radiation and a Bragg-Brentano set-up.

An Philips CM-120 with 120 kV acceleration voltage is used for the transmission electron microscopy.

SPICE Simulation

SPICE is an analog electronic circuit simulator. In this thesis, the open-source program ‘Ngspice’ is used. It processes a node list with the corresponding resistor (two nodes (intersections) + resistance) and calculates net parameters (*e.g.* potential, current flow, resistance) between defined nodes.

The algorithm starts with setting-up a Kirchhoff’s law equation for every node. Therefore, the equations hold for the condition that the sum of all currents flowing in or out

a node have to be zero. The nanowire network system only consists of resistors and a probing current source which exhibit a linear behavior. In doing so, a linear system of equations is achieved. Subsequently, the equations are solved by finding correct voltage variables V_x ($x = 1, 2, 3, \dots$) for every node.

More information about SPICE can be found in the book of Vladimirescu.^[214]

5.4 Solar Cell Characterization

JV Characterization

For the jV analysis two different set-ups are used. A manual system for 1 inch substrates is placed inside the glovebox at the UFO vacuum deposition system. It enables direct measurement of non-encapsulated solar cells without air exposure right after production. As sun simulator a SoCo 1200 MHD from Steuernagel Lichttechnik GmbH is utilized directly illuminating the sample with the intensity of 1 sun (AM1.5) calibrated with a silicon reference diode.

In order to measure larger amounts of samples automatically, the IV-robot is used. It consists of a sample holder with an automatic positioning system and a sunlight simulator 16S-003-300-AM1.5 (Solar Light Co.) illuminating the sample *via* a fiber. A silicon reference diode is used to calibrate the intensity. With this system, mismatch correction (see Section 2.3.4) can be achieved easily. First, the mismatch factor MM_{test} (corresponding AM1.5) for the OSC is calculated from an EQE measurement. The mismatch (MM_{Si}) for the silicon reference diode reveals to be 0.785. Second, the correct intensity is calculated following

$$j_{Si} = \frac{MM_{\text{test}}}{MM_{Si}}. \quad (5.7)$$

The intensity of the reference diode has to match j_{Si} that the OSC is generating the same amount of current as under correct AM1.5. Just by considering this fact, exact efficiency is obtained.

It is noteworthy that some samples are measured additionally with a mask of 1.88 mm^2 . Hence, the exact j_{sc} can be estimated excluding parasitic solar cell contribution. In particular, this step is necessary if the correct cell area is uncertain.

Chapter 6

Silver Nanowire Electrodes for Organic Solar Cells

As laid down in Section 3.4 on the state of the art in solar cell electrodes, silver nanowire networks fulfill all requirements for an application as highly conductive transparent electrode. In 2008 and 2009, publications introduced this electrode to the scientific community, focusing on the operating principle.^[52,96] Still, there exist a lot of points worth to screen for improvements. In particular, the implementation of the network into organic solar cells needs further research to achieve satisfying efficiency values.

In this chapter, the whole process chain of producing and implementing a transparent silver nanowire electrode into an small-molecule organic solar cell is described and improvements are demonstrated. In the first section, two appropriate deposition methods are demonstrated. Afterwards, the focus shifts towards the inherently rough topography and a possible planarization approach is pointed out. The subsequent structuring process revealed some challenges and therefore is stressed in the third section. In the last section small-molecule organic solar cells are deposited on top of these electrodes with variations in the layer structure.

In this chapter we focus on silver as standard nanowire material, whereas both commercial and self-synthesized nanowires are utilized.

The majority of the chapter content was published in *Organic Electronics*, 14, 143–148 (2013).^[215]

6.1 Deposition

Dispersions for production of nanowire electrodes (*e.g.* Cambrios ClearOhm^[216]) are already available and enable an easy deposition *via* common lab-methods such as spin-coating.^[41,101] However, these commercial products are specially tailored for the uti-

lization in electrodes. They contain many unknown components to allow a proper deposition (for instance a viscosity matrix and various additives^[217]). Therefore, these dispersions are less useful in order to reach a deeper process understanding.

Suppliers which offer untailed dispersions without additives typically use simple alcohols (*e.g.* ethanol, isopropanol) as standard solvent. These solvents result in sufficiently stable dispersions even for longer time-spans, which is also observed in our synthesis approaches.

It would be favorable to deposit the nanowire networks directly from these alcohol dispersions so as to avoid a higher process complexity originating from extra processing steps. Moreover, after solvent evaporation no residuals remain on the network and the nanowires stay unchanged in an original state (as synthesized) which is advantageous when investigating further post-treatment processes.

6.1.1 Dip-Coating

Motivated by former publications,^[96] first deposition tests are done with shaking plates and drop-coating. The dispersions wet the substrate sufficiently (tested for ethanol and isopropanol). The low boiling point of the solvent enables a fast evaporation even at room temperature. Nonetheless, Figure 6.1 clearly shows that these methods do not perform well concerning the achieved final film quality. During the evaporation

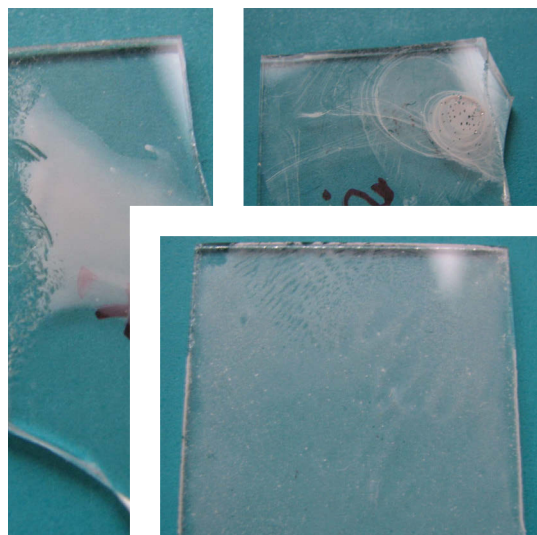


Figure 6.1: Photographs of inhomogeneous nanowire distributions on various drop-coated samples dried at air without shaker. Distribution gradients, agglomerations and ring-structures are visible.

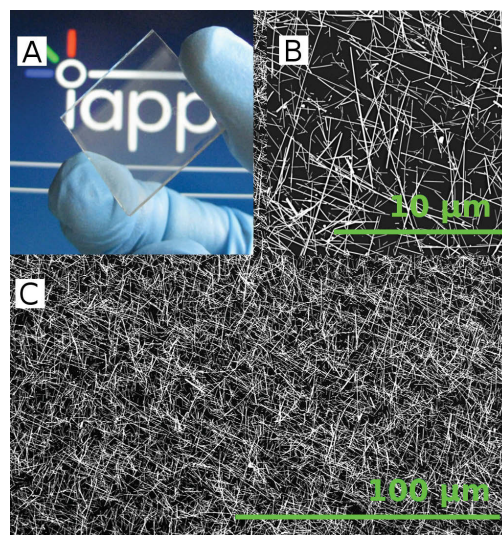


Figure 6.2: A: Photograph of dip-coated sample (upper 5 mm are uncoated). B: SEM picture of a dense NW electrode (120 cycles, 0.1 cm/s, 0.6 mg/ml in EtOH) (C: at lower magnification).

of the solvent film, the local concentration is unstable and material fluctuations can

be observed in the liquid film. In such thin films the interaction of viscosity, concentration, surface tension, evaporation and capillarity induce liquid flows which lead to material re-organization. As a consequence, the wires are transported within the film and inhomogeneous distributions occur after the evaporation process. Such effects are well known for nanoparticle dispersions (i.e. coffee ring effect^[218]). Thus, these kind of methods can be labeled as not appropriate for homogeneous network deposition.

In order to minimize the issue of inhomogeneous wire re-distribution, the wet film has to become thinner. This would accelerate the evaporation of the solvent and therefore decreases the time for wire transport. Moreover, thinner liquid films can suppress flow effects due to an increased interaction with the substrate.^[219] Additionally, in thin liquid films the movement of the long wires might be hindered. Dip-coating as typical lab method seems to be a perfect choice to fulfill these requirements.

As depicted in Figure 6.2, the dip-coating approach results in completely homogeneous films, both in the macroscopic (A) and microscopic regime (B, C). Therefore, the quality is suitable for the usage as network for electrode applications. Along with glass, this kind of networks are achieved on various substrates like PEN, PET, and commercially treated plastic foils. A detailed description of the process scheme is presented in Section 5.1.

Figure 6.3 demonstrates the dependency between the transmittance and the dipping cycles. A linear relation between surface coverage and transmittance can be assumed

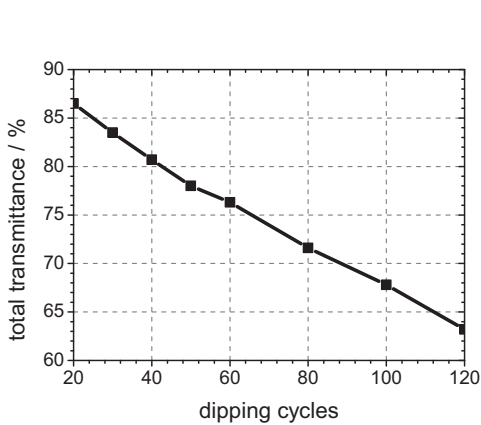


Figure 6.3: Total transmittance of deposited AgNW films (incl. glass) at 550 nm over the number of dipping cycles is presented.

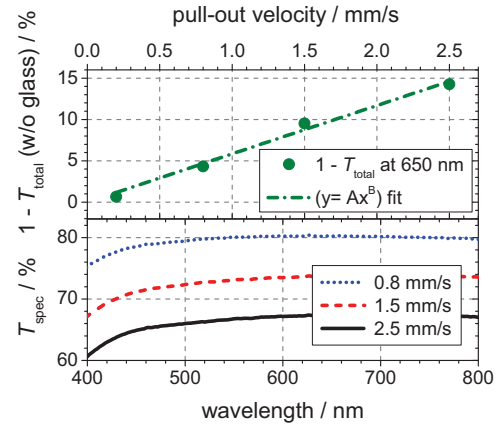


Figure 6.4: Bottom: specular transmittance spectra of networks deposited at various pull-up velocities (90 cycles). Top: transmittance loss (at 650 nm) vs. velocity incl. ($y = a \cdot x^b$)-fit.

as simple approximation for low nanowire densities (NW density $n_w \sim (1 - T_{\text{total}})$), see

also Section 8.1.2). Thus, the graph proves that each dip adds the same amount of wires to the network. The observed absence of any build-up effects demonstrates that the wires perfectly adhere to the substrate. They are not re-dispersed in the solvent if once stuck on the substrate. The deposited density per dip is just determined by the amount of wires which are dispersed in the thin solvent film remaining on the substrate after being pulled out of the dispersion reservoir. The sufficient wire-substrate adhesion is caused by the high surface-volume ratio of particles in the nanometer regime, which was already described in literature. In detail, the forces are quite complex and difficult to measure.^[220,221] It has to be mentioned that the wires stay dispersed and refrain from adhering to the substrate as long as the solvent is not fully evaporated. In this case, rinsing the substrate will wash away all wires. Due to adhesion mechanisms, the method works for many substrates as long as the solvent wets the surface and the wires attach to the surface after solvent evaporation. The experiments with plastic foils suggest that these requirements are fulfilled for many important substrates. As a consequence, no further surface treatment such as the application of poly-lysine^[70,222] is necessary.

Aside from cycle number, the pull-out speed influences the nanowire density, as it affects the solvent film height. In theory, the film height h of the solvent should follow the Landau-Levich relation^[223,224] for continuous pull-out

$$h \sim \frac{(\eta v_{\text{pull}})^{2/3}}{(\rho g)^{1/2} (\gamma)^{1/6}} \quad (6.1)$$

with gravity g , pull velocity v_{pull} and the liquid parameters (surface tension γ , viscosity η , and density of the liquid ρ).

Figure 6.4 shows the specular transmittance spectra for films coated at various pull-out velocities. In addition, the top graph presents the transmittance losses ($1 - T_{\text{total}}$) for a wavelength of 650 nm plotted against the velocity. Bearing the previous conclusions in mind, nanowire density should be directly related to the liquid film height during dipping. Therefore, Equation 6.1 should characterize the graph. Although theory predicts $h \sim v_{\text{pull}}^{2/3}$, the corresponding fit with $y = a \cdot x^b$ reveals an almost linear behavior with an exponent of $b = 1.0 \pm 0.1$ within the investigated region. Thus, nanowire deposition is faster than expected by Equation 6.1.

One reason might be the small sample size. The formula was derived for a continuous pull-out process of large substrates. In contrast, on small substrates the film does not reach equilibrium state. In general, the film thickness is higher and consequently, the formula underestimates the nanowire density. Additionally, various ‘thickening’ effects

are described in literature.^[225–227]

The investigated velocities represent the practical range of the utilized set-up. Velocities below 0.2 mm/s result in time-consuming deposition times (long cycle-times combined with low deposition per cycle) and values above 2.5 mm/s produce large inhomogeneous areas at the sample edges due to the high film thickness. However, for larger substrates also faster deposition should be possible. Nevertheless, there will be a speed limit above which the thin film formation collapses due to the complex inherent forces in the film.

The last parameter which affects density is the nanowire concentration. Because of the high material consumption, this experiment was not carried out and instead fixed values of 0.5 to 1 mg/ml are used. However, our findings suggest a linear dependency with growing material deposition for an increased concentration until the wires affect the dispersion properties (*e.g.* viscosity) at higher concentrations.

In contradiction to alternative deposition methods described in literature for dip-coating, neither complicated filtering or surface manipulation is necessary^[52,70] nor has the dispersion to be tailored in a time-consuming way to gain correct viscosity values, as required for spin-coating,^[41,101] which cannot easily be scaled anyway. The deposition of NWs directly on top of substrates without modification ensures an easy and fast screening of newly synthesized wire types in the lab and allows scaling into larger substrates and higher throughput without any changes in the fundamental deposition mechanism.

It has to be mentioned that depending on deposition conditions, the networks show a more or less pronounced anisotropic effect. In this chapter, random networks are discussed. Therefore, in order to achieve stable semi-isotropic networks with almost random alignment, the substrate is turned by 90° after half the dipping cycles has passed. However, a slight anisotropy can also be seen in Figure 6.2 at the second glance. Nevertheless, the transmittance and conductivity of these semi-random networks reveal just small differences compared to the fully random case which are neglected in this study. This issue is briefly addressed again in Chapter 8.

Finally, some comments on the implementation of the dip-coating process to industrial large-scale manufacturing are provided. We mostly use about 30 to 40 cycles to achieve suitable nanowire densities with relatively low concentrations around 1 mg/ml. Most likely, an increased nanowire amount up to 10 mg/ml (like present in

the as-purchased Bluenano dispersion) might be possible without changing dispersion behavior, although this was not carried out in our tests. Furthermore, the experiments revealed that an increased velocity leads to a rising deposition amount with an exponent higher than the theoretical $2/3$. Thus, in general, an increased pull-out speed increases both the throughput and the thickness. Consequently, a much smaller cycle number can be obtained and even a ‘one’-dip process might be possible. Moreover, the dipping process can be included into a continuous roll-to-roll in-line set-up.^[228]

6.1.2 Influence of Air Humidity

Occasional observations showed that a high water content in the dispersion disturbs the film formation regarding homogeneity. The SEM image in Figure 6.5(a) depicts an acceptable film, whereas the film in (b), which is deposited at high air humidity, demonstrates an extremely disturbed film with a lot of agglomerates. Thus, the

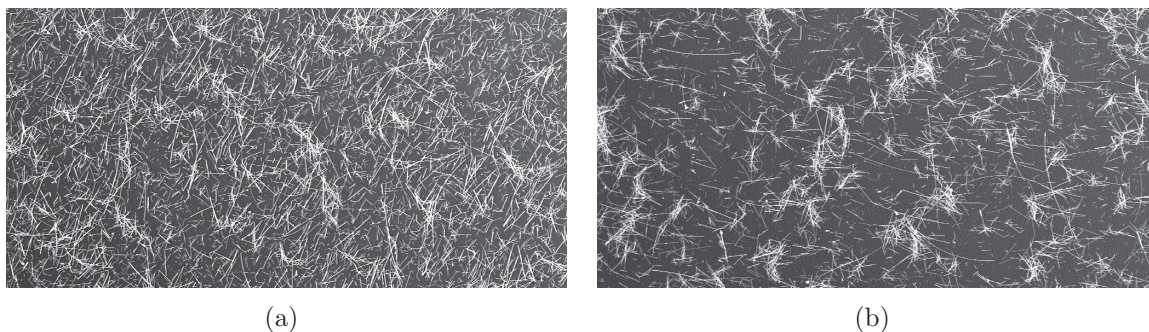


Figure 6.5: $200 \times 100 \mu\text{m}^2$ SEM graph of dipped nanowire films on a warm humid day. a) fresh dispersion, with plasma cleaning, decreased air humidity by silica gel b) dispersion stored for 1 d, w/o plasma treatment, high humidity. Both films are dipped without sample rotation and therefore appear to be slightly anisotropic.

influence of water on the film formation is investigated.

In general, ethanol is hygroscopic and it is miscible with water in arbitrary ratios. Water can either be absorbed directly from the air during deposition (high air humidity) or it is already absorbed in the dispersion before deposition (long storage in air).

At first, the former is examined, producing films at varying air humidity. The tuning of the water content is achieved with silica gel ($13\%_{\text{RH}}$) and a saturated $\text{Mg}(\text{NO}_3)_2$ -water solution^[229] ($60\%_{\text{RH}}$), while $37\%_{\text{RH}}$ are observed in air without manipulation. Figure 8.3 displays the SEM images of the films from low (left) to high (right) air humidity. More quantitative data to this experiment can be found in the anisotropy Section 8.1.1.

Towards higher air humidity, more and more clusters appear. Although the clusters

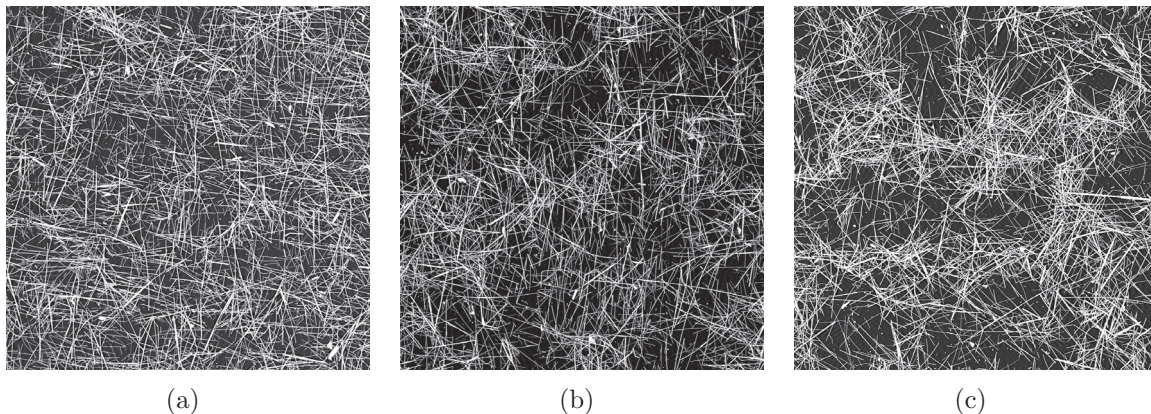


Figure 6.6: $80 \times 80 \mu\text{m}^2$ SEM images of dip-coated (90° rotated) NW films produced in an atmosphere with an air humidity of 13%, 37%, and 60%.

are not as prominent as in Figure 6.5(b), the agglomeration effect is already visible. It is noteworthy that the clusters are not very dense (compare with Figure 6.5) and rather regions with slightly higher and lower NW density appear.

A possible hypothesis, which can explain the origin of the agglomerations, is attributed to the surface tension. Ethanol and water show strongly deviating surface tension values of $\approx 22 \text{ mN/m}$ *vs.* $\approx 72 \text{ mN/m}$.^[230] Nevertheless, small amounts of water in ethanol ($< 10 \text{ vol}\%$) have only a negligible effect on the surface tension of the blend (see literature table^[230]) and thus no influence is expected. However, the liquids form an azeotrope^A at a molar mixing ratio of about 1:10 (water:ethanol) with slightly decreased boiling point.^[231] This issue has crucial consequences for the evaporation process. The corresponding vapor-liquid-equilibrium (VLE) diagrams are shown in Figure 6.7. Around the azeotropic point at high ethanol mole fractions, the composition of liquid and vapor are almost similar. Therefore, ethanol and water evaporate in similar quantity as can be seen in Figure 6.7(a). In contrast at water contents above 40 mol%, the ethanol evaporation is preferred and the vapor is ethanol-rich. As a result for small reservoirs, the water remains in the liquid and leads to an increased water concentration. As visible in Figure 6.7(a), the effect increases for higher water ratios and thus water accumulation is accelerated during evaporation. In consequence, the region above 30 mol% water is problematic for the nanowire deposition. The ethanol vaporizes much faster than water, water is accumulating in the dispersion film, and finally even a water film is formed. In an extreme case (i.e. sample demonstrated in Figure 6.5(b)) the water-rich phase can even be distinguished

^ATwo liquids form an azeotrope when the vapor of the boiling mixture consists of the same material ratio as the unboiling mixture. The azeotropic blends behave like a liquid consisting of a single component. An azeotrope cannot be separated by simple distillation and thus, its component ratio represents the highest possible purity which can be achieved without more sophisticated methods.

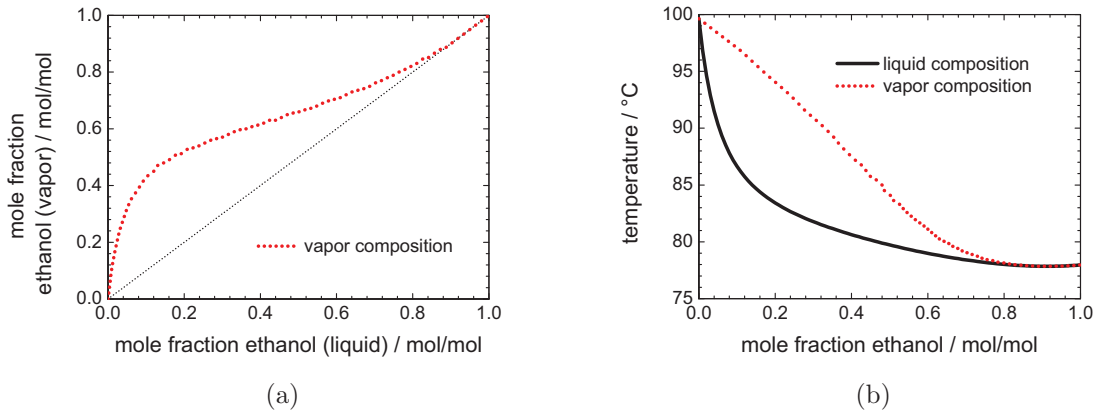


Figure 6.7: X-y VLE diagram (a) and T VLE diagram (b) of an ethanol-water mixture (1 bar). Source: Dortmundener Datenbank and ChemSOF.^[232,233]

from the ethanol phase. After a first contact line (ethanol-water mixture) has passed, a film remains which evaporates some seconds later causing a second contact line (water-rich film). This effect is caused by the rapidly increasing evaporation temperature demonstrated in Figure 6.7(b) for water concentrations above 90 mol%.

The high water contents change the deposition behavior completely. The surface tension comes closer to that of water, which influences the wetting of the substrate and causes inhomogeneous distributions (*e.g.* droplet structure) in the microscopic (when the effect is still small as in the Figure 6.6 (right)) and macroscopic (higher water contents completely destroy the film) regime. Among the surface tension effect, the high water content might also limit the dispersability of the NWs. However, in this case more dense clusters would be expected because of typically strong clustering effects of nanoparticles.

Similar experiments are also performed for the second absorption mechanism when water is directly absorbed by the dispersion reservoir at long storage times. Therefore, various amounts of water are added to the dispersion. In this experiment no gradual effects are visible. In contrast, an abrupt increase of the cluster density is observed at water concentrations of about 0.6 vol%, below the azeotropic point at about 4 vol%. Furthermore, the clusters are much more dense and therefore a lowered solubility might be present^B.

In consequence, the water adsorption in the thin ethanol film during deposition seems to be the main reason for the high water contents and the resulting film disturbance. The high surface-to-volume ratio of the thin dispersion film should support the absorption.

^BDuring addition higher water concentrations can be reached. Therefore, further experiments are necessary in order to obtain critical water ratios.

The large amount of clusters might also have an effect on the transmittance behavior. Figure 6.8 shows the corresponding transmittance data for samples depicted in Figure 6.6. The film with better homogeneity (13%_{RH} sample) exhibits a higher

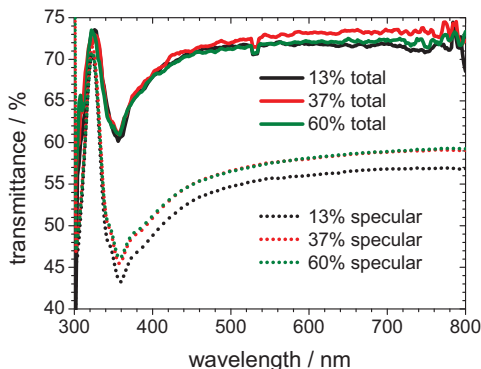


Figure 6.8: Specular (dotted) and total (solid) transmittance of dip-coated nanowire networks for varying air humidity.

ratio of scattered light transmission. However, the effect is rather small and further experiments are necessary in order to confirm these results. Nevertheless, this behavior provides a possible explanation for observations made by Hu *et al.* They described a strongly fluctuating HAZE for spray-coated NW films.

In conclusion it has to be emphasized, that humidity has to be avoided. First of all, the water concentration in the dispersion prior to dipping has to be low in order to avoid dispersability issues. Secondly, during deposition in the thin ethanol films small ratios of water might have large impacts. Nonetheless, as long as the water concentration stays lower than at the azeotropic point no problems occur.

6.1.3 Spray-Coating

Although the dipping process is scalable and fast, the scale-up process in the lab is rather difficult. In particular, the production of large amounts of single samples is either time-consuming (low concentration) or material intensive^C (high concentration). Thus, the results of the dip-coating experiments are transferred to a spray-coating method. This should enable a homogeneous deposition of large substrates (or many similar small ones) and additionally it speeds-up the production with low material consumption. Concerning the deposition physics, the methods should be comparable,

^CDuring dip-coating the dispersion gets spoiled due to agglomeration effects. Therefore, the utilized dispersion cannot be re-used many times.

since a thin liquid film containing the nanowires is applied to the substrate. Subsequently, the wires stay adhered to the substrate as it is the case for dip-coating.

All experiments and results of the investigations can be found in the diploma thesis of Carsten Häfner^[234] (supervised as part of this thesis), who set-up and examined our spray-coating system (introduced in Section 5.1). In the following paragraph only a comprehensive overview of the main results is demonstrated.

In order to achieve a thin solvent film as required for a homogeneous network, the deposition amount of solvent has to be adjusted accordingly. For instance, this can be achieved by varying the distance between nozzle and substrate as it is demonstrated in Figure 6.9, whereas the nozzle x-y position is fixed. The left picture (small distance)

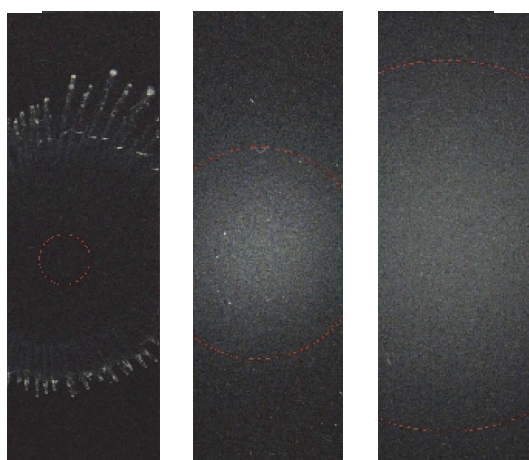


Figure 6.9: Photographic picture of material distribution after deposition w/o moving for varying distance (left to right) of 2.5, 10 and 17.5 cm (picture height: 4.75 cm).

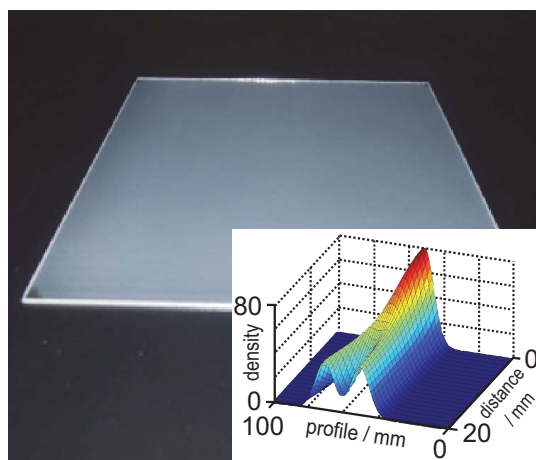


Figure 6.10: Spray-coated NW film on $15 \times 15 \text{ cm}^2$ glass substrate. Inset: Simulation image to find an optimized line distance for two lines in order to achieve a rather flat plateau enabling homogeneous deposition.

illustrates a ring structure where most of the wires are deposited at the edge. In this case the generated liquid film is too thick and consequently, is affected by the coating gas stream (blow effect). The picture in the middle (increased distance) exhibits an almost defect-free film. However, at second glance, some cloudy structures are visible in the center. Hence, the film thickness is still too high and the film gets unstable. As a consequence, droplets are formed causing defects during the drying process^D. In contrast to the former, the right picture shows a film where dispersion deposition and solvent evaporation are well balanced. Here, neither in the macroscopic nor in the microscopic regime defects are visible.

^DIt has to be mentioned that the coating gas flow in our set-up is quite strong and therefore might have a negative effect on the film stability.

As expected, the dispersion shows the same behavior as for the dip-coating process. A well adjusted set-up produces a thin liquid film. After solvent evaporation the wires stick to the substrate. Process speed can be increased by putting the sample on a hot-plate during coating, which further accelerates solvent evaporation and thus allows faster material deposition.

The spray-coating spot is rather limited in radius and shows a certain distribution with a density drop towards the edge (see Figure 6.9). Therefore, in order to produce large homogeneous films, the nozzle has to scan over the substrate in a line pattern. The track distance (pitch) has to be adjusted according to the line profile to obtain a homogeneous density. For instance, the inset of Figure 6.10 demonstrates a corresponding calculation to estimate the required line pitch (two lines). In addition, the figure depicts a nanowire film on a $15 \times 15 \text{ cm}^2$ glass substrate spray-coated at optimized parameters.

Measuring the transmittance and resistance over such a large spray-coated electrode revealed a satisfying homogeneity in the middle of the area as presented in Figure 6.11. However, in particular at the edges, deviations occur and homogeneity is a permanent

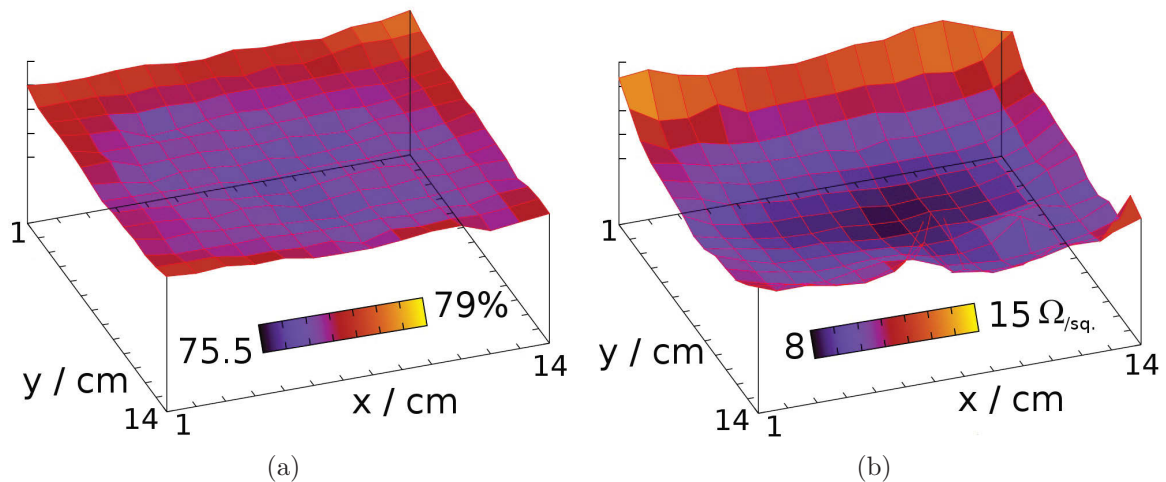


Figure 6.11: Homogeneity plot for the transmittance (a) and sheet resistance (b) corresponding to the electrode presented in Figure 6.10.

concern. Therefore, all samples have to be coated beyond the edge in order to achieve a constant plateau and guarantee homogeneous network deposition.

Although it is more complicated to obtain homogeneous films by spray-coating than by dip-coating, the advantages prevail for larger tests with many similar substrates.

6.2 Post-Treatment

Because of the NW ligand shell, the as-deposited thin films show a high sheet resistance and post-processing steps are necessary to reduce them. Since through thermal annealing promising results were achieved,^[96] we have investigated the annealing step in more detail.

Figure 6.12(a) displays the dependence of resistance on the annealing time for temperatures between 180 and 240 °C in air for dip-coated Bluenano wires (1st batch). Until saturation is reached, conductivity tremendously improves by annealing. Higher temperatures accelerate the process, but finally result in equal conductivity values. However, if the annealing period is too long, the resistance starts to increase again, as can be seen in the inset of Figure 6.12(a). This is caused by so called Rayleigh

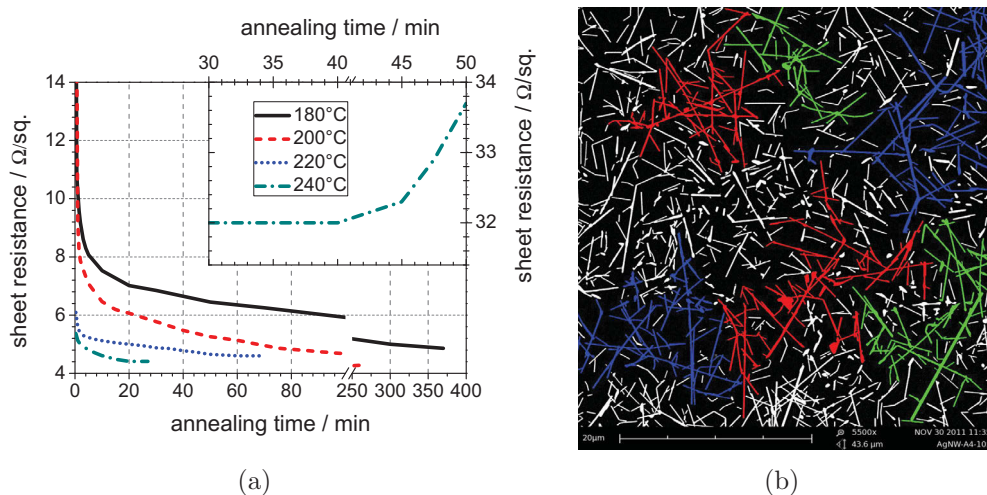


Figure 6.12: a: Sheet resistance *vs.* annealing time behavior of dip-coated 90 nm diameter nanowire networks for various temperatures between 180 and 240 °C in air. The inset illustrates the onset of degradation for another sample (less dense network) annealed at 240 °C for longer annealing times. b: $40 \times 40 \mu\text{m}^2$ SEM picture of a nanowire network after long annealing times of about 3 h at 210 °C. Still connected large NW islands are colored by a simple filling algorithm to illustrate the percolation effect. In-between regions of isolated wires interrupt the electrical contact.

instabilities in the nanowire structure,^[235] which lead to coalescence effects^E and network interruptions, as can be seen in Figure 6.12(b).

It is noteworthy that at elevated temperatures, an accelerated oxidation of silver has to be considered. However, silver oxides (mainly Ag_2O) decompose at temperatures above ≈ 240 °C.^[236] The exact kinetics are not known in particular, because changes regarding the nanostructure might occur. Nevertheless, a change in color or spectrum is not observed — silver oxides appear to be black. Therefore, just some monolayers

^EThe nanowire structure is destroyed and clusters with minimized surface are formed.

of oxide are expected.

Furthermore it has to be mentioned that in experiments with other nanowire batches (Bluenano and self-synthesized batches), strong deviations in the annealing curves are found. Thus, although the conclusions (faster process with $T \uparrow$, minimum T -independent) are still valid, the curves in Figure 6.12(a) do not reflect a general shape. For instance in Figure 6.13, annealing curves for self-synthesized nanowires are presented. Whereas the 180°C-sample shows a similar behavior as seen in Figure

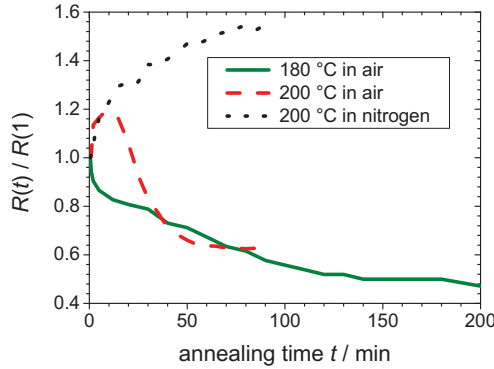


Figure 6.13: Annealing curves for self-synthesized AgNW batch 2 at 180°C in air (green solid), 200°C in air (red dashed) and 200°C in nitrogen (black dotted). The samples are spray-coated and the 2-wire mode resistance $R(t)$ is normalized with the value after one minute $R(1)$.

6.12(a), the 200°C-sample exhibits a completely different shape. Such deviating behavior is also observed for batches from Bluenano.

The origin of the improvement in general and the deviations in particular are not yet cleared up. However, samples annealed in nitrogen instead of air revealed that, at least, one decisive part of the effect is oxygen-mediated. Figure 6.13 illustrates the resistance improvement in air compared to a nitrogen atmosphere, whereas much lower resistance values are reached. Moreover, in the first minutes of the 200°C-samples, the shape of the curves seems to be similar which might be caused by a superposition of at least two processes. Possible contributions to this behavior might be *e.g.* auto-ignition, desorption of the surrounding molecular ligand shell, rearrangement of the shell when reaching the glass transition temperature ($T_g(\text{PVP}) \approx 180^\circ\text{C}$)^[237] or interactions with the substrate, whereas the oxygen process is assumed to be essential for gaining a low contact resistance at the junctions.

As an alternative to annealing, plasma treatment with argon was also investigated. However, the reproducibility in our set-up was not sufficient and, compared to the

heating step, the achieved enhancement was quite small. Therefore, an annealing step was still necessary.

6.3 Performance

By post-annealing, the contact between the wire junctions is enhanced and thus the network conductivity can be improved tremendously while the transmittance remains constantly high. The resulting performance curves^F for three dip-coated NW networks (all with Bluenano nanowires) are depicted in Figure 6.14a. The curves demonstrate the improvements which are achieved during this work. Here, the transmittance value

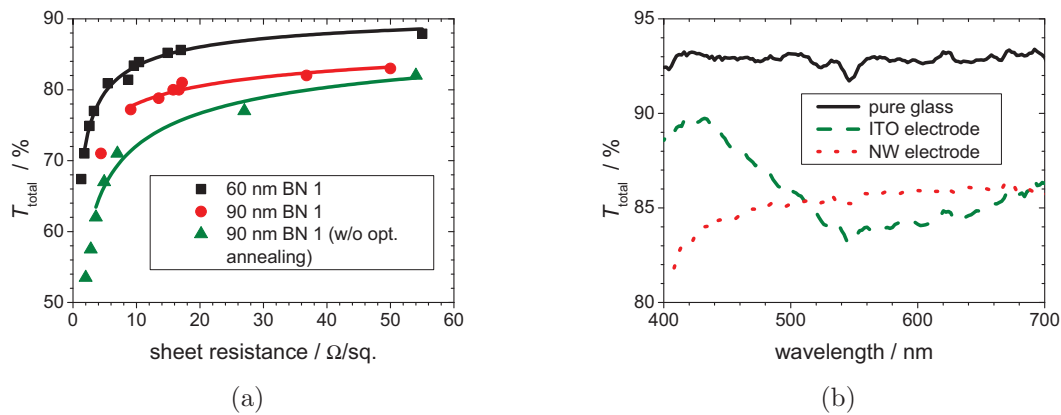


Figure 6.14: a: Performance graphs (total transmittance *vs.* sheet resistance) of 90 nm (before and after annealing optimization) and 60 nm nanowire networks. The total transmittance curves are fitted with a figure of merit function for percolated networks. b: Total transmittance spectra of a NW covered glass, an ITO reference with similar conductivity of 17 $\Omega/\text{sq.}$ and the bare glass itself.

at 550 nm is used, since the transmittance variation between 400 and 800 nm is rather small as presented in the neighboring Figure 6.14b. The green triangles represent the starting point of our research with nanowires of 90 nm in diameter and without an optimized annealing step. The red circles and the black squares demonstrate values for a 60 nm (about 10–15 μm long) and 90 nm (about 5–10 μm long) batch after optimization. The longer and thinner the wires, the better is the network performance. A result which was also observed by other groups both in experiment and simulation.^[100,161]

A figure of merit (see Equation 4.6) by De *et al.* is used for the evaluation of the percolation network.^[91] Whether the graphs are correctly described by this approach, is

^FThe total transmittance against the sheet resistance represents the main property of a transparent electrode. The curve is showing the values depending on the coverage.

checked by logarithmic graphs described in Section 4.1.2. Unfortunately, these graphs do not exhibit clear regimes (bulk *vs.* percolation). Nevertheless, deviations from a linear behavior are observed. Therefore, the fit region in Figure 6.14a is constrained and points at high densities, which might belong rather to the bulk regime, are ignored. The fitting of the assumed percolation regime in Figure 6.14a (solid lines) results in Π values of 156 and 36 for the 60 and 90 nm sample, respectively. Hence, the thin wire batch results in better values than presented in the review table by De *et al.*, whereas the highest nanowire value is 32.^[91] In consequence, the herein investigated nanowires exhibit a superior percolation behavior caused by a better aspect ratio.

Our best NW electrode batch reveals values of $< 20 \Omega/\text{sq.}$ at $> 85\%$ transmittance (92% after substrate subtraction) and therefore can compete with state of the art ITO films both in conductivity and transmittance, which is demonstrated in Figure 6.14b. The same comprehensive picture can be obtained by focusing on the commonly used figure of merits for transparent electrodes. The best 60 nm NW batch (our ITO) achieves at a sheet resistance of $15 \Omega/\text{sq.}$ ($17 \Omega/\text{sq.}$) and an averaged transmittance from 400 to 800 nm an T^{10}/R_s of $0.028 \Omega^{-1}$ (ITO: $0.028 \Omega^{-1}$) and an σ/α of $0.81 \Omega^{-1}$ (ITO: $0.82 \Omega^{-1}$) while it has to be stressed that the comparison are limited to this certain resistance.

6.4 Solar Cell Integration

6.4.1 Planarization

A closer look at the electrode nanostructure *via* SEM and AFM (see Figure 6.15A) reveals that the wires are well attached to the substrate and even bend back to the surface. The effect is caused by the combination of flexible thin wires and high adhesion forces, which was already mentioned in Section 6.1.1. Although the wires do not tend to poke out of the film, the nanowire grid shows an inherently rough surface. In particular, agglomerates which can result in large steps up to several hundred nanometers (see Figure 6.15), cause device damage. Therefore, the deposition of sm-OSC directly on top of the conductive network (investigated up to 100 nm HTL) leads to devices that are immediately short-circuited.

In order to address this issue, planarizing PEDOT:PSS layers are spin-coated upon the NW network. As demonstrated in Figure 6.15 B/C, the height of individual wires above the surface drops slowly with an additional PEDOT:PSS layer and, probably even more important, the spin-coated polymer smooths the edges of the wires as the

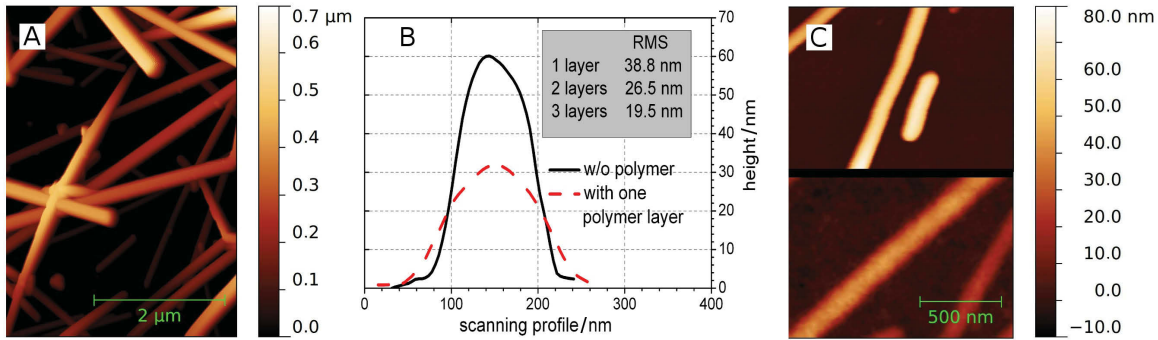


Figure 6.15: A: $5 \times 5 \mu\text{m}^2$ AFM image of a dense grid demonstrating a bended nanowire. B: Averaged AFM cross section scan with and without polymer of 5 different single nanowires is presented. C: The corresponding $2 \times 2 \mu\text{m}^2$ AFM images (top: without PEDOT:PSS, bottom: covered with a single PH1000 layer (2500 rpm, about 40 nm high)) are shown. Zero is set to the area between the wires. Additionally, the inset table in B demonstrates the decreasing roughness with increasing number of layers measured at $50 \times 50 \mu\text{m}^2$ AFM graphs.

AFM profile scans illustrate. In particular, defects such as wire agglomerates are covered well. Although the feature height of the network including a PEDOT:PSS layer is still high, smoothing and broadening of the structure results in a sufficiently flat surface topography. As expected, more and thicker layers can decrease the roughness even further (see root mean square (RMS) table inset of Figure 6.15B).

However, simultaneously the parasitic absorption of the PEDOT:PSS film decreases the electrode transmittance, as presented in Figure 6.16. The first ≈ 40 nm layer

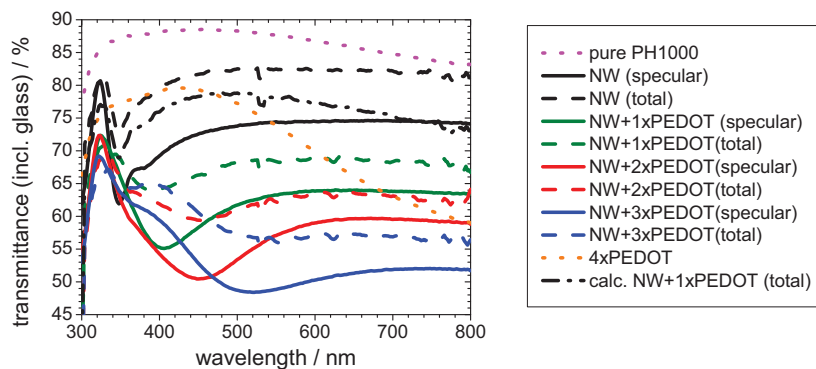


Figure 6.16: Different transmittance spectra (total and specular) for a nanowire network with and without PEDOT:PSS layer. Moreover, the pure PEDOT:PSS transmittance is plotted and simple calculations adding PEDOT:PSS to a NW network are done.

PH1000 decreases absolute transmittance by about 15% (black *vs.* green), which is more than expected. In comparison, a pure 40 nm PH1000 layer (spin-coated at 2500 rpm) on glass (magenta dotted) just causes about 5% (averaged and absolute)

losses with a stronger absorption in the longer wavelength region. The calculated addition of the pure PEDOT:PSS layer spectrum to the bare NWs (black dashed) leads to a completely different spectrum (black dash-dotted) than the measured curve (green dashed) with a factor of 2–3 in-between the values. Therefore, the absorption of PEDOT:PSS alone does not explain the strong drop.

Additionally, more layers are coated on the nanowires corresponding to the RMS values in the table of Figure 6.15B. The thicker samples show again an excessive transmittance decrease. Moreover, a clear shift of the transmittance dip is observed. The shift from 350 nm \rightarrow 420 nm \rightarrow 450 nm \rightarrow 520 nm is related to the change of the dielectric environment of the nanowire (see Section 4.2.2). Nanoparticle absorption shifts towards longer wavelength for surroundings with increasing refractive index, which is the case for air (1.0) and PEDOT:PSS (\approx 1.5). As long as the layers are rather thin (less material is deposited on top of the wire), additional layers are still changing the environment until the field amplitude of the plasmonic oscillation is not affected anymore.

However, this effect cannot motivate the large drop in the overall transmittance. Most likely due to scattering at the nanowire network structure, waveguide modes are coupled into the glass-PEDOT structure and therefore increasing the transmittance losses, as described in Section 4.2.2. It is noteworthy that adding an organic solar cell on top of the electrode might change the situation completely. The refractive index of the organic materials are typically larger than the 1.5 of PEDOT:PSS and therefore light can couple to the solar cell structure. Thus, measurements might underestimate the transmittance of the PEDOT-NW composite.

Nevertheless, light transmission is lost and hence a trade-off between planarization quality and transmittance drop is necessary. In order to improve planarization, the film thickness has to be increased. At the same time, additional transmittance losses have to be avoided and a certain conductivity of the layer is needed.

As a possible approach, transparent polymers are mixed into the commercial PEDOT:PSS solutions. It turned out that polyvinylpyrrolidone (PVP)^G is a promising candidate. The solid dissolves quickly in water and therefore could be mixed in the PEDOT:PSS formulations Clevios PH1000 and VPAI4083 solutions (both from Heraeus) by stirring. With the addition of an increasing amount of PVP the spin-coated layer height increases linearly, as shown for PH1000 in Figure 6.18 up to single layer thickness of 500 nm. During this film increase, the transmittance remains almost

^GPolyvinyl alcohol (PVA) was also examined but the solubility in the water-based PEDOT:PSS solutions is too low.

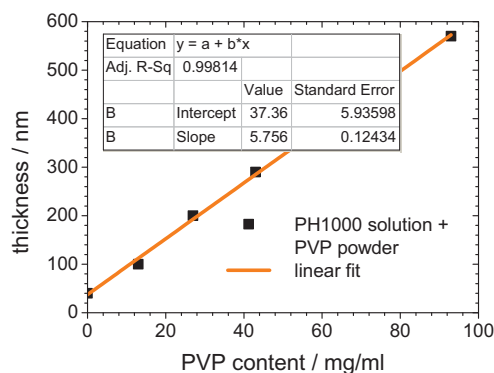
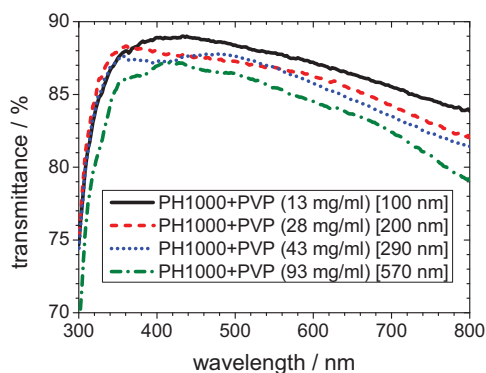


Figure 6.17: Transmittance spectra of various PH1000-PVP blends spin-coated on glass. (5000 rpm, 30 s, 120 °C)

Figure 6.18: Thickness against PVP content for the films shown in Figure 6.17 with a corresponding linear fit.

constant (thickness $\times 6$ vs. transmittance loss 2% absolute) whereas weak interference patterns become apparent in the spectra (see Figure 6.17). For both PEDOTs the resistance of the material blends are extremely high (hundreds of M Ω between two conductive silver points). The resistance of the PH1000:PVP-blend is lowered to the k Ω regime by adding ethylene glycol (EG).

Figure 6.19 shows the jV curves of ZnPc:C₆₀ solar cells deposited on such extended planarization layers. The applied interlayer is 280 nm thick. The cells with the

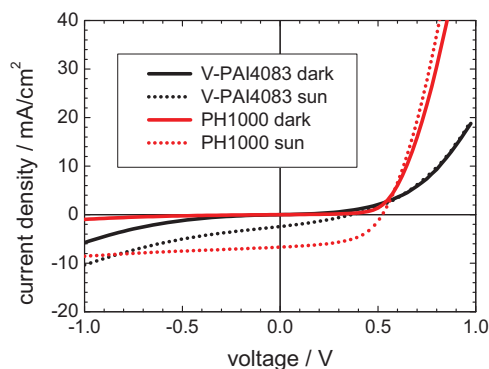


Figure 6.19: JV-curves in the dark and under illumination of p-i-i-ZnPc:C₆₀ solar cells including 50 nm HTL (see Section 5.2) on NW electrodes covered with 280 nm V-PAI4083-PVP blend (black) and 265 nm PH1000-PVP blend (red).

V-PAI4083 blend exhibit problems in current transport. The resistivity of the V-PAI4083 blend on glass is not measurable ($\rightarrow \infty$). An interlayer with such high resistance already causes unacceptable losses. In contrast, the cell with PH1000-PVP-EG layer demonstrates a promising shape^H. The conductivity of the interlayer

^HDue to problems with shunt path (see Section 6.4.2) at the laser edge, the cell cannot be compared to cells presented later in this thesis.

which reveals a value of 38 S/cm on glass, is sufficient for the integration into solar cells.

PEDOT:PSS is well-known in the field of organic devices since it is widely used in OSCs and OLEDs as injection layer. However, the system has some drawbacks. PSS as the counterion of PEDOT is strongly hygroscopic which might be of problem when working with water-sensitive organic devices.^[209] Moreover, it exhibits a high acidity which can harm the nanowire material (i.e. see Section 7.3.3). Therefore, alternatives have to be developed as it is presented in the diploma thesis of Ludwig Bormann^[238] which was supervised within this work. For example, planarization layers consisting of solution-processed small-molecule organics were produced. This interlayer result in a perfect smoothing of the nanowire structure and an ITO efficiency could be obtain on these composite electrodes. Furthermore, approaches for an integration without planarization were examined.

6.4.2 Structuring

After the application of the planarization layer, the composite has to be structured which turned out to be rather complicated. The aim is to achieve a pixel structure, as presented in Section 5.1 to include the electrodes in the IAPP process chain.

At the beginning, this is conducted through a Nd:YAG NIR laser scribing system. However, investigations of cells with various pixel sizes revealed different jV-curves, as presented in Figure 6.20 for areas of about 6 and 16 mm². Whereas similar current

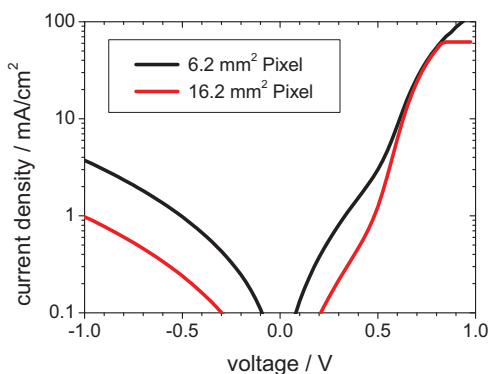


Figure 6.20: Semi-logarithmic jV-curves under dark conditions for the cells in Figure 6.21.

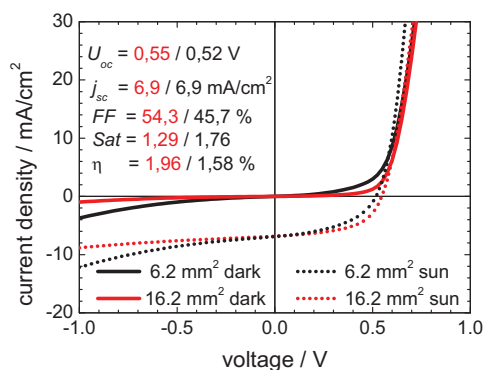


Figure 6.21: JV-curves for cells with two different pixel sizes with and without illumination. In addition, the corresponding cell parameters are presented.

densities can be observed at high voltages, in the reverse and low voltage regime the current density is much lower for the large pixel. This regions are dominated by

leakage currents. Thus, the majority of leakage currents flow through edge defects. The effect on the efficiency is demonstrated in the curves with illumination in Figure 6.21. The high leakage currents at negative bias are visible in this graph as well. In forward direction, the leakage currents cause a pronounced fill factor drop which decreases the efficiency.

This conclusion is supported by AFM and microscope images presented in Figure 6.22. Because of the thermal heating by the laser, the edge regions deform and bumps are

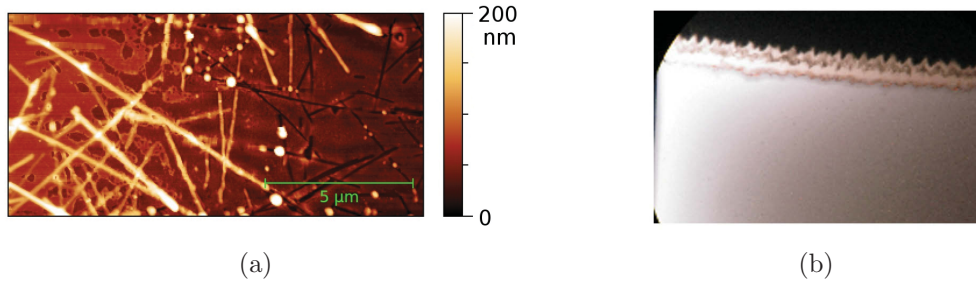


Figure 6.22: (a) The edge of an area structured with a Nd:YAG laser (left: un-processed region; right: processed region). The laser line width is about 70 μm and therefore just the line edge is visible. (b) Optical microscope-picture of a laser-structured pure PEDOT:PSS film (top: processed region).

formed as can also be observed for pure PEDOT:PSS films (see Figure 6.22b). Additionally, the PEDOT-NW composite consists of two different materials, which possess deviating absorption cross sections. Moreover, the used laser spot is about 70 μm wide. The spot has a typical Gaussian-like intensity distribution and therefore its intensity is lower in the outer regions. As a consequence, the nanowires and the polymer material are not removed homogeneously at all positions. In Figure 6.22a, edge nanowires remain present, while the PEDOT:PSS layer is being removed. PEDOT:PSS mainly absorbs above the red wavelength region (see Figure 6.16). In contrast, silver nanowires show a strong absorption at $\approx 320\text{--}400$ nm whereas higher wavelengths are mainly reflected. Thus, at the laser wavelength of 1064 nm, preferentially PEDOT:PSS is removed and higher intensities are required for silver. The uncovered nanowires result in a high roughness. As mentioned in the last section, this leads to shunt paths and therefore high leakage currents. Although the pure PEDOT:PSS film also shows a weak edge-leakage (see Figure 6.23), the uncovered nanowires in the laser-structured composite films cause an even stronger efficiency drop. The losses are not acceptable and impede the investigations.

Therefore, various structuring techniques are examined to improve the edge defects. Figure 6.23 shows the jV -curves for various structuring methods each measured

for three different pixel sizes. There is a distinction between active methods (as defined in the scheme of Figure 6.23), directly structuring the active area (laser scribing (355 and 1064 nm), scratching, orthogonal lithography) and passive methods, defining the areas by just covering the critical edges^I (sprayed lacquer, orthogonal lithography^J, SiO₂ sputtering, screen-printing, evaporation of high resistivity metal oxides). All methods mentioned in brackets are tested. However, the jV-graph in Figure 6.23

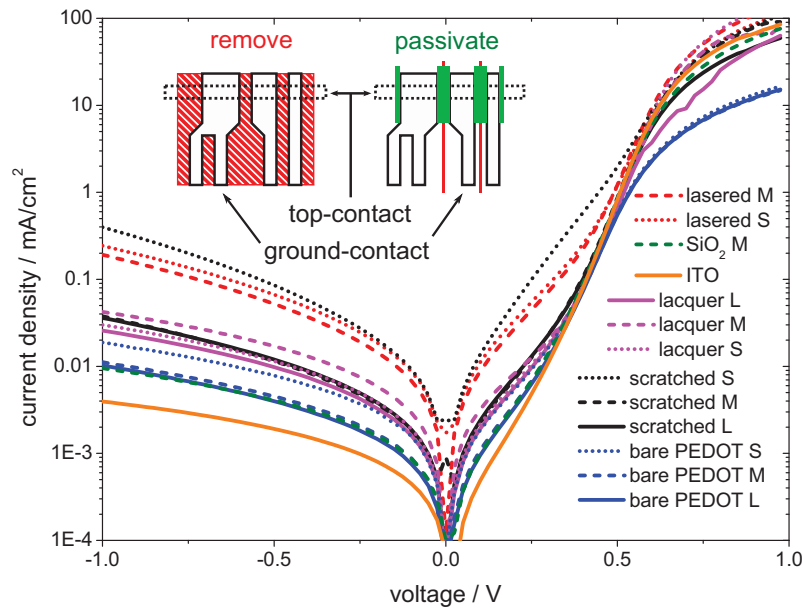


Figure 6.23: Semi-logarithmic jV-curves without illumination for various pixel sizes and structuring methods. The two schemes illustrate the active (left) and passive (right) structuring approach.

shows just fully operative samples. Among these samples the 1064 nm laser shows the worst performance. The passivation methods demonstrate the best results although reproducibility is not sufficient. The leakage currents for the passivated samples are about 1 to 2 orders of magnitude below the laser experiments. Furthermore, in particular the results for the spray-coated lacquer are almost area-independent. In order to transfer the passivation approach, to a more reliable technique a professional screen-printer is used. The passivation layers were printed by André Philipp at the Fraunhofer COMEDD in Dresden^K. The cells which are produced with this electrodes are shown

^IThe pixels are separated before by scratching or laser scribing and subsequently the pixel area is defined by the insulating passivation layer. Hence, the laser structures are covered with an insulating layer which should avoid the leakage.

^JThis method enables the lithographic structuring of organic materials.^[239] In our case a lift-off (passive) and an etching (active) method was used to achieve the required layout.

^KPrinter: EKRA X4 Professional, Paste: Peters SD2494NB-SM, Cycles: 1, Post-annealing: 50 min at 130 °C

in the next section.

6.4.3 ZnPc:C₆₀ Solar Cells with Varied HTL Thickness

A bulk heterojunction cell using ZnPc and C₆₀ for a 30 nm thick blended layer is chosen, as demonstrated in the inset of Figure 6.24. For comparison, reference cells on ITO electrodes without PEDOT:PSS interlayer are produced to evaluate the performance of the NW-PEDOT:PSS composite system. The sheet resistance is 27 Ω/sq. for the ITO and 25 Ω/sq. (81% transmittance, 90 nm batch, 30 times dipped, 1 mg/ml, 1 mm/s) for the NW electrode. For planarization one PH1000 layer (thickness about 40 nm) is spin-coated on the electrode. Additionally, the hole transport layer is varied to examine the influence of the stack height on the performance regarding the roughness issue.

The resulting dark *jV*-curves are plotted in Figure 6.24. The NW samples show higher leakage currents compared to ITO reference cells caused by shunting effects because of the rough nanowire electrodes. With increasing HTL layer thickness, the value of

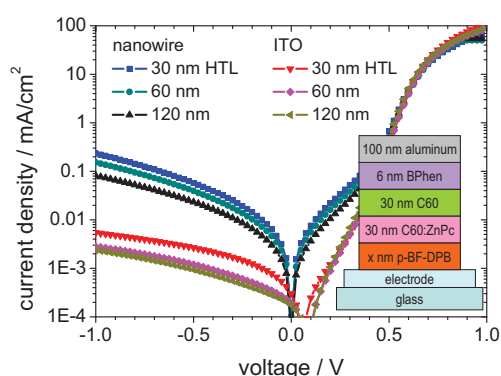


Figure 6.24: Dark current of solar cells with ITO and NW electrodes and different HTL thickness presented in a semi-logarithmic plot. The corresponding ZnPc:C₆₀ p-i-n stack is depicted in the inset.

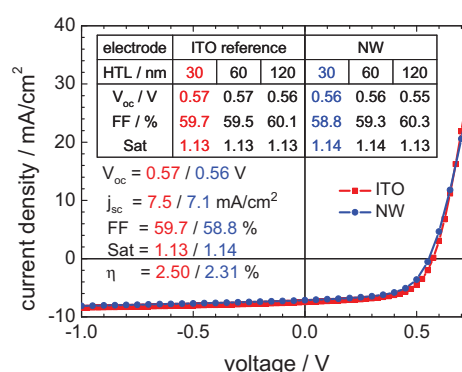


Figure 6.25: *JV*-curves and key parameters of solar cells with 30 nm HTL on ITO or NWs under illumination. The table shows interesting key parameters for cells with the HTL thickness variation.

the reverse leakage current decreases slightly for the NW cells. However, the reverse current of the NW cells is still two orders of magnitude higher, showing that the higher number of possible shunt paths cannot be compensated by the evaporated layer thickness. Thus, the overall performance impact of the evaporated HTL thickness is quite low. This is supported by the fact that even thicker HTL layers (investigated up to 100 nm) deposited directly on a NW-electrode without smoothing reveal only short circuited devices. Given the strong flattening effect of the spin-coated PEDOT:PSS layer, obviously the highly directed vacuum deposition of the HTL layer is much less

effective in planarizing the nanowire induced topography.

The key parameters under illumination are summarized in the inset table of Figure 6.25. The open circuit voltage (V_{oc}), the fill factor (FF) and the saturation value are equal within the error range for all cells. Although the leakage of the NW devices is much higher than in the ITO cells, the equal saturation proves that the effect on the device performance is small. Even for thin HTL layers of 30 nm the leakage is acceptable. The residual parallel resistance in the illuminated device is dominated by internal effects of the solar cell. Furthermore, the series resistances ($3.3 \Omega \text{ cm}^2$ for ITO and $4.7 \Omega \text{ cm}^2$ for AgNW) for both cells are similar and as a consequence the curves differ just slightly in shape demonstrated by the almost equal FF . Only the short circuit current (j_{sc}) for NW-based samples is lower than for the ITO-based references as it is presented for the best cell pair in the jV -curve of Figure 6.25. This can be attributed to the parasitic absorption of the PEDOT:PSS film which has been used for the NW samples only.

As a consequence, for the best NW cell in this experiment an efficiency of around 2.3% could be obtained, roughly 0.2% below the comparable ITO sample. The best values are achieved with just 30 nm HTL proving that the spin-coated planarization layer is sufficient to decrease the shunt paths caused by the unfavorable topography to an acceptable value.

Nevertheless, the leakage currents of the NW devices are still two orders of magnitude higher than for the common ITO as presented in Figure 6.24. Most likely, a certain amount of leakage is still flowing *via* the structure edges. This effect is inevitable as long as the ratio between edge line and area is small^L.

However, because of the roughness of the nanowire film, also current leakage *via* the electrode area is expected. The origin of this area leakage is investigated with organic light emitting diodes in the following. Although just briefly addressed in this thesis, the nanowire electrodes offer also a high potential for the application in OLEDs. Some examinations regarding the implementation in OLEDs can be found in the thesis of Fritz Lehnert which was supervised during this work.^[240] Moreover, in a collaboration with Stanford University, we published a paper dealing with the scattering effect of NW electrodes in bottom-emitting white OLEDs.^[241]

For the investigation of the leakage reasons, a translucent OLED^M with just 50 nm top-contact is either back-illuminated or shining by itself while kept under the surveillance of a microscope. For the observation a long-range $60\times$ objective is used to focus on

^LBecause the layout is fixed up to a certain level, the area is limited to about 30 mm^2 .

^MStack OLED706: electrode/ 240 nm Meo-TPD:NDP2 2 wt%/ 10 nm alpha-NPD/ 20 nm alpha-NPD:Ir(MDQ)2(acac) 10 wt%/ 10 nm BAiq2/ 60 nm Bhen:Cs 1:1/ 50 nm Alu.

the NW network *via* the substrate side. The network is depicted in Figure 6.26.

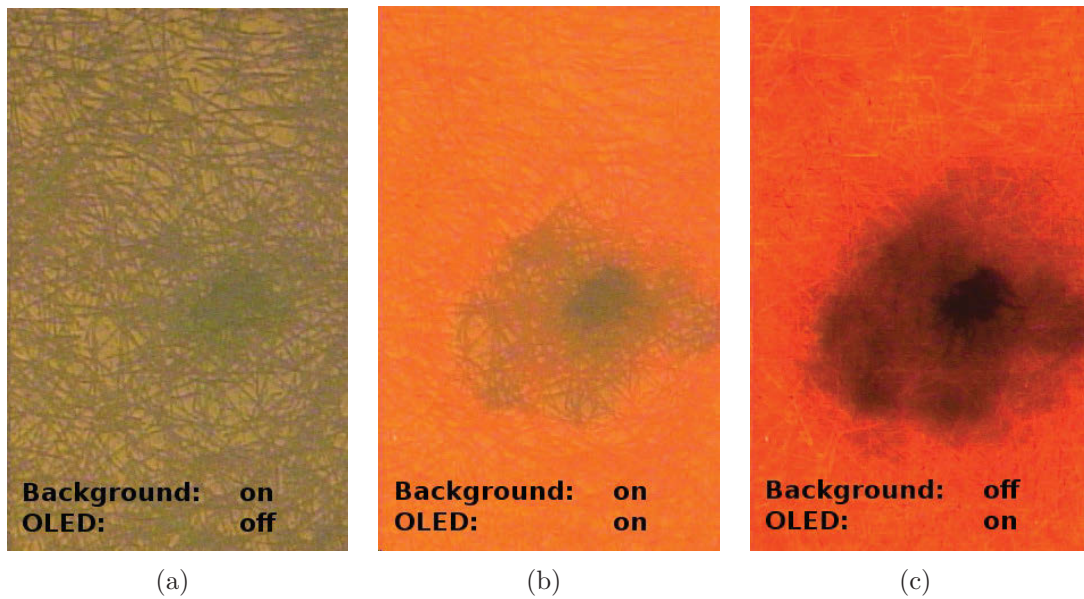


Figure 6.26: Back-illuminated microscope picture of a red bottom-emitting OLED (translucent due to thin 50 nm aluminum top-contact).

The magnification is large enough to make the nanowires visible (see picture (a)). Because of the conductivity of the PH1000 planarization layer and the 240 nm of HTL, the illumination (shown in picture (c), apart from the defect in the center) is quite homogeneous. However, in the middle of the pictures, a large nanowire cluster can be observed (a) while the OLED emission is reduced at this point (b and c). Most likely, this observation is caused by a leakage path through the cluster which leads to a voltage drop in the surrounding and therefore to a decrease of illumination intensity. Thus, large clusters are the main source of leakage, whereas single nanowires and their junctions are less critical.

In general, such clusters are already present in the dispersion^N. In general extensive ultrasonic treatment slightly improves the situation. Nevertheless, the quality of the as-purchased (as-synthesized) dispersion is strongly affecting the film and thus the device performance. The PEDOT:PSS planarization cannot level out these large clusters and therefore the results (mainly the leakage current) were fluctuating from batch-to-batch.

^NThe first investigated Bluenano batch possesses almost no clusters even without ultra-sonic treatment, whereas the 2nd and the 3rd reveal large agglomerates. The 4th shows an acceptable cluster number after ultra-sonic treatment.

6.5 Conclusion

Homogeneous AgNW films are realized both with dip-coating and spray-coating. Besides various process parameters, in particular for dip-coating, the quality of the network depends strongly on the adsorbed water content in the dispersion film. In general, the film characteristics could easily be tuned and both methods are scalable. Subsequently, an annealing step is necessary to improve the network conductivity and therefore achieve a performance which is comparable to commonly used ITO films. Shunts, which are a result of the rough electrode surface, can be avoided with a thin spin-coated PEDOT:PSS cover layer. Since the planarization also absorbs light, the possible thickness is limited, whereas an approach was presented to extend film height at constant transmittance by addition of PVP. In order to structure the composite, various methods are tested and a screen printing is finally used for layout generation. In the last part, small-molecule ZnPc:C₆₀ solar cells are deposited on the electrode revealing an efficiency similar to the ITO reference. The influence of the HTL layer is examined and the points of leakage are discussed.

Chapter 7

Copper as Nanowire Material

In the last chapter, silver was used as nanowire material. Promising results were laid down for this alternative transparent electrode system exhibiting ITO performance. On the downside, silver is an expensive and scarce material itself and therefore, the ultimate production scaling might be limited. Even though just a small amount of about 50–100 mg/m² is necessary for a highly conductive AgNW electrode,^[52] low-cost alternatives are needed. The replacement of silver by copper offers several superior key parameters, such as price (ca. 100 times cheaper) and availability (ca. 1000 times higher abundance^[242]). Very recently Rathmell *et al.* reported on the potential of copper nanowire (CuNW) networks as transparent contact layer.^[102,207]

In the following chapter the work on this alternative electrode material is presented. At the beginning, some comments about synthesis and deposition of the nanowires are provided. In the second section, the improvement of the wire-contact is addressed and two different post-processing steps are investigated. The last section deals with cell integration and is finalized by a brief discussion of the degradation.

The major results of this chapter have been accepted for publication in *Advanced Energy Materials*.^[243]

7.1 Synthesis and Deposition

7.1.1 Synthesis Approaches

In contrast to silver as nanowire material, copper nanowires have not been commercially available in the last years. In addition, copper is a sensitive material which is prone to oxidize. Therefore, much more effort has to be invested in the nanowire synthesis and modification.

The nanowires are synthesized by Dr. Nelli Weiß from the Physikalische Chemie at the

TU Dresden. This offers the opportunity to test various synthesis routes and produce dispersions with differing nanowire diameters or deposition solvents. Moreover, the knowledge of the exact synthesis route enables a deeper insight in the nanowire structure (*e.g.* surfactant shell) compared to commercial products^A.

As starting point the synthesis of Mohl *et al.* is chosen, since these nanowires should provide a large aspect ratio.^[154] In addition, for comparison also NWs based on the publications of Rathmell and Wiley are synthesized.^[102,207] These two synthesis approaches, which are investigated in more detail, are introduced in the next section. Nevertheless, in the last years various other synthesis routes have been published and some have also been tested by our group, as itemized in the following overview.

- Liu *et al.* published first capping growth of CuNWs with an approach similar to Mohl,^[154] but utilizing dodecylbenzenesulfonate as capping surfactant.^[155] Because of the similarity compared to Mohl and a lack of information about the dimensions, this recipe was not tested.
- Jin *et al.* more or less reproduced the results of Mohl.^[245]
- Zhang *et al.*^[246] presented a water-free synthesis which, however, did not work out properly in our tests.
- Ye *et al.* demonstrated a synthesis in organic solvent at 200 °C,^[156] which was not tested.
- Zhao *et al.* showed an approach similar to Rathmell's recipe.^[247]
- Shi *et al.* published an approach similar to Mohl, but with octadecylamine as capping agent and without reducing agent.^[248,249] In our tests the products appear to be unstable and, moreover, the mechanism remains unclear.

7.1.2 Mohl-Synthesis

The synthesis approach by Mohl *et al.* is based on a reduction of copper salt with glucose in an autoclave, which is way less poisonous than the commonly used reducing agent hydrazine (*e.g.* see next Section 7.1.3).

At the beginning, nanowires are synthesized exactly as presented in Mohl *et al.*^[154] The copper salt CuCl_2 is solved in water. Subsequently 0.39 g glucose as reducing agent and hexadecylamine (HDA) as capping are added. The resulting nanowires possess

^ASince recently also copper nanowires can be purchased, for instance from NanoForge Corp.^[244]

an average diameter of 44.6 nm calculated from 200 arbitrarily chosen nanowires on transmission electron microscopy (TEM) images (see Figure 7.1). This nanowire type

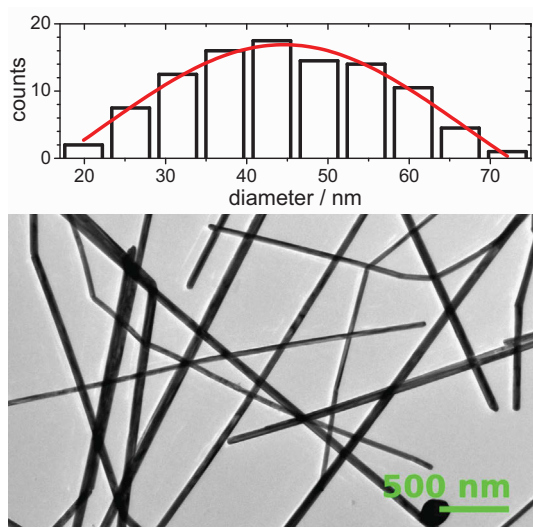


Figure 7.1: TEM image of CuNWs prepared with 0.39 g glucose drop-coated onto a TEM-grid and the corresponding diameter distribution at the top.

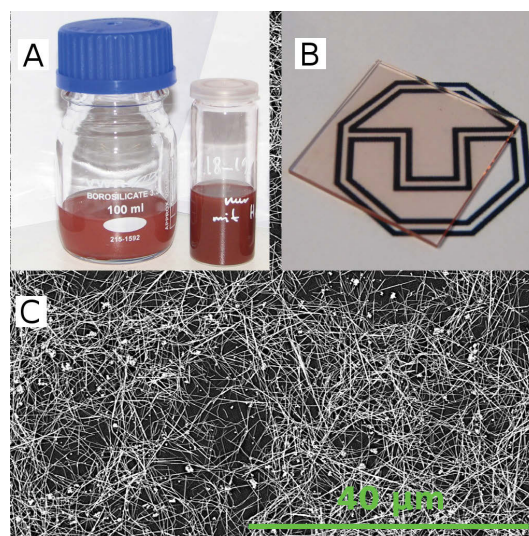


Figure 7.2: Copper nanowire dispersion ready for coating (A) and a spray-coated glass substrate (B) with the corresponding SEM image of the film (C).

is used throughout the rest of this chapter^B, unless otherwise noted. The detailed synthesis of the used nanowires can be found in the experimental Section 5.1.

The XRD data of the as-prepared nanowires can be found in Figure 7.3 showing a high crystallinity. As stressed by Jin *et al.*, in this synthesis a pentagonal nanowire is grown

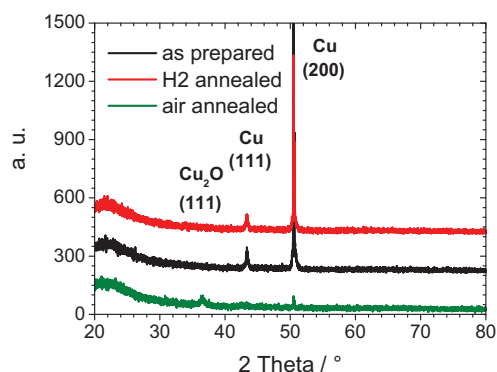


Figure 7.3: Reflection XRD data of CuNW films on glass as prepared directly after solvent exchange (a), after heating at 175 °C in H₂ (b) and annealed in air (c).

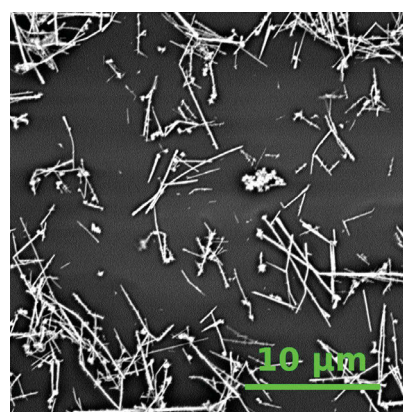


Figure 7.4: 30 × 30 μm² SEM figure of spray-coated nanowires synthesized following Rathmell and Wiley including PVP treatment.^[207]

^BThis nanowire type shows the best performance and stability achieved for copper in this work as stressed in Section 7.2.3.

with 5 [1,1,1] planes at each ending and 5 [1,0,0] faces along the length axis.^[245]

If the amount of glucose in the synthesis is doubled to 0.78 g, thinner nanowires with an average diameter of 33 nm are obtained. Lowering the temperature of the autoclave from 120°C to 100°C causes a diameter reduction to 24 nm for the 0.39 g glucose approach, which is consistent with results published by Jin *et al.*^[245]

All nanowire dispersions synthesized by this method show a similar length distribution, which is very broad containing wires from five to some tens and even hundreds of micrometers. In addition, a small amount of nanoparticles of varying shape is present in all dispersions as by-product of the synthesis.

After the synthesis, the NWs are washed with water and n-hexane to remove the excess of non reacted species, since they might deteriorate the wire-wire contact in the network films. Subsequently, the solvent is exchanged and the nanowires form low concentrated dispersions in isopropanol without larger aggregates.

Using these nanowire dispersions, homogeneous nanowire films could be spray- and dip-coated on glass (*e.g.* see Figure 7.2) and polymer substrates. In contrast to results presented by Rathmell *et al.*,^[102] no additional surfactants or film-coating matrix materials are necessary to prepare uniform copper NW films.

7.1.3 Wiley-Synthesis

The synthesis of Rathmell and Wiley^[207] uses hydrazine as reducing agent, as first mentioned by Chang *et al.*^[157] Moreover, ethylenediamine as capping agent and $\text{Cu}(\text{NO}_3)_2$ as copper source are added to an $\text{Na}(\text{OH})$ -water solution. The films produced in the original paper by a filtering and transfer process were immediately conductive without post-treatment.^[207]

As comparison we sought to reproduce this approach although the aspect ratio is rather moderate. Two batches are synthesized exactly as presented in the paper. It is noteworthy that in the 2nd batch the PVP washing step is left out. A detailed description can be found in the experimental Section 5.1. The deposition is done as described for the Mohl-nanowires, from isopropanol dispersions by spray and dip-coating.

Unfortunately, in contrast to the literature,^[207] the wires are not conductive after deposition. Moreover, the deposition of the wires is complicated. They tend to agglomerate even in highly diluted dispersions and result in clumpy films (see Figure 7.4). The addition of PVP, as mentioned in the literature,^[207] could not improve the situation. As a consequence, for further experiments the synthesis procedure by Mohl *et al.* is used.

7.2 Contact Issues, Post-Processing and Resulting Performance

7.2.1 Pressing

After film deposition, the network is not conductive because of the high junction resistance between adjacent wires in the network. Similar observations are reported for AgNW networks in Chapter 6. In accordance with literature, the surfactant is identified as potential reason.^[96] In case of the used CuNWs the presence of HDA molecules results in a gap between neighboring nanowires of less than twice the length of HDA, which was reported to be 2.26 nm.^[250] The PVP shell at the surface of AgNWs produced by the most common synthesis route is assumed to result in a similar distance between adjacent wires.^[96] However, the typical annealing in air cannot be used for enhancement of the contact since it would lead to an immediate oxidation of copper. Therefore, a mechanical pressing step similar to the technique successfully applied by Gaynor *et al.* for AgNWs is applied to enhance the contacts and enable a better network conductivity.^[70]

The CuNW networks for this experiment are spray-coated on a polyethylene terephthalate (PET) foil and pressed together with a cover glass to avoid damage. As evidenced from the SEM image in Figure 7.5, after pressing the wires remain on the plastic foil due to the presence of strong adhesion forces. Thus, the method is sufficient to achieve

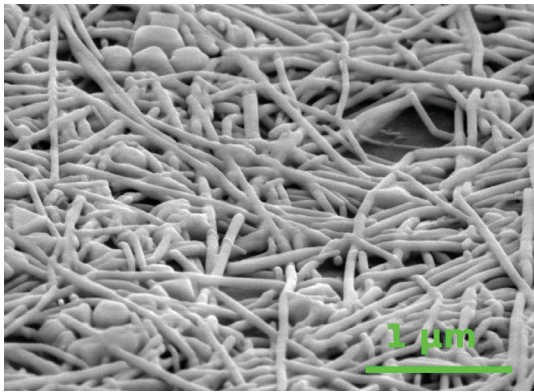


Figure 7.5: Tilted SEM image (angle of 60°) of a dense, spray-coated CuNW film after being pressed for 30 s at 3.9 GPa at room temperature.

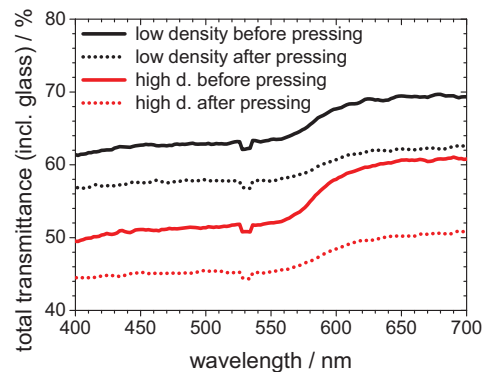


Figure 7.6: Total transmittance spectra of NW films before and after pressing with 1.96 GPa. The pressed networks reveal a sheet resistance of 50 Ω /sq. (black) and 8.6 Ω /sq. (red).

a well-connected network on the plastic foil without any delamination.

Pressures up to 4 GPa are applied, which affect both the conductivity and the transmittance. In our examinations, the minimal pressure at which a conductivity could

be achieved is 0.4 GPa. At equal nanowire densities higher pressures cause better conductivities. Unfortunately, the total optical transmittance is decreased by the pressing process (see Figure 7.6) and the value drops even stronger at higher pressures (see Figure 7.7). This high transmittance loss counteracts the improvement and spoils the

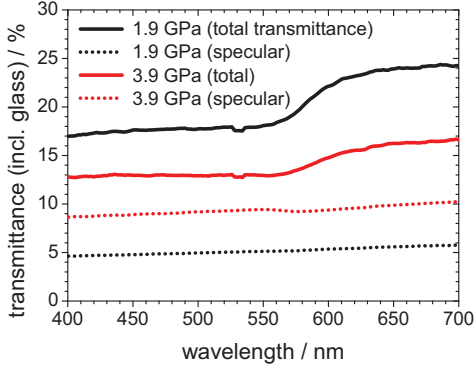


Figure 7.7: Transmittance spectra (specular and total) of dense nanowire films (same density) after pressing at differing pressure. The corresponding R_{sh} is $1.5 \Omega/\text{sq.}$ (black) and $1.0 \Omega/\text{sq.}$ (red)

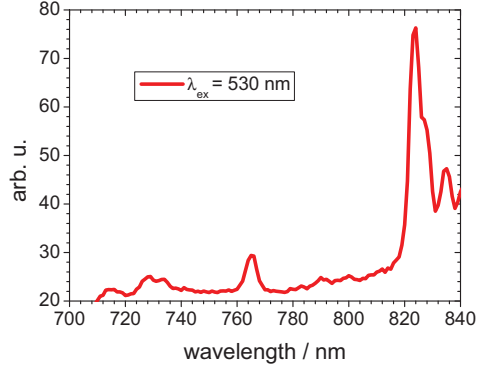


Figure 7.8: Emission spectrum of a CuNW film excited at 530 nm. The peak at 820 nm corresponds to the fluorescence of copper(I) oxide.

performance of the electrode. Although the networks are conductive after pressing, the performance values of $50 \Omega/\text{sq.}$ at about 65% transmittance (see examples in Figure 7.6) are far below the values achieved for silver nanowires (see Figure 6.14) and thus, are not sufficient for a competitive transparent electrode.

7.2.2 Annealing

Since the conductivity values for silver and copper are nearly equal, a better performance is expected for the long and crystalline copper wires. Therefore, the conductivity and especially the inter-wire contact has to be improved further. We suppose that a copper oxide layer might be responsible for the poor contact between the wires.^[154,245,246] Although the XRD study does not show any copper oxide related reflexes (see Figure 7.3), it is noteworthy that amorphous or thin nano-crystalline oxide layers are difficult to detect with XRD. An indication for a slightly oxidized Cu surface can be observed in fluorescence measurements^C for CuNW films on glass. The emission spectrum (excitation wavelength of 530 nm) presented in Figure 7.8 shows a clear peak around 820 nm which is attributed to oxygen vacancies in the copper(I) oxide lattice.^[251]

^CAlthough a fully study is not executed in this thesis, the method might offer an easy way to track the oxidation behavior.

In literature, the oxidation on copper nanoparticles utilized for ink-jet printing was intensively studied.^[252,253] The formation of an oxide layer in air was also reported for CuNWs^[102,154–156,254,255] and investigated for thin copper films.^[256]

Since the copper oxide layer is assumed to be the major limit for the conductivity, a reduction approach is used to convert the oxide into elementary Cu. In the reduction process the samples are heated to 175 °C under hydrogen flow.

Subsequently, the films show a strong decrease in sheet resistance to values as low as 24 Ω/sq. at 82% total transmittance (corresponds to about 88% when subtracting the substrate). The temperature applied during this treatment is much lower than that in other reduction experiments reported in the literature, *e.g.* 300 °C^[98,246] and 400 °C,^[257] but is sufficient to improve conductivity significantly. In the original paper by Mohl *et al.* also higher temperatures were required to achieve high conductive behavior.^[154] Recent publications, which apply nanowires from the Wiley group (NanoForge Corp.^[244]), also mention low temperatures of 180 °C. However, in Rathmell *et al.*^[102] the step is only utilized to remove the coating matrix and Kholmanov *et al.*^[258] do not further discuss the annealing.

The required temperature is crucial for the application of polymer foils. Although 175 °C is still a quite high temperature, and there is certainly room for improvement towards more gentle post-processing, we are able to achieve sufficient electrodes on temperature stabilized PET. The whole transmittance-resistance data for reduced CuNW electrodes of various coverages on glass substrates is displayed in Figure 7.9. For comparison the data of our standard ITO electrode on the same glass substrate

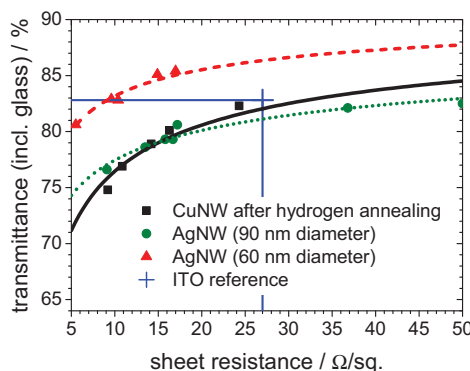


Figure 7.9: Performance graph of transparent NW electrodes obtained with our copper wires (black squares). For comparison results for silver wires with a diameter of 60 nm (red triangles) and 90 nm (green circles) are shown, taken from Chapter 6. The complete data sets are fitted with a FoM model presented by De *et al.*^[125] For comparison our standard ITO is marked with a blue cross.

and results obtained for AgNW electrodes (see Section 6.3) are added. All of them reveal a more or less similar performance. In order to compare the results to the literature, the figure of merit for conductive percolation networks is used as well. The calculated value for Π of around 60 is among the best values published for transparent conductive networks and hence offers a suitable electrode performance. To the best of our knowledge, this is the best CuNW performance published so far and illustrates the advantage gained from the very long nanowires achieved by the Mohl-synthesis.^[102,247,258,259]

Additional annealing experiments using nitrogen and a 10% hydrogen-nitrogen gas mixture do not result in any detectable decrease of the sheet resistance. This observation proves that the application of heat alone is not sufficient and a highly reducing environment is necessary to attain conductivity levels relevant for application. In addition, our hypothesis is further backed by the fact that the increase in conductivity is indeed caused by the reduction of oxide and not by the thermal desorption or rearrangement of the ligand shell.

Furthermore, hydrogen annealing has also an effect on the transmittance spectrum. As shown in Figure 7.10, annealing in the presence of hydrogen causes a transmittance increase in the short wavelength regime. An explanation about the exact origin of this

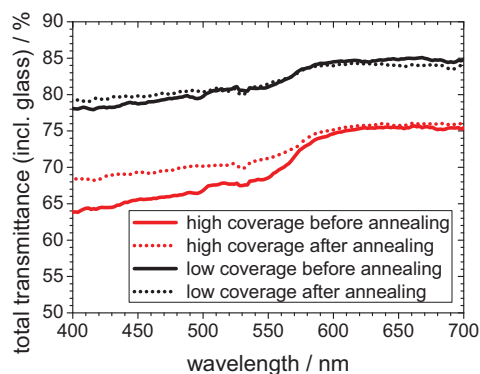


Figure 7.10: Transmittance graph of CuNW films (black: $24.3 \Omega/\text{sq.}$; red: $9.2 \Omega/\text{sq.}$) before (solid line) and directly after (dotted) hydrogen annealing.

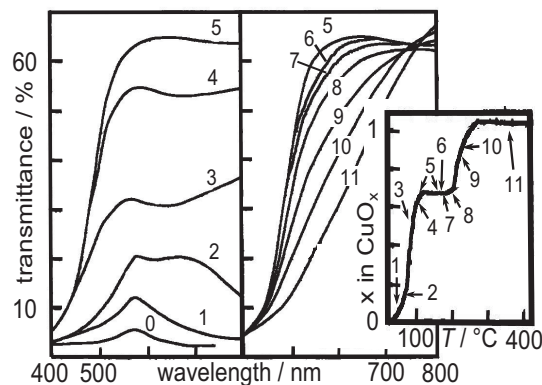


Figure 7.11: Transmittance spectrum of a 50 nm copper film during oxidation (1 \rightarrow 11) reproduced from Wieder and Czanderna.^[256]

effect probably needs complex calculations involving the scattering of the nanowires. Along with the nanowire material also the substrate, the wire dimensions and the shell environment affect the result. Nevertheless, from our observations, we can deduce that the transmittance change is caused by the expected reduction of copper(I) oxide (Cu_2O) to elementary copper. The Cu_2O in the oxide shell has a band gap of about 2.0 eV

and starts absorbing in the region < 500 nm (see Figure 7.11).^[256] A thinner shell of Cu_2O leads to higher transmittance in this short wavelength regime, but no changes occur in the red spectral region, where Cu_2O is transparent anyway. The correlation of this effect to Cu(I) oxide is also supported by its reversibility. After storing samples in air for several days, the transmittance spectra exhibit the same shape as prior to annealing.

Although the transmittance spectra return to the less transparent pre-reduction appearance after some days, conductivity remains high (around 20% increase in 100 days, as visible in the degradation graph depicted in Figure 7.12(a)). Most likely, the copper

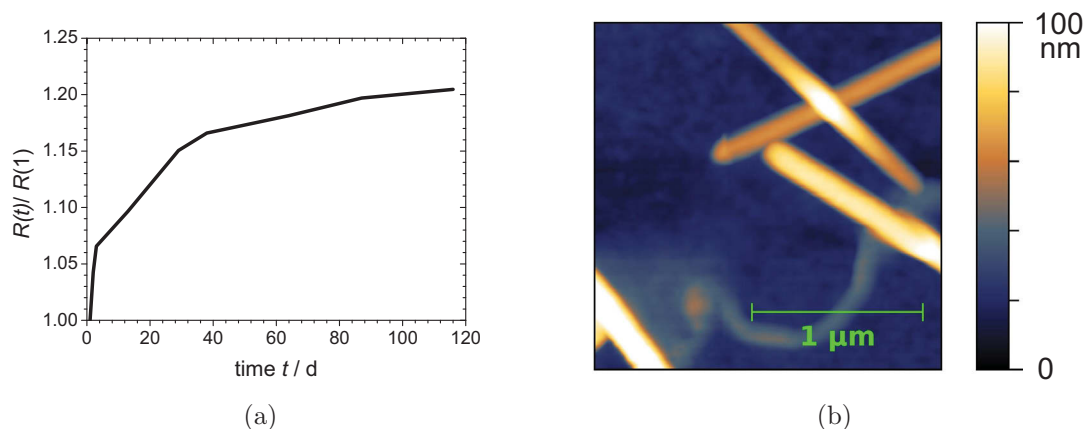


Figure 7.12: a: Resistance between two conductive silver points on a CuNW thin-film, measured for about 4 months to verify stability under ambient conditions. b: AFM image of a NW junction showing a bent AgNW. The nanowires are spray-coated on a V-PAI4083 PEDOT:PSS interlayer.

wires re-oxidize with time, whereas the contact areas at the junctions are protected between the wires and therefore are more resistant to oxidation. Since the nanowires can be quite flexible (as described in literature^[260] and observed in our experiments as visible in Figure 7.12(b)), such enlarged and therefore protected contacts are likely. The observed stability is consistent with results presented in the literature^[102] and should be sufficient for the application in encapsulated organic devices.

7.2.3 Post-Processing with Various Nanowire Diameters

As mentioned in the beginning of Section 7.1.2, the results presented in the paragraphs above are all measured for 45 nm Mohl nanowires.

As several studies pronounce the advantage of thinner nanowires for better performance,^[125,245] in this work nanowires with smaller diameters down to 24 nm are synthesized and tested. In the following, some remarks are given regarding these

experiments.

The thinner wires are deposited also by spray-coating just as the thicker wires. However, films made from nanowires with diameters below 30 nm are not conductive even after reduction with hydrogen at 175 °C. Conductivity results obtained for films with nanowires between 30 and 40 nm appear to be not reproducible. Furthermore, these nanowires show a faster degradation under ambient conditions compared to the results in Figure 7.12.

This lower conductivity and stability of the thinner wires can be explained with strong oxidation behavior. As mentioned in the last section, the contact area between the wires after reduction seems to be protected against oxidation by the wires itself. Consequently, a smaller wire radius should decrease this protection effect. Thus, the junctions re-oxidize quickly upon exposure to oxygen. Furthermore, the oxide shell of the Cu nanowires causes an effective thinning of the metal core. Therefore, at smaller diameters the conductive volume is relatively more affected by the oxide shell. Additionally, the core-diameter decreases below the range of the electron mean free path, which is about 40 nm for elementary copper. As demonstrated in Section 4.2.2, for small conductive cores (< 15 nm) and assumed diffuse surface electron scattering, a resistivity increase is expected.

Although thinner nanowires at equal length are claimed to be preferable,^[125,161] for our experimental conditions, wires with a diameter of 45 nm worked better than thinner wires. They enabled a reasonably high performance at sufficient stability, whereas thinner wires exhibit unstable results. Similar observations about a lower thickness performance limit were recently concluded by Zhao *et al.* They observed an accelerated increase in sheet resistance for nanowire diameters below 110 nm.^[247]

However, when the oxidation is suppressed by a complete processing in nitrogen atmosphere, thinner conducting nanowires and therefore a superior network performance might be possible. Nevertheless, in this case the electrode would be much more sensitive to oxygen and an appropriate encapsulation would be required.

7.3 Solar Cell Integration

7.3.1 PEDOT:PSS Application

After achieving a sufficient electrode performance and stability particularly for the thicker wire batch, the network is tested for organic solar cell applications.

At the beginning, the inherently rough surface of the nanowire film requires a planarization layer to avoid shunts in the shallow organic stack, as already shown in

Chapter 6 for silver.

Therefore, a PEDOT:PSS film is spin-coated to planarize the structure. Unfortunately, PEDOT:PSS is a hygroscopic and acidic material and thus, causes a critical environment for an ignoble metal like copper. Moreover, the processing of the PEDOT planarization layer requires temperatures above 100°C. At these elevated temperatures, the oxidation of copper is already accelerated when exposed to oxygen atmosphere, as can be seen in Figure 7.11. Since spin-coating in nitrogen is not possible in our lab, short tests are performed to examine the influence of the PEDOT heat-out step.

Annealing under ambient conditions at 120°C (relevant temperature for solution-processed PEDOT:PSS) causes a steep resistance increase (values about 20% per minute are measured), which rules out annealing in air.

Instead, a nitrogen atmosphere is desirable. Figure 7.13 shows the increasing resistance between two points (resistance is measured twice [1st and 2nd] per sample to examine the reliability) of the network while being annealed at 120°C in nitrogen atmosphere. After 10 min (realistic annealing time) an increase of 5 to 15% is measured, whereas an

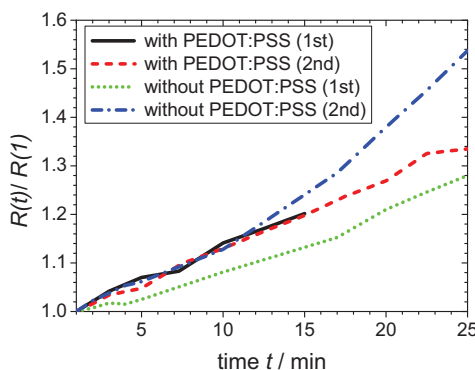


Figure 7.13: Two-wire resistance R of the network between two conductive silver points while being annealed at 120°C. The resistance is normalized to the value after one minute $R(1)$. R is measured twice [1st and 2nd] per sample to examine the reliability.

influence of the PEDOT:PSS layer^D could not be observed. Although oxygen is absent the degradation cannot be avoided completely — maybe caused by structural changes or remaining oxygen molecules. However, it is reduced by a factor of 10 compared to air.

As a consequence, after spin-coating of a circa 40 nm PEDOT:PSS PH1000 layer (as for the silver results) a stepwise baking step is chosen. At the beginning a short 20 s bake out is taking place in air to evaporate the majority of the solvent (water).

^DThe PEDOT:PSS formulation Clevios V-PAI 4083 from Heraeus is applied. Due to its low conductivity in the range of 10^{-3} S/cm,^[261] the influence on the conductivity compared to the copper grid is negligible

Subsequently, the film is annealed for 5 min in nitrogen. The temperature for both steps is 120 °C.

The procedure keeps the degradation small and just about 10% conductivity drop are observed during the annealing. Moreover, the sheet resistance of the PEDOT-NW composite remains almost constant compared to the original network performance, because the highly conductive PEDOT:PSS Clevious PH1000 contributes to the conductivity as already mentioned in Section 6.4.3.

The structuring of the electrode is done with the 1064 nm laser-scribing system. The screen-printing would require an additional annealing step to bake out the paste which is a source of degradation. In order to minimize the effect of edge-leakage, the pixel area is increased to 16 mm² as it is presented in Section 6.4.2. Thus, the area-to-edge ratio is improved and the edge effect is less pronounced.

7.3.2 F₄ZnPc:C₆₀ Solar Cell Deposition

After the application of the planarization layer a F₄ZnPc:C₆₀ bulk heterojunction cell^E is deposited on top of the polymer-coated CuNW network. The jV-curve and the data of the corresponding ITO-based reference cell are shown in Figure 7.14. Except of the

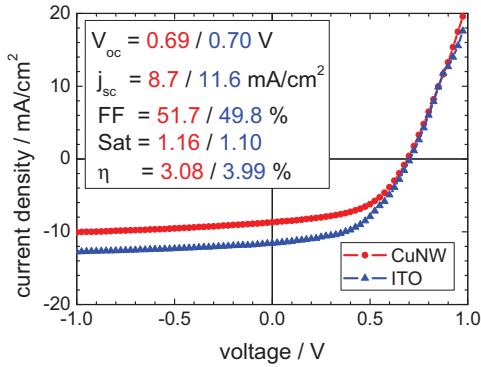


Figure 7.14: JV-curves and key parameters of solar cells on ITO and CuNW electrode illuminated by a sun-simulator at 1 sun. The values are the best out of two pixels with an area of 16 mm² (CuNW) and 12.8 mm² (ITO), respectively.

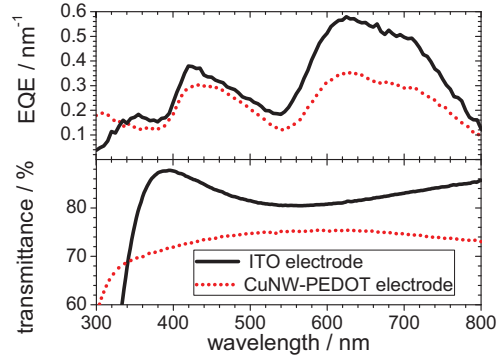


Figure 7.15: Top: External quantum efficiency of the two cells shown in Figure 7.14. Bottom: The corresponding specular transmittance spectra of the electrode systems used.

low short circuit current density, the key parameters are similar compared to the values of the reference cell. The saturation demonstrates that the leakage is at an acceptable

^EStack OSOL829: electrode/ 1 nm NDP9/ 50 nm BF-DPB:NDP9 10 wt%/ 5 nm F₄ZnPc/ 55 nm F₄ZnPc:C₆₀ 1:1 (100 °C)/ 30 nm C₆₀/ 6 nm BPhen/ 100 nm Alu.

level even for such thin (≈ 100 nm organic) small-molecule stacks. Thus, the planarization by the polymer layer is sufficient. Moreover, as explained in Section 6.4.3, the amount of agglomerates in the film is small enough and the quality of the dispersion is appropriate.

Since the electrical properties of the stack are sufficient (no shunts), the open circuit voltages are similar as well. The calculated series resistance seems to be dominated by the organic stack because both cells have identical values of $54\ \Omega\ \text{cm}^2$ (ITO) and $53\ \Omega\ \text{cm}^2$ (CuNW), respectively. Therefore, the fill factor (FF) for both cells is equal. For the short circuit current (j_{sc}) a large deviation of about 30% is observed. In Figure 7.15 the corresponding external quantum efficiency (EQE) graphs and the transmittance of the electrodes are plotted to elucidate the high losses. Unfortunately, the transmittance spectrum cannot explain the deviations. Between 300 nm and 550 nm the EQE matches to the transmittance curve. In contrast, above 550 nm at the $F_4\text{ZnPc}$ related absorption this correlation cannot be drawn any more. In this region, the EQE of the copper sample is about 50% lower than for the ITO-based cell, although the transmittance difference is just in the range of 15% to 20%. The drop might either be related to optical effects or most likely, the effect is a result of the substrate temperature during deposition. The samples are heated optically from the back-side and differences in absorption and reflection (ITO *vs.* metal network) might result in temperature differences. These deviations would affect layer morphology and therefore, change the solar cell properties.

Although several challenges were faced, an organic solar cell could be successfully deposited on top of a CuNW electrode. Along with the drop of j_{sc} all other important key parameters are equal to the reference. The efficiency of the nanowire device is 3.1% compared to 4.0% for the ITO reference.

7.3.3 Degradation

Although the presented $F_4\text{ZnPc}$ cell shows reasonable stability (measured over one month, stored without illumination) some solar cell runs (*e.g.* $\text{ZnPc}:\text{C}_{60}$ in OSOL893) failed completely. These solar cells revealed a large series resistance although the resistance of the electrodes exhibit still low values. Therefore, the charge carrier extraction from the solar cell seems to be hindered. As already mentioned, the counterion PSS is an acidic and hygroscopic material. Hence it might corrode the ignoble metal nanowires.

As the reproducibility is obviously affected, a brief examination is carried out to identify the steps in the process chain which are critical for the stability. For that purpose, $\text{ZnPc}:\text{C}_{60}$ solar cells with differences in the electrode processing are produced

at the UFO-chamber. Based on the assumption of ‘protected’ nanowire junctions (see Section 7.2.2) the storage time after hydrogen treatment and PH1000 application is varied. The applied p-i-n solar cell is similar to the one presented in Section 6.4.3 here with 50 nm HTL.

In the first part, the storage time in air is examined. At warm weather conditions (inside the building: 29°C, 50% $_{RH}$) the samples are freshly deposited, annealed, planarized and handled quickly until transfer into the evaporation chamber (with an additional heat-out step in nitrogen before vacuum transfer). The time of air exposure before PEDOT:PSS coating is varied between sample #1 (1/2 h) and sample #2 (2 1/2 h). As depicted in Figure 7.16 both solar cells show a similar performance which remains stable (checked for 12 days). Therefore, as long as the time of air exposure is

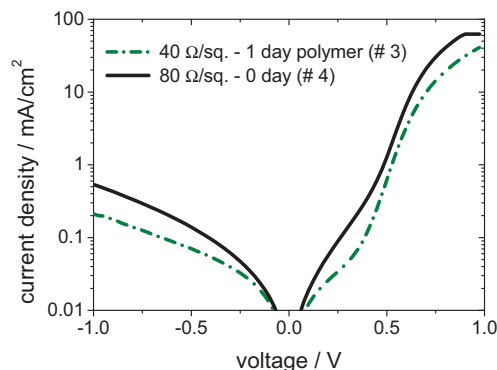
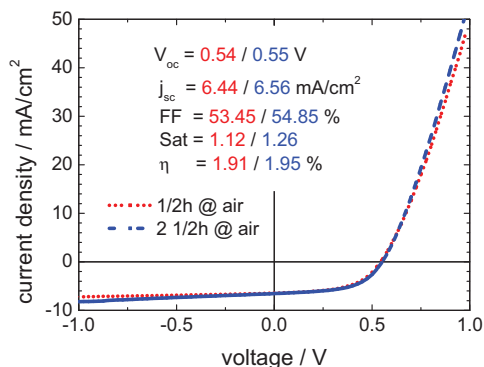


Figure 7.16: jV-curve of sample #1 and #2 under illumination with the corresponding key parameters. **Figure 7.17:** Semi-logarithmic jV-plot of sample #3 and #4 without illumination.

moderate, the cells stay unaffected and no barriers are formed.

The remaining samples (#3 and #4) are stored in nitrogen after the hydrogen annealing. After storing for one week, they are used in order to determine the influence of absorbed water in the PEDOT:PSS layer on the cell efficiency. After PH1000 is coated on sample #3 ($R_{sh} = 40 \Omega/\text{sq.}$ incl. PH1000), the sample is stored (without glovebox heat-out) in nitrogen for one additional day. In contrast sample #4 is coated with PH1000 directly before solar cell deposition ($R_{sh} = 80 \Omega/\text{sq.}$ incl. PH1000). The corresponding dark jV-curves in Figure 7.17 show a different behavior. The solar cell #3 with half the sheet resistance of sample #4 reveals a much higher series resistance (current density at high voltages is decreased), which indicates conductivity problems. However, a corresponding drop of the electrode resistance is not observed^F. Therefore, the problem seems to be related to the contact between copper and polymer layer.

^FIn order to explain the decrease, a strong resistance increase (at least factor 2–3) within one day is required.

Obviously, the generation of copper oxide (with undefined and badly conductive semiconductor structure) produces a barrier for the charge carriers. Moreover, a further degradation can be observed. After 4 days sample #3 demonstrates a strong s-kink, which is a hint for extraction/ injection barriers.^[37]

Since the oxidation just weakly affect the sheet resistance and rather the CuNW interface, the assumption of protected contact areas could be confirmed. It is noteworthy that metal interfaces (*e.g.* top or bottom electrode), in particular for reactive metals, are often a point of cell degradation.^[262]

As a consequence, two crucial points can be emphasized. First, the water content in the PEDOT:PSS seems to be the main driving force for cell degradation, due to contact degeneration at the polymer-copper interface. Therefore, when producing and storing these copper composite electrodes, appropriate heat-out steps and a water-free environment are necessary.

Second, although the contact between polymer and copper degrades, the sheet resistance of the composite still remains low. The contact at the nanowire junctions exhibit a different degradation behavior compared to the polymer-copper interface. Nevertheless, both contacts are important to enable a sufficient current transport in the solar cell. Hence, for the evaluation of the electrode stability among the sheet resistance, also the degradation of the nanowire surface has to be considered. Thus, a graph as presented in Figure 7.12 is not adequate for reviewing the electrode stability as commonly done in research publications.^[102,258,259] Additionally, the surface degradation has to be investigated.

7.4 Conclusion

Compared to silver, which was addressed as nanowire material in the previous chapter, the more abundant material copper is applied.

A hydrazine-free, hydrothermal synthesis method is used for growing ultra-high aspect ratio copper nanowires. As for silver, the nanowires are dispersed in alcohols and homogeneous films could be prepared on glass and PET foils without any matrix material by utilizing a spray-coater. After deposition, the film is not conductive and therefore a pressing step is investigated to improve the contact between the wires. Since the resistance remained high after pressure application, further examinations identified a copper oxide shell as reason for the low electrical conductivity. Thus, a reduction in hydrogen atmosphere at elevated temperatures is performed resulting in a significantly improved network performance ($24 \Omega/\text{sq.}$ at 88% transmittance) comparable to the sil-

ver NW results in Chapter 6. Finally, with the help of a planarizing PEDOT:PSS layer, the electrode is integrated into a $F_4ZnPc:C_{60}$ bulk heterojunction small-molecule organic solar cell, which shows perfect electrical behavior and revealed 3.1% efficiency compared to 4.0% with an ITO reference device. Additionally, a brief degradation study with $ZnPc:C_{60}$ cells is presented. The experiments illustrate that the sheet resistance is just a minor point of degradation and the copper-polymer interface is way more prone to cause conductivity problems.

Chapter 8

Anisotropic Nanowire Networks

In Chapter 6 and 7, random or at least semi-random networks are investigated. However, without special handling the dip-coated networks exhibit a rather anisotropic structure, as indicated briefly in Section 6.1.1. The Anisotropy strongly affects the properties of the nanowire network. Various effects occur, both interesting for the application and from a fundamental point of view.

Therefore, the properties of anisotropic silver nanowire networks are discussed in the following chapter. In the first section, facts concerning the preparation of such networks are presented. Moreover, the optical consequences are addressed, whereas the spectrum can be used to evaluate the alignment. Subsequently, the second section focuses on the influence on the electrical properties dealing with the percolation and the resulting conductivity behavior. Furthermore, a simulation approach is discussed and a possible application in solar cell modules is outlined.

8.1 Dip-Coating and Anisotropy

8.1.1 Network Generation and Anisotropy

When a substrate is dipped into a nanowire alcohol dispersion, after pull-out and solvent evaporation a more or less aligned nanowire film is deposited as depicted in Figure 8.1. For an extended substrate with infinite width, the alignment direction is always parallel to the dipping-process as depicted in the middle of the figure. Deviations occur towards the left and right edge of the substrate (see Figure 8.1 left and right picture). The closer the edge, the more the NW orientation changes, while the wires are still parallel to each other. In these regions the alignment is dominated by the edge and the NWs are aligned increasingly perpendicular to it.

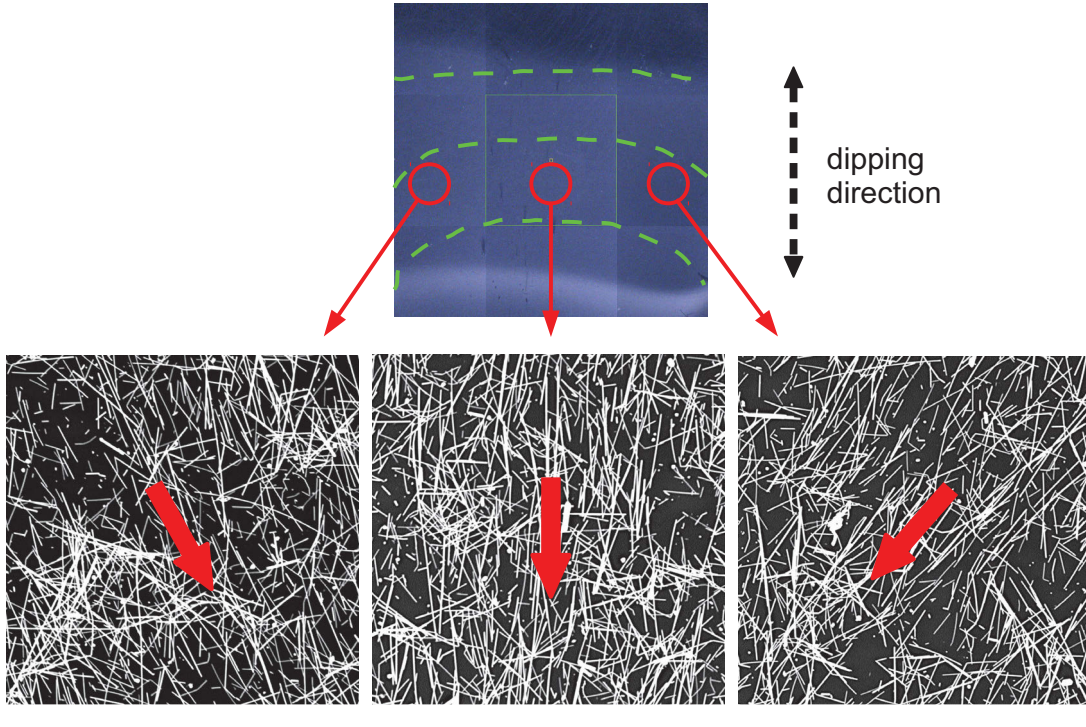


Figure 8.1: Photographic image of a dip-coated silver nanowire film on glass, whereas the dipping direction is marked. The SEM graphs demonstrate the network alignment at different positions of the film. The alignment directions are emphasized with an arrow.

During the evaporation process the contact line^A is moving towards the bottom of the dipped sample. The shape of the line is illustrated in Figure 8.1 (top) for three arbitrary points in time during evaporation^B. For the experimental parameters chosen here, the line is moving fast (the process takes about 3 s). Evidently, the contact line shape matches well to the nanowire alignment, whereas the nanowires are oriented perpendicular in relation to the contact line.

Under suitable parameters (low dispersion clusters and low air humidity) highly oriented nanowire films are generated as shown in Figure 8.2(a). Compared to a random or semi-random network, these films exhibit an anisotropic light transmittance behavior. As shown in Figure 8.2(b) different curves are observed for light polarized parallel (TM) and perpendicular to the NW orientation (TE). This characteristic can be used as measure for the degree of alignment. The larger the split between the two curves, the higher the alignment quality.

In order to obtain some information on the network generation, two additional experiments are performed regarding the alignment quality. Figure 8.3 shows the

^AThe contact line is defined following the literature and describes the border of the liquid film on the substrate.^[218]

^BAn example for such a deposition process can be found in Lu *et al.*^[263] In this publication the movement of a contact line is illustrated and a picture of the typical interference patterns is shown.

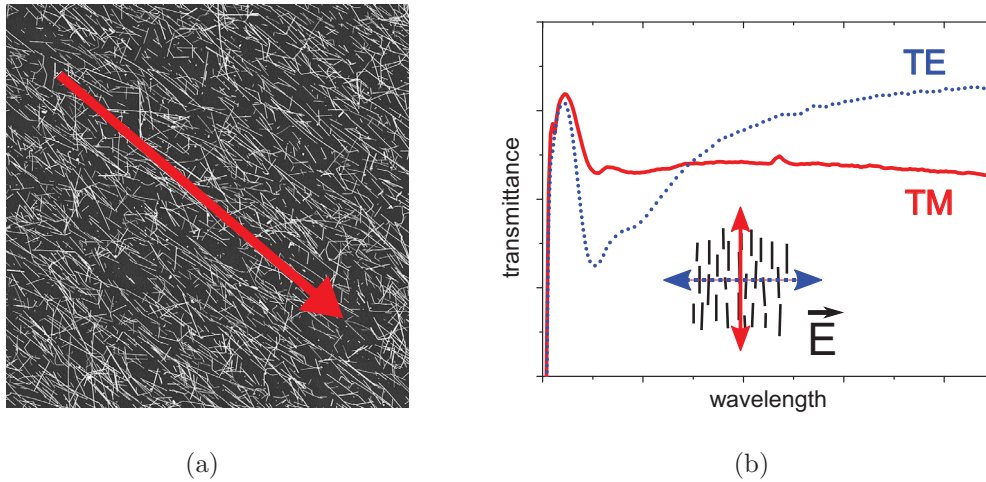


Figure 8.2: a) $80 \times 80 \mu\text{m}$ SEM graph of an anisotropic silver nanowire network (NW121) with an arrow pointing towards the dipping (alignment) direction. b) The corresponding specular transmittance spectra for parallel (TM — solid red) and perpendicular polarization (TE — dotted blue) are depicted

polarization-dependent transmittance spectra for the air humidity experiments presented in the previous Section 6.1.2. At low water contents, the split between TM

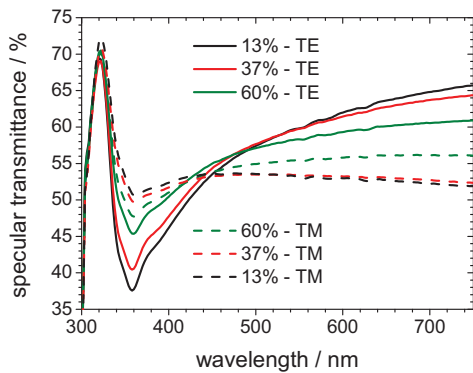


Figure 8.3: Specular transmittance spectra for aligned silver nanowire films illuminated with TM (dotted) and TE (solid) polarized light at varying air humidity.

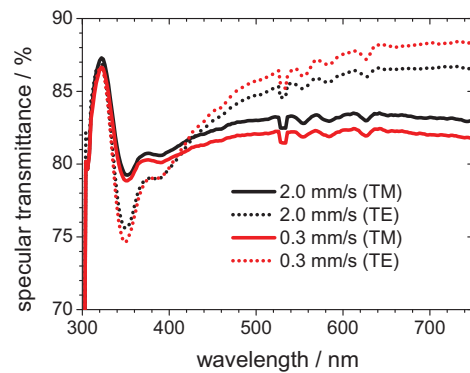


Figure 8.4: Specular transmittance spectra for TE (dotted) and TM (solid) polarized light measured at aligned AgNW films dipped with different withdraw speeds.

and TE polarization is large. With increasing humidity values, the deviation between the curves decreases.

As a second experiment, the anisotropy change for varying pull-out velocities is examined. Figure 8.4 shows the polarization-dependent transmittance for films generated at 2.0 mm/s and 0.3 mm/s which represent the limits of our set-up as mentioned in Section 6.1.1. The small difference in the curve-splitting demonstrates the stability of the anisotropy regarding the velocity (within the limit). Another similar experiment

revealed that the slight differences occur mainly above 1.0 mm/s.

In the following paragraph, four possible explanations for this alignment effect are discussed.

The first is the liquid drainage during the pull-out step. The drainage flow is an inherent effect in the dip-coating process caused by earth gravity as described in experimental Section 5.1. Such a downward solvent stream might result in nanowire orientation (parallel to the stream) due to energy minimization, as shown in artificial flow channels for adjustable velocities.^[264] Furthermore, the effect is described in a patent for tilted (gravity) and rotated (centrifugal force) substrates.^[222]

Secondly, the Marangoni effect has to be mentioned.^[265] It is also a liquid flow, but is induced by deviations in the surface tension of the liquid film. The evaporation of the alcohol results in a temperature drop because of the required latent heat. This leads to an inhomogeneous surface tension distribution. Because the substrate is a heat-sink, the differences vanish towards the substrate and the flow is pronounced rather at the liquid surface. Since, in our case, the liquid film is thin (compared to a worse-wetting droplet) the effect should most likely be small. This conclusion is supported by the fact that the pull-out speed has just a minor influence on the alignment as shown in Figure 8.4. Because the speed is directly connected to the film height, a stronger effect would be expected for higher velocities which is not observed.

Third, the contact line flow known from the renowned coffee ring effect^[218] is discussed. In case of a pinned contact line^C, liquid flows are generated to level out inhomogeneous (unstable) distributions of the film height. The contact line and Marangoni effect are compared in a publication by Deegan *et al.*^[219] The contact line flow is located also at the top of the film and therefore should be weak as aforementioned for Marangoni. Furthermore, as for the Marangoni flow, a stronger influence of the velocity is expected since the film situation is changed completely.

Regarding stream analysis of dip-coating, the publication by Mayer *et al.* is worth mentioning. It illustrates the complexity of flow-structures during the coating process. In addition, they presented an in-situ measurement set-up utilizing an optical microscope in order to analyze the coating situation.^[225]

As a last effect the surface tension itself provides a possible explanation which should be mentioned. While the contact line is passing the substrate, the surface tension exerts force on the nanowires which can lead to a re-orientation. However, an increase of the surface tension by adding water to the solvent (see Figure 8.3) decreases the anisotropy, although a higher surface tension increases the force on the NW. Moreover,

^CThe definition and origin of contact line pinning is well explained in Deegan *et al.*^[218]

qualitative SEM images in Section 6.1.2 show that the film degenerates due to the formation of clusters, whereas the alignment seems to be stable. Therefore, instead of being caused by it, the anisotropy is rather superimposed by a surface tension effect. Although it does not destroy the anisotropy, it is still counterproductive in order to achieve defect-free aligned films.

In consequence, the drainage flow seems to dominate the orientation whereas the other two flow effects are negligible and the surface tension has a negative effect.

Although Huang *et al.* observed no alignment effect with a similar set-up for AgNWs from an ethanol dispersion,^[266] in our experiments the orientation strength is quite stable as long as humidity is kept low. The alignment is observed for all applied nanowire batches and substrates, and even the dip-coating velocity appeared to be almost independent for the examined range.

It is noteworthy that there are other techniques to produce aligned nanowires films (*e.g.* applying shear forces in a contact-printing set-up^[267,268] or roll-printing set-up,^[269] deposition on a growing bubble^[270] or other stretchable substrates,^[271] in a so called Langmuir-Blodgett process^[272] and deposition at a contact line^[266]). A comprehensive review was published by Wang *et al.*^[273]

However, all of these techniques exhibit an insufficient scalability which disqualifies them for industrial application. Furthermore, most of them are unable to control the network structure as it can be done by dip-coating. The network is built up in a cycle-by-cycle process. Each dip-coated nanowire layer can be tuned independently and a tailored network can be produced. Despite the freedom of design, the effort is still moderate. Therefore, this technique is perfect in order to investigate fundamental behaviors of nanowire networks and gain advantages for future applications.

8.1.2 Transmittance Spectra of Nanowire Networks

As already mentioned in the fundamental Section 4.2.2, the detailed optical behavior of nanowire networks is dominated by various effects and thus, appears to be rather complex. Nevertheless, the detailed transmittance behavior is of great importance for solar cell applications as briefly presented in Section 2.3.3.

Therefore, in the following paragraph, the spectra of an anisotropic dip-coated silver nanowire film is analyzed concerning transmittance, reflectance, absorption and scattering. The anisotropy increases the order in the system, compared to random NW networks. In combination with the usage of polarized light, some effects can be separated from each other and therefore a deeper insight in the optical behavior of nanowire

films is obtained.

Total Transmittance, Reflectance and Absorption

Figure 8.5 illustrates the integrated total transmittance and reflectance of a dip-coated aligned nanowire film on glass. In addition, by assuming $A = 1 - R_{\text{total}} - T_{\text{total}}$, absorp-

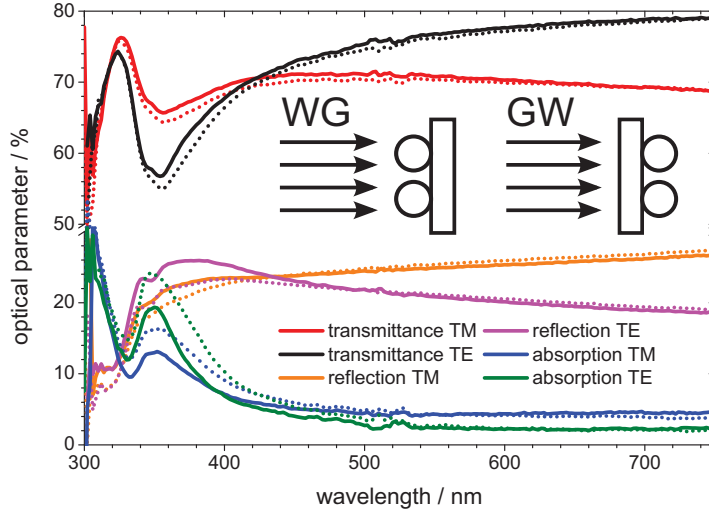


Figure 8.5: Total transmittance, total reflectance and absorption spectra for parallel (TM) and perpendicular (TE) polarization. The curves are measured for glass \rightarrow wire (GW — solid line) and wire \rightarrow glass (WG — dotted line) constellation as defined in the inset.

tion A is calculated and depicted in the graph. The curves are measured for parallel (TM) and perpendicular (TE) polarization from both sample sides (glass \rightarrow nanowire (GW) *vs.* nanowire \rightarrow glass (WG)), as illustrated in Figure 8.5.

In the TM case, the transmittance spectrum T_{total} occurs to be rather flat and slowly increasing towards shorter wavelengths. The slight dip below 400 nm is a result of the imperfect anisotropy and therefore it would vanish in a perfect network^D. The total reflectance R_{total} is also flat, slowly decreasing towards shorter wavelengths. The absorption in this region appears to be small with a value of 4%.

The weak absorption suggests that the transmittance curves are dominated by the reflection of the nanowires. As depicted in Figure 8.7, above 350 nm silver is highly reflective. The reflection graphs are calculated according to n and k values from liter-

^DFor instance the anisotropy of the sample in Figure 8.2 has a better degree of alignment and thus, a weaker dip at this position. Therefore, also the split between the curves is larger.

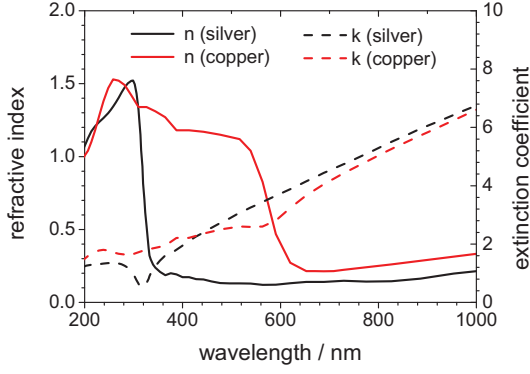


Figure 8.6: Refractive index n and extinction coefficient k for silver and copper taken from literature.^[274]

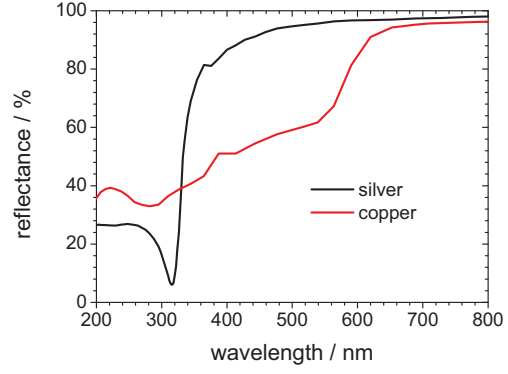


Figure 8.7: Reflectance spectra of a silver and copper surface for normal incidence (deviations for larger angles $< 5^\circ$).

ature^[274] using the reflectivity equation

$$R = \frac{n^2(1 + k^2) + 1 - 2n}{n^2(1 + k^2) + 1 + 2n} \quad (8.1)$$

for normal incidence.^[275] The reflection is a direct result of the electron cloud screening in metal materials. Moreover, also the weak slope in R_{total} and T_{total} can be explained by the reflectance behavior, because a slight change from 800 to 400 nm is visible in Figure 8.7.

As a consequence, for high wavelengths the total transmittance should be directly correlated to the area which is covered with nanowire material (nanowire density n_w), an assumption already used in Section 6.1.1. In order to prove this fact, an aperture value of $(22.1 \pm 4.8)\%$ is obtained by SEM (average of 7 images). At 700 nm in Figure 8.5, $T_{\text{total}} = 70\%$ is reached including glass reflection. Therefore, an aperture $(1 - n_w)$ of about 24% is obtained by using the equation $T_{\text{total}} = 70\% = 92\% \cdot (1 - n_w) + 0 \cdot n_w$, while a glass absorbance of 8% (mainly reflection) and a nanowire absorbance of 100% (mainly reflection, as explained before) are used. The before assumed correlation $n_w \sim (1 - T_{\text{total}})$ seems to be correct.

The high transmittance at 320 nm is a result of plasma resonance and interband transition effects^[276,277] (unlike free-electron plasma resonance which is observed at higher frequency) in the silver material accompanied by the abrupt change of the n, k -values (see data in Figure 8.6). At this point the reflectance drops, (see Figure 8.5) and because of the small diameter, a larger share of incident light is transmitted.

In contrast, for TE polarization a clear asymmetric transmittance dip is visible at around 350 nm causing high transmittance losses. However, in the region above

450 nm the total transmittance is larger than expected for the optical aperture (22% are assumed based on the last paragraph).

These effects are caused by the sub-wavelength dimension of the nanowire cross-section. At a certain wavelength, the light is exciting a localized surface plasmon resonance (LSPR) at the short nanowire axis. In general, for a free-standing particle, such plasmon dips exhibit a symmetric curve.^[179] However, the observed curve is a consequence of an interference between the LSPR re-emission (narrow-band spectrum) and the direct transmission passing the substrate (broad-band spectrum), denoted as Fano resonance^E.^[179,191,278,279] Thus, the exact LSPR should be located at the turning point between destructive (transmittance decrease for $\lambda < 420$ nm) and constructive (transmittance increase for $\lambda > 420$ nm) inference. In addition, the effect is responsible for the asymmetric shape of the dip. The enhancement in the constructive region is larger than the destructive losses at the dip (9% *vs.* 8% - assuming 70.5% transmission at the turning point). Since the transmittance drops towards larger wavelength, the gain is even higher. An averaged transmittance from 300 nm to 800 nm reveals 74.0%, whereas for the parallel polarization (aperture case) just 69.7% are reached. This enhancement is consistent with observations on metal line grids in literature.^[179]

The reflectance in Figure 8.5 demonstrates a similar behavior with a shallow peak at 350 nm due to enhanced plasmonic back-scattering. The peak splitting (dip at 330 nm and 360 nm) might be a result of high order resonances because of deviations in the diameter cross-section (towards higher wavelength: dipole \rightarrow quadrupole).^[191]

As expected from the plasmon theory, some of the light absorbed by the plasmon excitation is lost because of non-radiative damping. Thus, an absorption peak is present at 340 nm. In the region above 500 nm, the absorption is almost negligible, as already mentioned for the parallel case.

In addition, all curves are recorded from both sample sides, as illustrated in the Figure 8.2. In the region above 400 nm, the difference between the curves can be neglected. However, at the plasmonic dip a deviation can be observed.

The detailed origin remains unclear, but two hypotheses are likely. First, an increased incoupling into the substrate might be possible because of the direct contact-interaction between substrate and nanowire (nanowire serves as antenna). Furthermore, the extra absorption is caused by the nanowire itself: In the situation glass \rightarrow nanowire a smaller amount is reaching the nanowire (\approx 8% reflection losses at glass interfaces). As a consequence the absorption in the nanowire is decreased.

^EIn general, the Fano resonance is an interference between a narrow-band and a broad-band electromagnetic wave which is observed in various physical processes.

Forward Scattering

In the literature the scattering behavior of the nanowire electrodes has often been mentioned.^[100,280] Recently, in a collaboration our group published an angular-independent light distribution for a bottom-emission OLED taking a benefit from the scattering behavior.^[241]

Figure 8.8 illustrates the three distinct transmittance types. For TM polarization, the

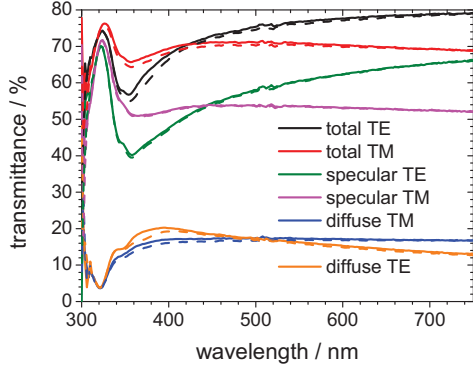


Figure 8.8: Total, specular and diffuse transmittance spectra plotted for both polarizations and sample constellations.

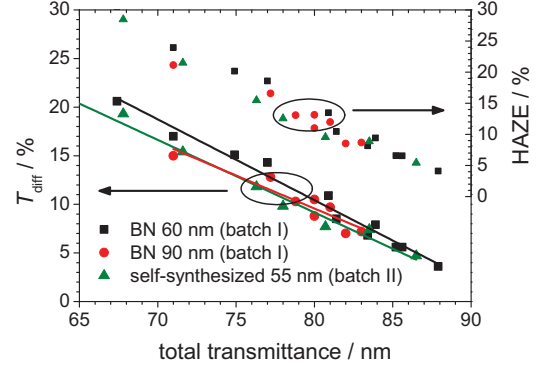


Figure 8.9: T_{diff} (left) and the HAZE (right) are plotted utilizing data from Figure 6.14 and from a self-synthesized AgNW batch.

diffuse part (difference between total and specular transmittance) is flat above 400 nm. Therefore, the scattering is completely wavelength independent. As a consequence, this scattering share cannot be attributed to plasmonic effects and Mie-scattering.

The ratio between total and diffuse transmittance denoted as HAZE-factor H_t is increasing linearly with growing nanowire density (with $n_w \sim (1 - T_{\text{total}})$), as visible in the right scale of Figure 8.9. The values for nanowires with different diameters show only small deviations. The left scale depicts the corresponding T_{diff} against T_{total} -graph which is fitted with a linear function. The negative slope reveals a value in the range of 0.7–0.8. Furthermore, this observation induces an almost stable value in a $T_{\text{diff}}/(1 - T_{\text{total}})$ -plot. In consequence, a fixed share of the transmittance loss ($1 - T_{\text{total}}$) related to the NW density is scattered. Since the slopes in Figure 8.9 does not differ much, the nanowire diameter (here: examined for ≈ 55 –90 nm) seems to be less important for the scattering efficiency.

The forward scattering is caused by the alternating dielectric constant (refractive index) in the sub-wavelength regime. As a result, the wires act as scattering centers. As the refractive index for silver (see Figure 8.6) is rather constant between 400 and 800 nm, as it is also the case for the glass ($n \approx 1.5$) and air ($n = 1.0$) environment, the scattering efficiency spectra (T_{diff}) is constant. It is worth mentioning, that this

behavior can be observed in a similar way for copper. However, the refractive index of copper exhibits a jump at 600 nm (see Figure 8.6) which causes a jump in the scattering efficiency. The larger refractive index split (copper *vs.* surrounding) above 600 nm results in a larger scattering efficiency (see Figure 7.7).

As noted, the diameter has most likely a minor impact on the scattering part and thus, rather the exact shape seems to be important. For instance, the pressed samples in copper Section 7.2.1 display a deformed structure. In this case, compared to the unpressed results, the $T_{\text{diff}}/(1 - T_{\text{total}})$ -ratios change. The exact origin of the ratio is still puzzling and more data, in particular for copper, is necessary to allow further statements.

The TE polarized scattering (T_{diff}) in Figure 8.8 reveals a peak at 400 nm with decreasing values towards higher wavelengths. Here, the aforementioned sub-wavelength scattering is superposed by the particle scattering effect due to the localized surface plasmon resonance.

It is noteworthy that at 320 nm, the electrode is transmitting almost completely specular light, and moreover the difference between the polarization directions vanishes. As mentioned before, at this wavelength silver is losing its reflectivity (see Figure 8.7) and the refractive index (see Figure 8.6) jumps to higher values in the range of air and glass. Since the scattering is a consequence of the alternating dielectric coefficient, the effect decreases.

As aforementioned, in the region above 350 nm, scattering is observed as a result of particle plasmons (only for TE) and alternating dielectric properties (TE + TM).

Reflection

The reflection spectra of the sample are shown in Figure 8.10. In general, the spectra exhibits the typical behavior with a plasmon peak in TE and a rather flat spectrum for TM polarization. At 320 nm the diffuse reflection vanishes and just the $\approx 8\text{--}9\%$ specular reflection related to the bare glass are measurable, which is described earlier. The most interesting peculiarity is the prominent deviation between GW and WG illumination (notation see Figure 8.2).

The GW constellation reveals much lower diffuse reflectance over the whole spectral range. In-coupling and wave-guiding effects can be ruled out as explanation since no differences between GW and WG set-up are observed in the absorption spectra presented in Figure 8.5. Alternatively, the characteristic can be explained with the differing reflection behavior of glass (specular) and silver nanowire network (mostly diffuse). By assuming an aperture of 100% with 8% reflection for glass and an aperture

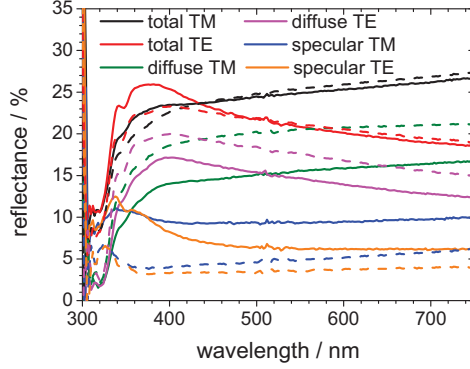


Figure 8.10: Total, specular and diffuse reflectance spectra plotted for both polarizations and sample constellations. The specular reflectance value is calculated with $R_{\text{spec}} = R_{\text{total}} - R_{\text{diff}}$ (no data was recorded).

of $\approx 22\%$ with $\approx 100\%$ reflection for the nanowire network^F, this explanation is sufficient for the TM polarization. For example, for WG illumination (light passes the nanowire network and afterward the glass substrate) the 21% diffuse and the 6% specular reflectance can be perfectly attributed to network and glass losses.

It is noteworthy that the assumed values are ideal and thus, some deviations occur due to the interaction of glass and nanowire. For instance, the origin of the TE reflection is not fully clear and most likely coupling has to be considered.

It has to be mentioned that all spectra are taken from nanowire networks which possess neither a perfect alignment nor a mono-disperse diameter and length distribution. Hence, all effects should be broadened in spectral behavior. Furthermore, the results are specific for systems which merely consist of nanowires on glass. When the electrode is implemented into an extended layer system, the refractive index of the other materials influences the result.

In conclusion, apart from some small deviations most of the effects could be assigned. In particular, the origin of the transmittance curve, which is highly significant for a transparent electrode, could be well explained.

A large fraction of the transmittance directly corresponds to the aperture, whereas the localized surface plasmon resonance causes slight integrated enhancement for the visible range. In particular, for longer wavelength more light passes the aperture than expected.

The forward scattering is dominated by the alternating dielectric constant at the sub-

^FThe chosen parameters are just approximations based on the observations in the penultimate section.

wavelength scale, which leads to a stable scattering intensity all over the visible regime. In addition, a small amount of scattering is related to the LSPR with a peak at around 400 nm.

8.2 Resistance Effects and Application

8.2.1 Conductivity and Percolation Behavior

Besides the optical consequences, also changes in the conductance of the network arose from the anisotropy. The field of current transport in anisotropic stick networks is still not fully investigated. Many of the experiments and simulations have been performed on rather limited sizes in transistor-like set-ups.^[281–283] These results cannot be generalized because of the scaling effects,^[281] which are stressed again later on. More relevant are the data obtained for polymer fibers containing oriented CNT bundles.^[284,285] Furthermore, for a two dimensional film, the anisotropic conductivity was demonstrated recently for a ZnO nanowire network by Phadke *et al.*^[286]

As mentioned in Section 8.1.1, the network structure can easily be tuned with dip-coating in a preferred manner (density, angular distribution). Hence, this method represents a promising opportunity to obtain a deeper insight into this field.

Thus, in order to examine the electrical behavior, samples with various angular nanowire distributions are produced. The corresponding measurement set-up and the used definitions are illustrated in Figure 8.11. All networks produced consist of an equal distribution of nanowires within the angle $\pm\Phi$ around a preferred alignment direction. This structure is achieved by dipping the sample at varying rotation (in 10° steps) positions. For instance, the 15° sample is dipped at rotation angles of -15° , -5° , $+5^\circ$, and $+15^\circ$.

Among the direction dependent two-wire measurements, a four point probe resistivity stand (4PP) is used as described in Section 5.3. In this constellation the 4PP value represents a rather averaged sheet resistance because it does not reflect the anisotropy properly^G. Moreover, it is determined to get an impression for the contact resistance of the two-wire measurement.

In the 90° case (pseudo-isotropic) — in principle the crossed 90° sample corresponds to $\theta = \pm 45^\circ$ — no deviations are observed between the two directions and as expected, the two-wire resistances are higher than the 4PP values which excludes

^GIn this experiment the 4PP sheet resistance is almost independent of the measurement direction. It is noteworthy that in samples with higher alignment (see sample Figure 8.2) this parameter gets also anisotropic.

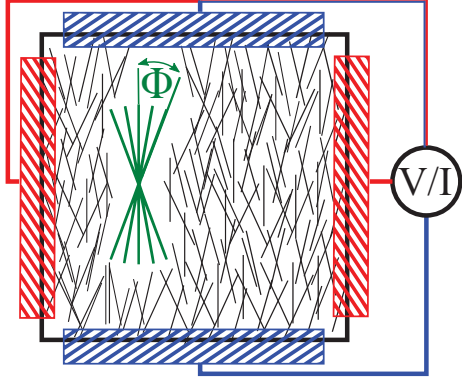


Figure 8.11: The experimental set-up is shown. The angle Φ is the nanowire distribution angle within an equal distribution is assumed. The resistance measurement is performed in a two-wire-mode square set-up parallel (blue, R_{\parallel}) and perpendicular (red, R_{\perp}) to the average alignment direction.

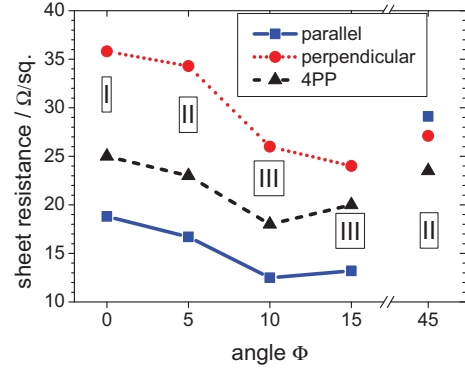


Figure 8.12: The sheet resistance is shown for the two measurement directions in networks with various degrees of alignment and a 90° crossed sample as reference for the random case. Additionally, the 4PP (line set-up explained in Section 5.3) value is plotted.

the contact resistance. In contrast, for the anisotropic networks, a strong split by a factor of 2 can be seen between R_{\parallel} and R_{\perp} direction. The 4PP value is located slightly below the average between the parallel and perpendicular resistance which is expected by assuming the 4PP to be a rather average value without contact resistance. Furthermore, the parallel resistance of all samples is lower than the value in the 90° (pseudo-isotropic) case, which indicates superior transport properties compared to the ‘isotropic’ structure. The best value ($\theta = 0^\circ$) is 55% below the semi-random case which is a tremendous improvement. As a last observation, the three measured resistances decrease with the increasing angular distribution.

In order to explain the anisotropic behavior, first the percolation has to be checked. The percolation threshold is a fixed value for a certain percolation system and thus, is affected by an additional orientation feature. In general, for an infinite network, the isotropic random case has a percolation threshold density of $N_c = f/l^2 = 5.6/l^2$ with nanowire length l .^[124] As aforementioned, with dip-coating rather a semi-isotropic network is achieved, consisting of perpendicular aligned wires ($\Phi = 90^\circ$) produced by rotation of the sample by 90° (see Section 6.1.1). In theory such oriented networks should result in a slightly worse performance with a factor of $f \approx 9.6^H$.^[287] Nevertheless, since the alignment quality of the dip-coated networks is not as high as in the theoretical study, the deviation could not be observed and a random distribution

^HThe value was calculated by Balberg *et al.* in a rather unstable pre-simulation using small nanowire densities and might not be very exact.

is assumed. It has to be mentioned that a patent by the Cambrios Technologies Corporation^[222] claims a contradictory critical percolation factor (theoretical) $f = 2$ which would increase the connectivity. However, neither the corresponding literature citation could be found nor could our results confirm this fact (see also simulations in Section 8.2.2).

Because even the perpendicular orientation ($\Phi = 90^\circ$) exhibits a higher percolation threshold than the random case, it is rather obvious that any kind of anisotropy would lead to an increase of the critical density. Moreover, when Φ is decreasing, the critical density further increases and the network shows a lower connectivity, as mentioned in publications.^[281,287]

Just for small networks with a nanowire length l in the range of the area dimension L , an enhancement compared to the random case is possible and an anisotropic conductivity is observed.^[281] A typical example are transistor set-ups mentioned above. In these systems the percolation threshold splits in a parallel and perpendicular value which thus results in an anisotropic conductivity. However, for infinite areas, the distinction vanishes and also an anisotropic network exhibits an isotropic percolation threshold. Therefore, the conductivity is isotropic, as well.^[287] As a consequence, the conductivity exponent μ in Equation 4.2 should be fixed and isotropic near the percolation threshold. Hence, in fibers or nanowire electrodes (both represent extended percolation systems) the conductivity should be isotropic and aligned networks should be less conductive compared to the random case. Thus, the percolation theory cannot explain the anisotropic conductivity observed in the literature^[284–286] and our experiment.

The explanation of the effect can be found by increasing the nanowire density. As mentioned in Section 4.1.2, network electrodes possess nanowire densities well above the percolation threshold, even reaching the bulk regime because otherwise conductivity would be too low. Balberg *et al.* mentioned already in 1983 that for densities far above the percolation threshold, anisotropic conductivity might be possible.^[287] In this situation the percolation is already well established and extra nanowires just add further current paths. This case was recently investigated by Li and Zhang. For these networks the ratio between junction resistance R_j and wire resistance R_w starts to matter and the critical exponent μ is substituted by an so-called apparent exponent.^[124] Although not addressed in literature, this apparent exponent might explain the anisotropic conductivity, as well. Additional nanowires with an preferred alignment improve the current transport in a certain direction by bridging not aligned nanowires and junctions. Therefore, the conductivity splits into two values and even superior values might be possible compared to a random structure.

Based on this theory, the graph of Figure 8.12 can be explained. The deviation between the parallel and perpendicular sheet resistance (R_{\parallel}/R_{\perp}) is a result of a split of the apparent exponent. Since the density is well above the percolation threshold, the aligned nanowires preferentially bridge junctions in the alignment direction. Thus, the resistance parallel to the nanowires exhibit values below the average random resistance.

It is noteworthy that some points in the curve are still not fully explained. For all aligned networks, the resistance values are dropping with decreasing orientation. Either this effect is attributed to percolation effects, which actually are rejected in this paragraph, or it is an artifact, which is caused by deviations in the nanowire density, because of the complicated dipping of rotated samples^I. Thus, in order to provide some additional experimental data, the run number of the samples is added to the Figure 8.12^J. Less material might be deposited in the later runs as a result of changing NW concentration. This would also explain, why for the 10° and 15° sample even the perpendicular resistance exhibits values below the random value. Further experiments have to show whether this dependency can be confirmed.

Nevertheless, the general effect of anisotropic conductivity is well proven and is observed for BN and self-synthesized wires.

8.2.2 Electrical Simulation

The last section demonstrated that the resistance of an aligned network can be smaller than in the random case. In the following section, resistance simulations should be used to reproduce this anisotropic effect and seek for optimized alignment structures. Similar calculations were already performed for transistor-like structures.^[281–283,288] Topinka *et al.* published an extensive colorful study of a random CNT network calculating current, resistance and voltage for various densities.^[289] Additionally, this approach was also transferred to large scale transparent networks.^[286]

However, it turned out that for the case of nanowire length $l \approx$ film dimension L , these simulations might not be reliable.^[288] The publications do not dispel these doubts. Unfortunately, because of a lack of investigation time and hardware resources, these tests are not performed for our experiment, as well.

Nevertheless, the approach and the results are shown in the following section. In ad-

^IThe tuning of the angular distribution requires many mount and unmount steps. Moreover, dipping of rotated substrates increases material consumption due to the increased parasitic deposition at the edges. Unfortunately, the analysis of the density by UV-vis is less reliable because the anisotropy is effecting the spectra — the fluctuations are in the range of 3%.

^JAs mentioned before, with each run two samples are dipped back-to-back

dition, some comments regarding the reliability are also provided.

Simulation Approach

The nanowire network is generated with “QtOctave“, a user interface for the numerical computation program GNU Octave. It is free open-source software, which is distributed under the terms of the GNU general public license (GPL). At the beginning, linear equations are generated, which fulfill the distribution and orientation requirements at random position within the network boundaries. Because of the large aspect ratio the nanowire volume is neglected. Afterward the relevant intersections are determined. In addition, contact areas are introduced on both sides. Here all intersections within a certain ‘contact‘ area are connected resistance-free to a single node, which defines the potential of the contact area. The network between the contacts has a square shape. Thus, the resistance in-between is equal to the sheet resistance of the network. An illustration of a random (a) and an aligned (b) case including contact connections (to the left and right of the network) are depicted in Figure 8.13.

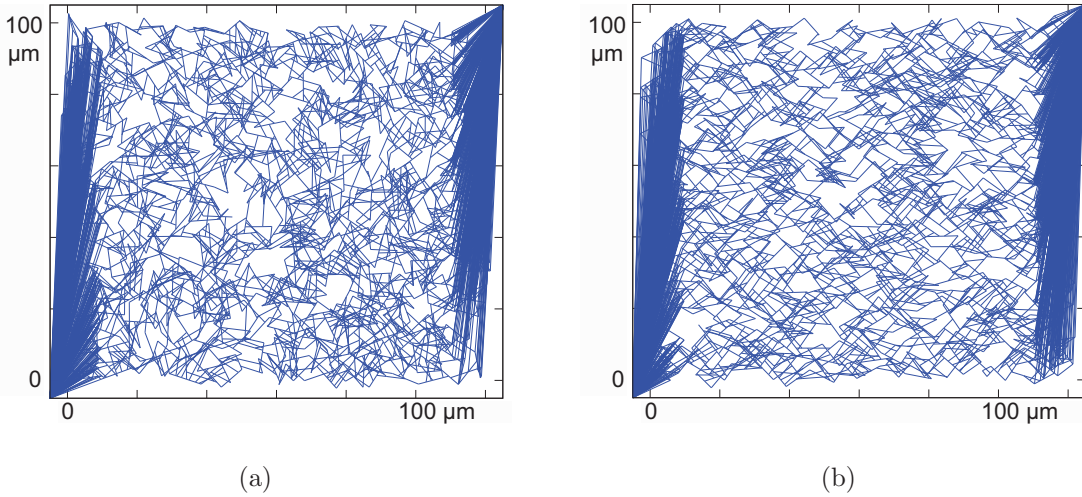


Figure 8.13: Generated nanowire network ($L = 100 \mu\text{m}$) with 1630 nanowires ($l = 10 \pm 0.2 \mu\text{m}$ — normal distribution) for the fully random case (a) with $R_{\parallel} = 55 \Omega/\text{sq.}$ and for a random distribution within $\Phi = \pm 40^\circ$ (b) with $R_{\parallel} = 44 \Omega/\text{sq.}$ Because $10 \mu\text{m}$ on each side are used for the contacts, a number of 1960 nanowires is simulated on an area of $100 \times 120 \mu\text{m}^2$.

Subsequently, each intersection is assigned to a simulation node and the connections are replaced by the according resistance value. Moreover, the intersections can be split into two nodes, while the connection in-between is set as the contact resistance. The final ASCII document consists of a list of all resistors with its two respective node numbers.

This ASCII file is handed-over to a “SPICE“ integrated circuit solver, in my case the

open source program ‘ngspice’. The solving algorithm is presented in the experimental Section 5.3. As a result an averaged sheet resistance value is achieved, which is obtained out of 5 (random and $\pm\Phi$ case) or 10 (two-direction $+\Phi/ -\Phi$ case) independently generated networks.

Results and Discussion

Figure 8.14 shows the calculated sheet resistances (normalized to the isotropic random value) against the alignment angle Φ . Moreover, the curve is simulated for various wire densities. As nanowire resistance $25 \pm 5 \Omega/\mu\text{m}$ is chosen, which was obtained by Hu *et*

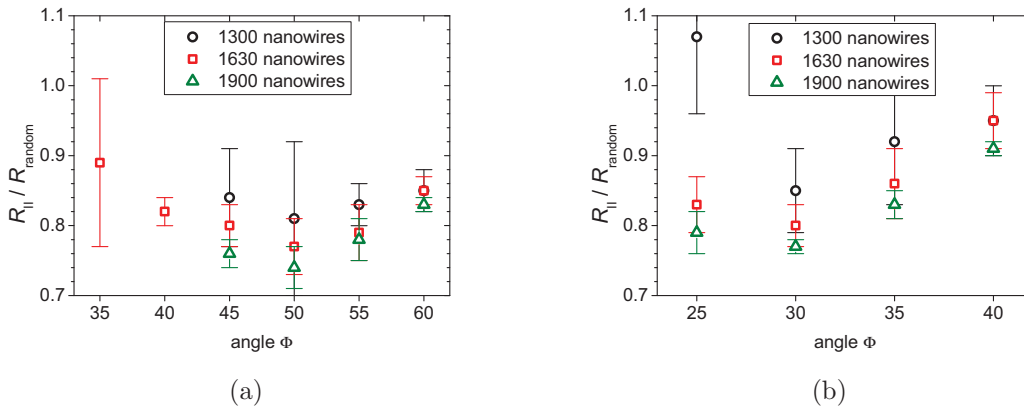


Figure 8.14: Calculated sheet resistance values for $100 \times 100 \mu\text{m}$ nanowire networks with 1300 (black), 1630 (red) and 1900 (green) nanowires for a continuous distribution within $\pm\Phi$ (a) and for a two-direction alignment with just $+\Phi/ -\Phi$ (b). The values are normalized to the completely random distribution with $R_{\text{random}} = 84 \Omega/\text{sq.}$ (1300), $R_{\text{random}} = 54 \Omega/\text{sq.}$ (1630) and $R_{\text{random}} = 42 \Omega/\text{sq.}$ (1900).

al. measuring in four-wire mode.^[100] The length of the nanowires is $l = 10 \pm 0.2 \mu\text{m}$. For both values a normal distribution is used. The sheet resistance values for the networks are within the expected range (*e.g.* the random network in Figure 8.14(a) exhibits a sheet resistance of $54 \Omega/\text{sq.}$ for $0.163 \text{ wires}/\mu\text{m}^2$ which corresponds to the 1630 nanowire case).

However, this work does not strive a complete comparisons between calculated and measured values concerning conductivity and transmittance. This correlation would require the correct values for the length, diameter and angular distribution of the nanowires. Furthermore, also the exact wire and junction resistance are necessary. Instead, just a qualitative analysis of the principle effects is performed.

In Figure 8.14(a) the nanowires are continuously distributed between $\pm\Phi$. The sheet resistance in parallel direction R_{\parallel} is normalized to the completely random

network R_{random} and plotted against the angle Φ . The curve presents a clear minimum at an angle of 50° , whereas the value does not depend on the nanowire density in the investigated region. The gain is in the range of 25% with slightly superior values for higher densities. In this case the network is farther away from the percolation regime and thus, the improvement due to the alignment might be pronounced, as described in the previous section.

In the case of a network which just consists of two different nanowire directions^K ($+\Phi/-\Phi$), the behavior is slightly different. As depicted in Figure 8.14(b) the minimum is at an angle of 30° . The deviation can be explained by the fact that the parallel wires ($\Phi = 0^\circ$) are more important, since the parallel share is responsible for the preferred resistance direction. Thus, because just two directions are present, their orientations have to shift towards smaller angles. Further interpretation might not be useful since the amount of data is rather limited.

It is noteworthy that both curves show a stable minimum independent of wire density. Thus, the simulation results most likely are stable and reliable, which is further discussed at the end of this paragraph.

Along with wire density, also contact resistance R_j is investigated and varied between negligible and $1\text{ k}\Omega$. The calculations are performed for the network with a wire density of $0.163\text{ wires}/\mu\text{m}^2$ (1630 nanowires are used), as presented in Figure 8.14(a). Figure 8.15 is illustrating the results, whereas the black circles^L for 0Ω are taken from Figure 8.14(a).

The minimum distribution angle remains unaffected, as observed for the variation of the density. The absolute sheet resistance increases for the increasing junction resistance as expected. However, for the depicted normalized values, no clear trend regarding an improvement is visible. Moreover, the sheet resistance values are less reliable although 10 simulation cycles are applied. Compared to the 0Ω calculations, the errors with included contact resistance are increasing from about 3% to roughly 10% with some pronounced runaways. Therefore, further calculations have to be performed in order to gain a clear picture.

A publication by Hecht *et al.* is worth mentioning regarding contact resistance in conductive networks.^[128] This work deals with the ratio of junction *vs.* tube resistance in random CNT films. In combination with comments by Lu *et al.*,^[250] for higher

^KThis case is not realized in the experiments of the previous section. However, the structure is much easier to realized because just two dipping directions are required.

^LIt has to be mentioned that for this calculation the R_j is excluded in the program code. A contact resistance of 0Ω results in node connections with conductivities of $\rightarrow \infty$ which causes problems in the solving algorithm.

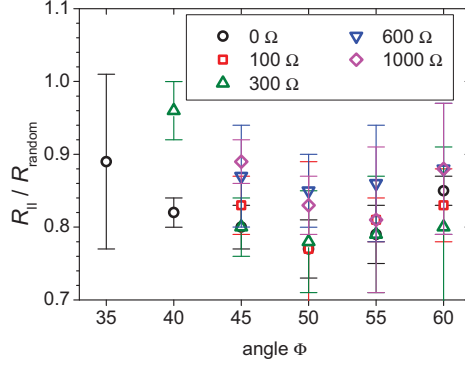


Figure 8.15: Calculated sheet resistance values for $100 \times 100 \mu\text{m}$ nanowire networks with 1630 nanowires for a random distribution within $\pm \Phi$ for various contact resistances of 0Ω (black), 100Ω (red), 300Ω (green), 600Ω (blue) and 1000Ω (magenta). The values are normalized to the completely random distribution with $R_{\text{random}} = 54 \Omega/\text{sq.}$ (0Ω), $R_{\text{random}} = 80 \Omega/\text{sq.}$ (100Ω), $R_{\text{random}} = 126 \Omega/\text{sq.}$ (300Ω), $R_{\text{random}} = 182 \Omega/\text{sq.}$ (600Ω) and $R_{\text{random}} = 270 \Omega/\text{sq.}$ (1000Ω).

contact resistances, the anisotropic conductivity is expected to be more pronounced. In this situation the bridging effect in a preferred direction should be of advantage. However, this dependency is not observed and thus the hypothesis cannot be validated.

As mentioned already in the introduction of this section, for small ratios between nanowire length and film dimensions as in our simulations ($l : L = 1/10$), the edge of the film cannot naturally be neglected. Thus, the reliability of the approach has to be discussed. In these small percolation networks, a direction-dependent percolation threshold might be observed^[287] as mentioned earlier. However, in unlimited systems this dependency vanishes.

The stable angular minimum for differing densities might support the reliability of the calculations and thus the simulated system size might be sufficient. However, this evidence is weak and therefore not convincing enough. The exact density above which the network gets less-dependent or independent of the percolation effect (region III/IV in Figure 4.2) is unknown. Therefore, the network might still be driven by the percolation. Moreover, the calculations performed for varying junction resistances show a fluctuating behavior without clear trends. As discussed above, this contradicts the expected behavior and therefore might demonstrate the reliability problems.

Hence, simulations of various film dimensions are necessary in order to test the reliability. Furthermore, the different network regions (from percolation towards bulk regime) could be investigated. However, by increasing the film size and thus the node number both the calculation time and memory consumption are rising. Unfortunately, such extended node systems (> 100000 nodes) cannot be solved with the simple SPICE

approach on a state of the art personal computer (RAM: 4GB; CPU: Intel Core2 Duo E8400). Besides using a more sophisticated machine, also alternative approaches for solving the problem can be chosen. Some algorithms are suggested in the book by Stauffer and Aharony.^[113]

8.2.3 Optimized Network Structure and Application

The anisotropic networks in the previous sections demonstrate conductivity values above that of random structures. Therefore, the behavior might be interesting for transparent electrode application. Figure 8.16 illustrates a possible monolithic layout which benefits from the anisotropy. The long and narrow rectangular pixels are

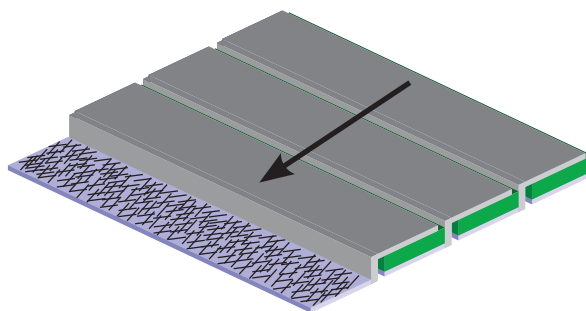


Figure 8.16: Application scenario of an electrode showing anisotropic conductivity. The low resistance direction is marked with a black arrow.

connected in series at the length side. The current transport is performed as marked along the short axis. Therefore, this resistance is important for the current transport, whereas the length axis plays a negligible role. In this constellation, an anisotropic conductivity increase along this transport direction would be of great advantage. As a result, in a solar cell module the losses would be decreased.

8.3 Conclusion

The production of anisotropic nanowire networks by dip-coating is reported and the origin of the effect is discussed. A comparison with alternative methods reveals the advantage of the alignment by dip-coating. Aligned nanowires show a strong polarization-dependent transmittance behavior, which is caused by deviations in the absorption for the respective axis of high aspect nanowires. Therefore, an anisotropic network is used to do a full optical characterization of these nanostructured films, whereas the random case is just a superposition of the aligned networks. Besides that, electrical behavior is examined. The anisotropic conductivity is explained including a short literature review. In simulations and experiments various densities, angular distributions and

contact resistances are investigated searching for an optimized structure. Anisotropic conductivities above that of a random structure are observed, which might be interesting for an application as transparent electrode.

The anisotropic networks are a perfect model system in order to investigate the optical and electrical behavior of nanowire networks. In particular for the conductivity, the presented adjustable networks provide a promising opportunity to achieve a deeper insight in the conductivity behavior at various density regimes of stick-like percolation networks.

Chapter 9

Conclusion and Outlook

In this thesis, metal nanowire networks are investigated as transparent electrodes for small-molecule organic solar cells. This electrode approach combines the high conductivity of metals with a network structure offering a large aperture to transmit the majority of incident light. Furthermore, nanowire electrodes offer several advantages, as flexibility, solution-processability, and low material consumption.

The major part of this thesis focuses on the production and integration process of metal nanowire electrodes into sm-OSCs. The single production steps are investigated in order to isolate crucial points, understand underlying effects, and seek for improvements.

As nanowire materials, silver and copper are examined, both exhibiting a high conductivity. Silver is a stable noble metal system, whereas the less noble copper is characterized by its higher abundance.

For the deposition of NWs, first, a dip-coating process is discussed in detail. The coating mechanism is explained and influencing parameters are investigated. Dip-coating is a well controlled process resulting in homogeneous NW films. Subsequently, the findings are transferred to a spray-coating process, introduced as an alternative technique. Spray-coating allows faster deposition of extended coating areas, while the deposition mechanisms for alcohol-based NW dispersions remain similar. Both methods are scalable, can perfectly be controlled, and result in homogeneous networks. After deposition, the nanowire networks are barely conductive. Therefore, silver nanowires are annealed in air to achieve a tremendous conductivity enhancement. A minimum in resistance is reached depending on temperature, treatment time, and atmosphere. As a result, a performance ($< 20 \Omega/\text{sq.}$ at $> 85\%$ transmittance) comparable to commonly applied ITO electrodes is achieved. The initial contact problems are related to the insulating capping-shell around the nanowires which

hinders current flow at the NW junctions. The capping is inevitable since it is a result of the synthesis and, moreover, has to be present for the dispersability.

In contrast to silver, copper shows strong oxidation and therefore, annealing in air would be counterproductive. A pressing step, which is known as annealing alternative for AgNWs, does not result in the expected performance improvement. Thus, the insulating shell is assumed to be much thicker and more stable than for silver. Copper oxide is identified as reason for the contact problems. A reduction under hydrogen-flow at elevated temperatures is applied and results in a performance ($24\ \Omega/\text{sq.}$ at 82% transmittance) comparable to silver. In addition, the reduction process changes the transmittance spectra. This behavior, caused by Cu_2O , can be used to track the re-oxidation. In air, the spectrum degrades within hours and the network reaches a pre-reduction state. Nevertheless, the resistance increase is moderate because the nanowire junctions are reasonable stable, once formed. Therefore, in particular at room temperature, the CuNW electrode is relatively stable, and in encapsulated devices the sheet resistance should remain low. However, sensitivity regarding oxidation strongly depends on the nanowire diameter, as demonstrated in experiments with CuNWs of various diameters. The thinner the nanowires, the more critical is the oxidation.

It is noteworthy that although the sheet resistance of networks with thicker nanowires stays low for a long time, the thin oxide layer on the nanowires can result in problems. In solar cells, the insulating layer can hinder the current transport between organic layer and metal grid.

The main drawback of NW electrodes is their inherent roughness. Organic solar cell stacks are extremely thin and therefore steps in the range of the layer thickness cause shunts. In this work, a highly conductive PEDOT:PSS is used to planarize the topography. The spin-coated layer slightly decreases the structure height and, even more important, the steps are smoothed out. A 40 nm PEDOT:PSS layer is already sufficient to achieve an acceptable surface, as long as the NW film is free of large agglomerates. Furthermore, the planarization approach is enhanced by adding the polymer PVP to the original PEDOT:PSS solution. Therefore, the film thickness can be increased by 10-times whereas the parasitic absorption of the film remains constant. In order to produce a solar cell, the electrode has to be structured in a certain layout. This process appears to be quite crucial because of the small pixel size in our experiments. The applied laser process generates high structure steps and uncovered NWs at the pixel edge. These defects increase the current leakage and decrease efficiency. Thus, several methods are tested to seek for an alternative, while a screen-printing process of a passivation layer works best.

Finally, OSCs are processed on top of the planarized NW electrode. The produced

ZnPc:C₆₀ cells reach almost ITO performance with the respective efficiency of 2.3% (AgNW) and 2.5% (ITO). Variations in stack structure show that the HTL thickness has only a minor influence on the leakage current and that the solution-processed planarization layers are mandatory. Nevertheless, the leakage currents are still orders of magnitude higher compared to a standard ITO electrode. A detailed surveillance reveals that this effect is mainly attributed to leakage paths at large agglomerates. The agglomerates are already present in the dispersion and therefore, its quality strongly influences electrode performance.

The last part of this thesis describes an anisotropic alignment effect caused by the dip-coating deposition. The NWs are preferentially aligned parallel to the dipping direction. The origin of the alignment and corresponding parameters are discussed. The effect allows the tuning of the network structure, from fully parallel nanowires, *via* constrained angular distributions, up to a random structure. Moreover, the approach is scalable and works without complicated intermediate steps.

The high degree of order in the fully parallel case is used to obtain a deeper insight in silver nanowire network optics. The aligned networks exhibit a polarization-dependent spectrum. Apart from the nanowire density related aperture, spectra are strongly affected by the polarization-dependent excitation of localized surface plasmons. In contrast, the scattering efficiency is almost independent of polarization and is dominated by the sub-wavelength nanowire size.

Along with the optical consequences, an interesting electrical behavior is observed. The anisotropy causes an anisotropic conductivity, while the value can be superior (an increase up to 50% is measured) compared to a random structure with same NW density. The origin of this effect is discussed and samples with various angular NW distributions are examined. Furthermore, electrical circuit simulations are performed in order to reproduce the anisotropy and obtain qualitative statements concerning structure optimization. At the end a possible application scheme is presented briefly.

The implementation of NW electrodes into small-molecule organic solar cells was demonstrated successfully for silver and copper nanowires. If dispersions without agglomerations and transparent solution-based planarization layers are used, solar cell jV-curves will achieve ITO-like performance. Thus, further research has to pay attention to the improvement of the electrode performance.

Apart from increasing the nanowire length in the synthesis, future developments have to focus on the post-processing of the networks to achieve higher conductivities. In order to enable industrial roll-to-roll application on polymer foils, low temperature processes combined with short treatment times are required. The crucial point is the

contact area at the nanowire junctions. In general, an enhanced adhesion between nanowire and substrate might be of advantage for future progress. In combination with the nanowire ductility, the junction area is enlarged. This improves the conductive contact and furthermore, protects the junction from undesired chemical reactions like oxidation.

For copper nanowires, additionally, the oxide layers have to be eliminated. Apart from hydrogen, less critical reduction agents can be applied (*e.g.* formic acid). A room temperature alternative might be the removal of oxides by a solvation process in pure acids. Furthermore, the re-oxidation has to be blocked to avoid insulating barriers and improve lifetime. The deposition of noble metals might be a possible way, while a partly coverage might be sufficient for current transport. If these issues are solved, copper might be the best choice for metal network electrodes. It combines high performance with high material abundance.

PEDOT:PSS is an acidic and hygroscopic polymer. Thus, more effort has to be invested in the development of planarization layers processable without water at low temperatures. The aforementioned solution-processed HTLs might be a promising approach to achieve this goal. Additionally, the quality of the dispersion (less agglomerates) has to be improved because this would lower demand for planarization. Anisotropic networks offer a great opportunity to further improve the electrode. First, the additional insight in the optical behavior can be used to investigate the effect of various environments on transmittance and scattering. In particular, the scattering might have a large influence on the cell performance. Second, the superior conductivity behavior in aligned structures has to be further optimized. Simulations on larger areas have to show if the presented explanation is correct and how an optimized network structure has to look like. Moreover, the optimized structure can be implemented into large area devices to prove relevance regarding application.

In this thesis, the whole process chain necessary for the application of metal nanowire networks in transparent electrodes for organic solar cells was investigated. Additionally, the origin of fundamental properties were addressed. The results confirmed the promising performance of this electrode type and showed the path towards more efficient structures.

The metal nanowire networks are of interest for every electronic device with need for a transparent electrode. Especially flexible OSCs produced in large-scale mass-production would profit from such an electrode approach.

Bibliography

- [1] U.S. Energy Information Administration, International Energy Statistics, <http://www.eia.gov/countries/>, accessed: 06/27/2013.
- [2] U.S. Energy Information Administration, International Energy Outlook 2013, <http://www.eia.gov/countries/reports.cfm>, accessed: 08/31/2013.
- [3] IEA, *World Energy Outlook 2010*, **2010**.
- [4] P. Bethge, *Spiegel Online*, <http://www.spiegel.de/spiegel/print/d-80818274.html>, **2011**.
- [5] IPCC, *Fourth Assessment Report, AR4*, **2007**.
- [6] TU Graz, Grundlagen der Sonnenenergieeinstrahlung, <http://portal.tugraz.at/portal/page/portal/Files/i3070/downloads/skripten/Sonnenenergienutzung/Teil2\Grundlagen.pdf>, accessed: 07/25/2013.
- [7] G. Knies, H. Graßl, F. Trieb, *DESERTEC-Atlas*, CEP Europäische Verlagsanstalt, **2011**.
- [8] C. Morris, *heise online*, <http://www.heise.de/tp/artikel/37/37226/1.html>, **2012**.
- [9] V. Fthenakis, E. Alsema, *Progress in Photovoltaics: Research and Applications* **2006**, *14*(3), 275–280.
- [10] Heliatek GmbH, Neuer Weltrekord für organische Solarzellen: Heliatek behauptet sich mit 12% Zelleffizienz als Technologieführer., <http://tinyurl.com/13zz9fs>, accessed: 06/19/2013.
- [11] M. A. Green, K. Emery, Y. Hishikawa, W. Warta, E. D. Dunlop, *Progress in Photovoltaics: Research and Applications* **2013**, *21*(1), 1–11, DOI 10.1002/pip.2352.
- [12] A. E. Becquerel, *Compt. Rend. Acad. Sci.* **1839**, *9*, 561–567.
- [13] M. K. Riede, doctoral thesis, Universität Konstanz, **2006**.
- [14] P. Würfel, *Physics of Solar Cells*, 2nd ed., Wiley-VCH Verlag GmbH, Weinheim, Germany, **2005**, DOI 10.1002/9783527618545.
- [15] S. M. Sze, *Physics of semiconductor devices*, Wiley, New York, U.S., **1981**.

- [16] M. Schwoerer, H. C. Wolf, *Physik Journal* **2008**, 29–32.
- [17] B. Bolto, R. McNeill, D. Weiss, *Australian Journal of Chemistry* **1963**, 16(6), 1090, DOI 10.1071/CH9631090.
- [18] C. Chiang, C. Fincher, Y. Park, A. Heeger, H. Shirakawa, E. Louis, S. Gau, A. MacDiarmid, *Physical Review Letters* **1977**, 39(17), 1098–1101, DOI 10.1103/PhysRevLett.39.1098.
- [19] M. Schwoerer, H. C. Wolf, *Organic Molecular Solids*, Wiley-VCH, **2007**.
- [20] M. Pope, C. S. Swenberg, *Electronic Processes in organic Crystals and Polymers*, Oxford University Press, **1999**.
- [21] W. Brütting, *Physics of Organic Semiconductors*, Wiley-VCH, **2005**.
- [22] K. Leo, Organic Semiconductor World, <http://www.orgworld.de>, accessed: 12/14/2012.
- [23] C. Falkenberg, doctoral thesis, TU Dresden, **2011**.
- [24] N. Karl, in *Festkörperprobleme 14*, vol. 14, (Ed. by H. J. Queisser), Friedr. Vieweg & Sohn Verlagsgesellschaft mbH, **1974**, p. 261, DOI 10.1007/BFb0108470.
- [25] R. Boyer, Interactive Concepts in Biochemistry, <http://www.wiley.com/college/boyer/0470003790/index.htm>, accessed: 02/11/13.
- [26] J.-L. Brédas, J. E. Norton, J. Cornil, V. Coropceanu, *Accounts of Chemical Research* **2009**, 42(11), 1691–9, DOI 10.1021/ar900099h.
- [27] B. P. Rand, J. Genoe, P. Heremans, J. Poortmans, *Progress in Photovoltaics: Research and Applications* **2007**, 15(8), 659–676, DOI 10.1002/pip.788.
- [28] C. Deibel, V. Dyakonov, *Reports on Progress in Physics* **2010**, 73(9), 096401, DOI 10.1088/0034-4885/73/9/096401.
- [29] P. G. Nicholson, F. A. Castro, *Nanotechnology* **2010**, 21(49), 492001, DOI 10.1088/0957-4484/21/49/492001.
- [30] N. Karl, J. Marktanner, *Molecular Crystals and Liquid Crystals Science and Technology. Section A. Molecular Crystals and Liquid Crystals* **2001**, 355(1), 149–173, DOI 10.1080/10587250108023659.
- [31] M. Pfeiffer, K. Leo, X. Zhou, J. Huang, M. Hofmann, A. Werner, J. Blochwitz-Nimoth, *Organic Electronics* **2003**, 4(2-3), 89–103, DOI 10.1016/j.orgel.2003.08.004.
- [32] J. Huang, J. Blochwitz-Nimoth, M. Pfeiffer, K. Leo, *Journal of Applied Physics* **2003**, 93(2), 838, DOI 10.1063/1.1533838.
- [33] T. Menke, doctoral thesis, TU Dresden, **2013**.

- [34] T. Menke, D. Ray, J. Meiss, K. Leo, M. Riede, *Applied Physics Letters* **2012**, *100*(9), 093304, DOI 10.1063/1.3689778.
- [35] C. W. Tang, *Applied Physics Letters* **1986**, *48*(2), 183, DOI 10.1063/1.96937.
- [36] K. Walzer, B. Maennig, M. Pfeiffer, K. Leo, *Chemical Reviews* **2007**, *107*(4), 1233–71, DOI 10.1021/cr050156n.
- [37] W. Tress, K. Leo, M. Riede, *Advanced Functional Materials* **2011**, *21*(11), 2140–2149, DOI 10.1002/adfm.201002669.
- [38] M. Riede, C. Urich, J. Widmer, R. Timmreck, D. Wynands, G. Schwartz, W.-M. Gnehr, D. Hildebrandt, A. Weiss, J. Hwang, S. Sundarraj, P. Erk, M. Pfeiffer, K. Leo, *Advanced Functional Materials* **2011**, *21*(16), 3019–3028, DOI 10.1002/adfm.201002760.
- [39] A. Sharma, B. Kippelen, P. J. Hotchkiss, S. R. Marder, *Applied Physics Letters* **2008**, *93*(16), 163308, DOI 10.1063/1.2998599.
- [40] A. Elschner, S. Kirchmeyer, in *Organic Photovoltaics*, (Ed. by C. J. Brabec, V. Dyakonov, U. Scherf), Wiley-VCH, chapt. XII, **2008**, p. 213.
- [41] D.-S. Leem, A. Edwards, M. Faist, J. Nelson, D. D. C. Bradley, J. C. de Mello, *Advanced Materials* **2011**, 4371–4375, DOI 10.1002/adma.201100871.
- [42] B. de Boer, A. Hadipour, M. M. Mandoc, T. van Woudenberg, P. W. M. Blom, *Advanced Materials* **2005**, *17*(5), 621–625, DOI 10.1002/adma.200401216.
- [43] W. Tress, doctoral thesis, TU Dresden, **2012**.
- [44] J. Meiss, M. K. Riede, K. Leo, *Applied Physics Letters* **2009**, *94*(1), 013303, DOI 10.1063/1.3059552.
- [45] M. Thomschke, R. Nitsche, M. Furno, K. Leo, *Applied Physics Letters* **2009**, *94*(8), 083303, DOI 10.1063/1.3088854.
- [46] L. Müller-Meskamp, Y. H. Kim, T. Roch, S. Hofmann, R. Scholz, S. Eckardt, K. Leo, A. F. Lasagni, *Advanced Materials* **2012**, *24*(7), 906–910, DOI 10.1002/adma.201104331.
- [47] J. B. Kim, P. Kim, N. C. Pégard, S. J. Oh, C. R. Kagan, J. W. Fleischer, H. A. Stone, Y.-L. Loo, *Nature Photonics* **2012**, *6*(5), 327–332, DOI 10.1038/nphoton.2012.70.
- [48] M. W. Rowell, M. D. McGehee, *Energy & Environmental Science* **2011**, *4*(1), 131, DOI 10.1039/c0ee00373e.
- [49] G. Haacke, *Journal of Applied Physics* **1976**, *47*(9), 4086, DOI 10.1063/1.323240.
- [50] V. K. Jain, A. P. Kulshreshtha, *Solar Energy Materials* **1981**, *4*(2), 151–158, DOI 10.1016/0165-1633(81)90038-1.

- [51] D. B. Fraser, H. D. Cook, *Journal of The Electrochemical Society* **1972**, *119*(10), 1368, DOI 10.1149/1.2403999.
- [52] S. De, T. M. Higgins, P. E. Lyons, E. M. Doherty, P. N. Nirmalraj, W. J. Blau, J. J. Boland, J. N. Coleman, *ACS Nano* **2009**, *3*(7), 1767–74, DOI 10.1021/nm900348c.
- [53] M. Dressel, G. Grüner, *Electrodynamics of Solids*, Cambridge University Press, **2002**.
- [54] C. Lungenschmied, G. Dennler, H. Neugebauer, S. N. Sariciftci, M. Glatthaar, T. Meyer, A. Meyer, *Solar Energy Materials and Solar Cells* **2007**, *91*(5), 379–384, DOI 10.1016/j.solmat.2006.10.013.
- [55] Y. Galagan, J.-E. J.M. Rubingh, R. Andriessen, C.-C. Fan, P. W.M. Blom, S. C. Veenstra, J. M. Kroon, *Solar Energy Materials and Solar Cells* **2011**, *95*(5), 1339–1343, DOI 10.1016/j.solmat.2010.08.011.
- [56] S. Choi, W. J. Potscavage, B. Kippelen, *Journal of Applied Physics* **2009**, *106*(5), 054507, DOI 10.1063/1.3211850.
- [57] K. Bädeker, *Annalen der Physik* **1907**, *327*(4), 749–766, DOI 10.1002/andp.19073270409.
- [58] A. Stadler, *Materials* **2012**, *5*(4), 661–683, DOI 10.3390/ma5040661.
- [59] L. Castañeda, *Materials Sciences and Applications* **2011**, *02*(09), 1233–1242, DOI 10.4236/msa.2011.29167.
- [60] C. G. Granqvist, *Applied Physics A Solids and Surfaces* **1993**, *57*(1), 19–24, DOI 10.1007/BF00331211.
- [61] H. Kim, C. M. Gilmore, A. Piqué, J. S. Horwitz, H. Mattoussi, H. Murata, Z. H. Kafafi, D. B. Chrisey, *Journal of Applied Physics* **1999**, *86*(11), 6451, DOI 10.1063/1.371708.
- [62] R. G. Gordon, *MRS Bulletin* **2000**, *25*(08), 52–57, DOI 10.1557/mrs2000.151.
- [63] T. Minami, *Semiconductor Science and Technology* **2005**, *20*(4), S35–S44, DOI 10.1088/0268-1242/20/4/004.
- [64] K. A. Sierros, N. J. Morris, K. Ramji, D. R. Cairns, *Thin Solid Films* **2009**, *517*(8), 2590–2595, DOI 10.1016/j.tsf.2008.10.031.
- [65] H. H. Binder, *Lexikon der chemischen Elemente*, S. Hirzel Verlag, **1999**.
- [66] SMG Indium Resources Ltd., Indium Prices, <http://www.smg-indium.com/Docs/IndiumPriceCharts.pdf>, accessed: 11/29/2012.
- [67] A. Feltrin, A. Freundlich, *Renewable Energy* **2008**, *33*(2), 180–185, DOI 10.1016/j.renene.2007.05.024.

- [68] T. Minami, *Thin Solid Films* **2008**, *516*(17), 5822–5828, DOI 10.1016/j.tsf.2007.10.063.
- [69] H. C. Nguyen, T. T. Trinh, T. Le, C. V. Tran, T. Tran, H. Park, V. A. Dao, J. Yi, *Semiconductor Science and Technology* **2011**, *26*(10), 105022, DOI 10.1088/0268-1242/26/10/105022.
- [70] W. Gaynor, G. F. Burkhard, M. D. McGehee, P. Peumans, *Advanced Materials* **2011**, 2905–2910, DOI 10.1002/adma.201100566.
- [71] M. Fahland, *Vakuum in Forschung und Praxis* **2011**, *23*(2), 30–34, DOI 10.1002/vipr.201100450.
- [72] H. Kim, J. S. Horwitz, G. P. Kushto, Z. H. Kafafi, D. B. Chrisey, *Applied Physics Letters* **2001**, *79*(3), 284, DOI 10.1063/1.1383568.
- [73] D. R. Cairns, R. P. Witte, D. K. Sparacin, S. M. Sachsman, D. C. Paine, G. P. Crawford, R. R. Newton, *Applied Physics Letters* **2000**, *76*(11), 1425, DOI 10.1063/1.126052.
- [74] J.-A. Jeong, H.-K. Kim, *Solar Energy Materials and Solar Cells* **2009**, *93*(10), 1801–1809, DOI 10.1016/j.solmat.2009.06.014.
- [75] S. Schubert, J. Meiss, L. Müller-Meskamp, K. Leo, *Advanced Energy Materials* **2013**, n/a–n/a, DOI 10.1002/aenm.201200903.
- [76] C. Guillén, J. Herrero, *Thin Solid Films* **2011**, *520*(1), 1–17, DOI 10.1016/j.tsf.2011.06.091.
- [77] S. Schubert, M. Hermenau, J. Meiss, L. Müller-Meskamp, K. Leo, *Advanced Functional Materials* **2012**, *22*(23), 4993–4999, DOI 10.1002/adfm.201201592.
- [78] S. Kirchmeyer, K. Reuter, *Journal of Materials Chemistry* **2005**, *15*(21), 2077, DOI 10.1039/b417803n.
- [79] A. Elschner, S. Kirchmeyer, W. Lövenich, U. Merker, K. Reuter, *Pedot: Principles and Applications of an Intrinsically Conductive Polymer*, CRC Press, **2010**.
- [80] Y. H. Kim, C. Sachse, M. L. Machala, C. May, L. Müller-Meskamp, K. Leo, *Advanced Functional Materials* **2011**, *21*, 1076–1081, DOI 10.1002/adfm.201002290.
- [81] Y. Xia, K. Sun, J. Ouyang, *Advanced Materials* **2012**, *24*(18), 2436–40, DOI 10.1002/adma.201104795.
- [82] K. Neyts, M. Marescaux, A. U. Nieto, A. Elschner, W. Lovenich, K. Fehse, Q. Huang, K. Walzer, K. Leo, *Journal of Applied Physics* **2006**, *100*(11).
- [83] R. H. Baughman, A. A. Zakhidov, W. A. de Heer, *Science* **2002**, *297*(5582), 787–92, DOI 10.1126/science.1060928.

- [84] L. Hu, D. S. Hecht, G. Grüner, *Chemical Reviews* **2010**, *110*(10), 5790–844, DOI 10.1021/cr9002962.
- [85] Q. Cao, J. A. Rogers, *Advanced Materials* **2009**, *21*(1), 29–53, DOI 10.1002/adma.200801995.
- [86] Y. H. Kim, L. Müller-Meskamp, A. A. Zakhidov, C. Sachse, J. Meiss, J. Bikova, A. Cook, A. A. Zakhidov, K. Leo, *Solar Energy Materials and Solar Cells* **2012**, *96*(1), 244–250, DOI 10.1016/j.solmat.2011.10.001.
- [87] V. Scardaci, R. Coull, J. N. Coleman, *Applied Physics Letters* **2010**, *97*(2), 023114, DOI 10.1063/1.3462317.
- [88] K. S. Novoselov, A. K. Geim, S. V. Morozov, D. Jiang, Y. Zhang, S. V. Dubonos, I. V. Grigorieva, A. A. Firsov, *Science* **2004**, *306*(5696), 666–9, DOI 10.1126/science.1102896.
- [89] K. S. Novoselov, A. K. Geim, S. V. Morozov, D. Jiang, M. I. Katsnelson, I. V. Grigorieva, S. V. Dubonos, A. A. Firsov, *Nature* **2005**, *438*(7065), 197–200, DOI 10.1038/nature04233.
- [90] N. Peres, F. Guinea, A. Castro Neto, *Physical Review B* **2006**, *73*(12), 1–23, DOI 10.1103/PhysRevB.73.125411.
- [91] S. De, J. N. Coleman, *ACS Nano* **2010**, *4*(5), 2713–20, DOI 10.1021/nn100343f.
- [92] S. Bae, H. Kim, Y. Lee, X. Xu, J.-S. Park, Y. Zheng, J. Balakrishnan, T. Lei, H. R. Kim, Y. I. Song, Y.-J. Kim, K. S. Kim, B. Ozyilmaz, J.-H. Ahn, B. H. Hong, S. Iijima, *Nature Nanotechnology* **2010**, *5*(8), 574–8, DOI 10.1038/nnano.2010.132.
- [93] M.-G. Kang, L. Guo, *Advanced Materials* **2007**, *19*(10), 1391–1396, DOI 10.1002/adma.200700134.
- [94] M.-G. Kang, H. J. Park, S. H. Ahn, L. J. Guo, *Solar Energy Materials and Solar Cells* **2010**, *94*(6), 1179–1184, DOI 10.1016/j.solmat.2010.02.039.
- [95] J. Zou, H.-L. Yip, S. K. Hau, A. K.-Y. Jen, *Applied Physics Letters* **2010**, *96*(20), 203301, DOI 10.1063/1.3394679.
- [96] J.-Y. Lee, S. T. Connor, Y. Cui, P. Peumans, *Nano Letters* **2008**, *8*(2), 689–92, DOI 10.1021/nl073296g.
- [97] L. Müller-Meskamp, C. Sachse, Y. H. Kim, M. Furno, C. May, K. Leo, *Vakuum in Forschung und Praxis* **2012**, *24*(4), 24–31, DOI 10.1002/vipr.201200495.
- [98] H. Wu, L. Hu, M. W. Rowell, D. Kong, J. J. Cha, J. R. McDonough, J. Zhu, Y. Yang, M. D. McGehee, Y. Cui, *Nano Letters* **2010**, *10*(10), 4242–8, DOI 10.1021/nl102725k.

- [99] T. L. Belenkova, D. Rimmerman, E. Mentovich, H. Gilon, N. Hendler, S. Richter, G. Markovich, *Journal of Materials Chemistry* **2012**, *22*(45), 24042, DOI 10.1039/c2jm35291e.
- [100] L. Hu, H. S. Kim, J.-Y. Lee, P. Peumans, Y. Cui, *ACS Nano* **2010**, *4*(5), 2955–2963, DOI 10.1021/nm1005232.
- [101] J. Krantz, M. Richter, S. Spallek, E. Spiecker, C. J. Brabec, *Advanced Functional Materials* **2011**, *21*(24), 4784–4787, DOI 10.1002/adfm.201100457.
- [102] A. R. Rathmell, B. J. Wiley, *Advanced Materials* **2011**, *23*(41), 4798–803, DOI 10.1002/adma.201102284.
- [103] E. C. Garnett, W. Cai, J. J. Cha, F. Mahmood, S. T. Connor, M. Greyson Christoforo, Y. Cui, M. D. McGehee, M. L. Brongersma, *Nature Materials* **2012**, *11*(3), 241–9, DOI 10.1038/nmat3238.
- [104] R. Zhu, C.-H. Chung, K. C. Cha, W. Yang, Y. B. Zheng, H. Zhou, T.-B. Song, C.-C. Chen, P. S. Weiss, G. Li, Y. Yang, *ACS Nano* **2011**, *5*(12), 9877–9882, DOI 10.1021/nm203576v.
- [105] L. Li, Z. Yu, W. Hu, C.-h. Chang, Q. Chen, Q. Pei, *Advanced Materials* **2011**, *23*(46), 5563–7, DOI 10.1002/adma.201103180.
- [106] F. S. F. Morgenstern, D. Kabra, S. Massip, T. J. K. Brenner, P. E. Lyons, J. N. Coleman, R. H. Friend, *Applied Physics Letters* **2011**, *99*(18), 183307, DOI 10.1063/1.3656973.
- [107] X.-Y. Zeng, Q.-K. Zhang, R.-M. Yu, C.-Z. Lu, *Advanced Materials* **2010**, *22*(40), 4484–8, DOI 10.1002/adma.201001811.
- [108] S. Kirkpatrick, *Reviews of Modern Physics* **1973**, *45*(4), 574–588, DOI 10.1103/RevModPhys.45.574.
- [109] Y. Chen, G. Paul, R. Cohen, S. Havlin, S. P. Borgatti, F. Liljeros, H. Eugene Stanley, *Physica A: Statistical Mechanics and its Applications* **2007**, *378*(1), 11–19, DOI 10.1016/j.physa.2006.11.074.
- [110] M. A. Aon, S. Cortassa, B. O'Rourke, *Proceedings of the National Academy of Sciences of the United States of America* **2004**, *101*(13), 4447–52, DOI 10.1073/pnas.0307156101.
- [111] S. Blumberg, O. Frank, T. Hofmann, *Journal of Agricultural and Food Chemistry* **2010**, *58*(6), 3720–8, DOI 10.1021/jf9044606.
- [112] G. Grimmett, *Percolation*, Springer-Verlag, **1999**.
- [113] D. Stauffer, A. Aharony, *Percolationstheorie - Eine Einführung*, VCH Verlagsgesellschaft mbH, **1995**.
- [114] S. R. Broadbent, J. M. Hammersley, *Mathematical Proceedings of the Cambridge Philosophical Society* **1957**, *53*(03), 629, DOI 10.1017/S0305004100032680.

- [115] B. Last, D. Thouless, *Physical Review Letters* **1971**, *27*(25), 1719–1721, DOI 10.1103/PhysRevLett.27.1719.
- [116] I. Balberg, N. Binenbaum, C. Anderson, *Physical Review Letters* **1983**, *51*(18), 1605–1608, DOI 10.1103/PhysRevLett.51.1605.
- [117] Y.-B. Yi, A. M. Sastry, *Physical Review E* **2002**, *66*(6), 066130, DOI 10.1103/PhysRevE.66.066130.
- [118] X. Jing, W. Zhao, L. Lan, *Journal of Materials Science Letters* **2000**, *19*(5), 377–379, DOI 10.1023/A:1006774318019.
- [119] Q. Xue, *European Polymer Journal* **2004**, *40*(2), 323–327, DOI 10.1016/j.eurpolymj.2003.10.011.
- [120] H. S. Göktürk, T. J. Fiske, D. M. Kalyon, *Journal of Applied Polymer Science* **1993**, *50*(11), 1891–1901, DOI 10.1002/app.1993.070501105.
- [121] G. Pike, C. Seager, *Physical Review B* **1974**, *10*(4), 1421–1434, DOI 10.1103/PhysRevB.10.1421.
- [122] X. Zheng, M. G. Forest, R. Vaia, M. Arlen, R. Zhou, *Advanced Materials* **2007**, *19*(22), 4038–4043, DOI 10.1002/adma.200700011.
- [123] I. Balberg, S. Alexander, N. Wagner, *Physical Review B* **1984**, *30*(7), 3933–3943, DOI 10.1103/PhysRevB.30.3933.
- [124] J. Li, S.-L. Zhang, *Physical Review E* **2010**, *81*(2), 1–5, DOI 10.1103/PhysRevE.81.021120.
- [125] S. De, P. J. King, P. E. Lyons, U. Khan, J. N. Coleman, *ACS Nano* **2010**, *4*(12), 7064–72, DOI 10.1021/nn1025803.
- [126] J. Coleman, S. Curran, A. Dalton, A. Davey, B. McCarthy, W. Blau, R. Barklie, *Physical Review B* **1998**, *58*(12), R7492–R7495, DOI 10.1103/PhysRevB.58.R7492.
- [127] L. Hu, D. S. Hecht, G. Grüner, *Nano Letters* **2004**, *4*(12), 2513–2517, DOI 10.1021/nl048435y.
- [128] D. Hecht, L. Hu, G. Grüner, *Applied Physics Letters* **2006**, *89*(13), 133112, DOI 10.1063/1.2356999.
- [129] S. I. White, R. M. Mutiso, P. M. Vora, D. Jahnke, S. Hsu, J. M. Kikkawa, J. Li, J. E. Fischer, K. I. Winey, *Advanced Functional Materials* **2010**, *20*(16), 2709–2716, DOI 10.1002/adfm.201000451.
- [130] S. Sorel, P. E. Lyons, S. De, J. C. Dickerson, J. N. Coleman, *Nanotechnology* **2012**, *23*(18), 185201, DOI 10.1088/0957-4484/23/18/185201.
- [131] H.-Z. Geng, D. S. Lee, K. K. Kim, G. H. Han, H. K. Park, Y. H. Lee, *Chemical Physics Letters* **2008**, *455*(4-6), 275–278, DOI 10.1016/j.cplett.2008.02.102.

- [132] S. De, P. E. Lyons, S. Sorel, E. M. Doherty, P. J. King, W. J. Blau, P. N. Nirmalraj, J. J. Boland, V. Scardaci, J. Joimel, J. N. Coleman, *ACS Nano* **2009**, *3*(3), 714–20, DOI 10.1021/nn800858w.
- [133] D. Natelson, in *Recent Research Developments in Vacuum Science and Technology*, Research Signpost, Kerala, India, **2003**, p. 16.
- [134] S. Barth, F. Hernandez-Ramirez, J. D. Holmes, A. Romano-Rodriguez, *Progress in Materials Science* **2010**, *55*(6), 563–627, DOI 10.1016/j.pmatsci.2010.02.001.
- [135] R. G. Hobbs, N. Petkov, J. D. Holmes, *Chemistry of Materials* **2012**, *24*(11), 1975–1991, DOI 10.1021/cm300570n.
- [136] N. Wang, Y. Cai, R. Zhang, *Materials Science and Engineering: R: Reports* **2008**, *60*(1-6), 1–51, DOI 10.1016/j.mser.2008.01.001.
- [137] E. J. Menke, M. A. Thompson, C. Xiang, L. C. Yang, R. M. Penner, *Nature Materials* **2006**, *5*(11), 914–9, DOI 10.1038/nmat1759.
- [138] D. Natelson, R. L. Willett, K. W. West, L. N. Pfeiffer, *Applied Physics Letters* **2000**, *77*(13), 1991, DOI 10.1063/1.1312256.
- [139] S. H. Ko, I. Park, H. Pan, C. P. Grigoropoulos, A. P. Pisano, C. K. Luscombe, J. M. J. Fréchet, *Nano Letters* **2007**, *7*(7), 1869–77, DOI 10.1021/nl070333v.
- [140] B. Bhushan, *Handbook of Nanotechnology*, 2nd ed., Springer, **2007**.
- [141] R. S. Wagner, W. C. Ellis, *Applied Physics Letters* **1964**, *4*(5), 89, DOI 10.1063/1.1753975.
- [142] P. Liu, Z. Li, B. Zhao, B. Yadian, Y. Zhang, *Materials Letters* **2009**, *63*(20), 1650–1652, DOI 10.1016/j.matlet.2009.04.031.
- [143] K. R. Krishnadas, P. R. Sajanlal, T. Pradeep, *The Journal of Physical Chemistry C* **2011**, *115*(11), 4483–4490, DOI 10.1021/jp110498x.
- [144] J. C. Hulteen, C. R. Martin, *Journal of Materials Chemistry* **1997**, *7*(7), 1075–1087, DOI 10.1039/a700027h.
- [145] S. H. Park, M. W. Prior, T. H. LaBean, G. Finkelstein, *Applied Physics Letters* **2006**, *89*(3), 033901, DOI 10.1063/1.2234282.
- [146] J. Cornelissen, R. van Heerbeek, P. Kamer, J. Reek, N. Sommerdijk, R. Nolte, *Advanced Materials* **2002**, *14*(7), 489–492, DOI 10.1002/1521-4095(20020404)14:7<489::AID-ADMA489>3.0.CO;2-Y.
- [147] Y. Sun, B. Mayers, T. Herricks, Y. Xia, *Nano Letters* **2003**, *3*(7), 955–960, DOI 10.1021/nl034312m.
- [148] B. Wiley, Y. Sun, Y. Xia, *Accounts of Chemical Research* **2007**, *40*(10), 1067–76, DOI 10.1021/ar7000974.

- [149] Y. Sun, B. Gates, B. Mayers, Y. Xia, *Nano Letters* **2002**, *2*(2), 165–168, DOI 10.1021/nl010093y.
- [150] G. Lee, *Materials Chemistry and Physics* **2004**, *84*(2-3), 197–204, DOI 10.1016/j.matchemphys.2003.11.024.
- [151] B. H. Hong, S. C. Bae, C. W. Lee, S. Jeong, K. S. Kim, *Science* **2001**, *294*(5541), 348–51, DOI 10.1126/science.1062126.
- [152] Q. N. Luu, J. M. Doorn, M. T. Berry, C. Jiang, C. Lin, P. S. May, *Journal of Colloid and Interface Science* **2011**, *356*(1), 151–8, DOI 10.1016/j.jcis.2010.12.077.
- [153] L. Y. Zhang, J. Wang, L. M. Wei, P. Liu, H. Wei, Y. F. Zhang, *Nano-Micro Letters* **2010**, *1*(1), 49–52, DOI 10.5101/nml.v1i1.p49-52.
- [154] M. Mohl, P. Pusztai, A. Kukovecz, Z. Konya, J. Kukkola, K. Kordas, R. Vajtai, P. M. Ajayan, *Langmuir* **2010**, *26*(21), 16496–502, DOI 10.1021/la101385e.
- [155] Z. Liu, Y. Yang, J. Liang, Z. Hu, S. Li, S. Peng, Y. Qian, *The Journal of Physical Chemistry B* **2003**, *107*(46), 12658–12661, DOI 10.1021/jp036023s.
- [156] E. Ye, S.-Y. Zhang, S. Liu, M.-Y. Han, *Chemistry* **2011**, *17*(11), 3074–7, DOI 10.1002/chem.201002987.
- [157] Y. Chang, M. L. Lye, H. C. Zeng, *Langmuir : the ACS journal of surfaces and colloids* **2005**, *21*(9), 3746–8, DOI 10.1021/la050220w.
- [158] P. E. Lyons, S. De, J. Elias, M. Schamel, L. Philippe, A. T. Bellew, J. J. Boland, J. N. Coleman, *The Journal of Physical Chemistry Letters* **2011**, *2*(24), 3058–3062, DOI 10.1021/jz201401e.
- [159] D. Azulai, T. Belenkova, H. Gilon, Z. Barkay, G. Markovich, *Nano Letters* **2009**, *9*(12), 4246–9, DOI 10.1021/nl902458j.
- [160] D. Azulai, E. Cohen, G. Markovich, *Nano Letters* **2012**, *12*(11), 5552–8, DOI 10.1021/nl302484n.
- [161] S. M. Bergin, Y.-H. Chen, A. R. Rathmell, P. Charbonneau, Z.-Y. Li, B. J. Wiley, *Nanoscale* **2012**, *4*(6), 1996–2004, DOI 10.1039/c2nr30126a.
- [162] N. W. Ashcroft, N. D. Mermin, *Solid State Physics*, Saunders College Publishing, **1976**.
- [163] R. B. Dingle, *Proceedings of the Royal Society A: Mathematical, Physical and Engineering Sciences* **1950**, *201*(1067), 545–560, DOI 10.1098/rspa.1950.0077.
- [164] B. J. Wiley, Z. Wang, J. Wei, Y. Yin, D. H. Cobden, Y. Xia, *Nano Letters* **2006**, *6*(10), 2273–8, DOI 10.1021/nl061705n.
- [165] A. Bid, A. Bora, A. Raychaudhuri, *Physical Review B* **2006**, *74*(3), 035426, DOI 10.1103/PhysRevB.74.035426.

- [166] A. Graff, D. Wagner, H. Ditlbacher, U. Kreibig, *The European Physical Journal D* **2005**, *34*(1-3), 263–269, DOI 10.1140/epjd/e2005-00108-7.
- [167] Q. Huang, C. M. Lilley, M. Bode, *Applied Physics Letters* **2009**, *95*(10), 103112, DOI 10.1063/1.3216836.
- [168] W. Steinhögl, G. Schindler, G. Steinlesberger, M. Traving, M. Engelhardt, *Journal of Applied Physics* **2005**, *97*(2), 023706, DOI 10.1063/1.1834982.
- [169] Q. Huang, C. M. Lilley, M. Bode, R. Divan, *Journal of Applied Physics* **2008**, *104*(2), 023709, DOI 10.1063/1.2956703.
- [170] W. Steinhögl, G. Schindler, G. Steinlesberger, M. Engelhardt, *Physical Review B* **2002**, *66*(7), 075414, DOI 10.1103/PhysRevB.66.075414.
- [171] H. Marom, J. Mullin, M. Eizenberg, *Physical Review B* **2006**, *74*(4), 045411, DOI 10.1103/PhysRevB.74.045411.
- [172] E. H. Sondheimer, *Advances in Physics* **2001**, *50*(6), 499–537, DOI 10.1080/00018730110102187.
- [173] C. Durkan, M. Welland, *Physical Review B* **2000**, *61*(20), 14215–14218, DOI 10.1103/PhysRevB.61.14215.
- [174] Y. Zhou, S. Sreekala, P. M. Ajayan, S. K. Nayak, *Journal of Physics: Condensed Matter* **2008**, *20*(9), 095209, DOI 10.1088/0953-8984/20/9/095209.
- [175] J. Hu, T. W. Odom, C. M. Lieber, *Accounts of Chemical Research* **1999**, *32*(5), 435–445, DOI 10.1021/ar9700365.
- [176] V. Rodrigues, J. Bettini, A. Rocha, L. Rego, D. Ugarte, *Physical Review B* **2002**, *65*(15), 153402, DOI 10.1103/PhysRevB.65.153402.
- [177] H. A. Atwater, A. Polman, *Nature Materials* **2010**, *9*(3), 205–13, DOI 10.1038/nmat2629.
- [178] G. Mie, *Annalen der Physik* **1908**, *25*(3), 377–445.
- [179] J. van de Groep, P. Spinelli, A. Polman, *Nano Letters* **2012**, *12*(6), 3138–44, DOI 10.1021/nl301045a.
- [180] P. B. Catrysse, S. Fan, *Nano Letters* **2010**, *10*(8), 2944–9, DOI 10.1021/nl1011239.
- [181] S. A. Maier, *Plasmonics - Fundamentals and Applications*, Springer, **2007**.
- [182] C. F. Bohren, D. R. Huffman, *Absorption and Scattering of Light by Small Particles*, Wiley-VCH Verlag GmbH, Weinheim, Germany, **1998**, DOI 10.1002/9783527618156.
- [183] E. Hutter, J. H. Fendler, *Advanced Materials* **2004**, *16*(19), 1685–1706, DOI 10.1002/adma.200400271.

- [184] C. Sönnichsen, doctoral thesis, **2001**.
- [185] R. A. Pala, J. White, E. Barnard, J. Liu, M. L. Brongersma, *Advanced Materials* **2009**, *21*(34), 3504–3509, DOI 10.1002/adma.200900331.
- [186] C. Sönnichsen, T. Franzl, T. Wilk, G. von Plessen, J. Feldmann, *Physical Review Letters* **2002**, *88*(7), 077402, DOI 10.1103/PhysRevLett.88.077402.
- [187] H.-A. Chen, H.-Y. Lin, H.-N. Lin, *The Journal of Physical Chemistry C* **2010**, *114*(23), 10359–10364, DOI 10.1021/jp1014725.
- [188] C.-L. Zou, F.-W. Sun, Y.-F. Xiao, C.-H. Dong, X.-D. Chen, J.-M. Cui, Q. Gong, Z.-F. Han, G.-C. Guo, *Applied Physics Letters* **2010**, *97*(18), 183102, DOI 10.1063/1.3509415.
- [189] P. Ramasamy, D.-M. Seo, S.-H. Kim, J. Kim, *Journal of Materials Chemistry* **2012**, *22*(23), 11651, DOI 10.1039/c2jm00010e.
- [190] K. R. Catchpole, A. Polman, *Applied Physics Letters* **2008**, *93*(19), 191113, DOI 10.1063/1.3021072.
- [191] P. Spinelli, C. van Lare, E. Verhagen, A. Polman, *Optics Express* **2011**, *19 Suppl 3*(May), A303–11, DOI 10.1364/OE.19.00A303.
- [192] J. R. Krenn, G. Schider, W. Rechberger, B. Lamprecht, A. Leitner, F. R. Aussenegg, J. C. Weeber, *Applied Physics Letters* **2000**, *77*(21), 3379, DOI 10.1063/1.1327615.
- [193] G. Schider, J. Krenn, A. Hohenau, H. Ditlbacher, A. Leitner, F. Aussenegg, W. Schaich, I. Puscasu, B. Monacelli, G. Boreman, *Physical Review B* **2003**, *68*(15), 155427, DOI 10.1103/PhysRevB.68.155427.
- [194] Q. Xu, J. Bao, F. Capasso, G. M. Whitesides, *Angewandte Chemie (International ed. in English)* **2006**, *45*(22), 3631–5, DOI 10.1002/anie.200600394.
- [195] J. Kottmann, O. Martin, D. Smith, S. Schultz, *Physical Review B* **2001**, *64*(23), 235402, DOI 10.1103/PhysRevB.64.235402.
- [196] J. Kottmann, O. Martin, *Optics Express* **2001**, *8*(12), 655, DOI 10.1364/OE.8.000655.
- [197] O. J. Glembocki, R. W. Rendell, S. M. Prokes, D. A. Alexson, M. A. Mastro, S. C. Badescu, A. Fu, in *Proceedings of SPIE*, vol. 6768, (Ed. by N. K. Dhar, A. K. Dutta, M. S. Islam), vol. 6768, p. 676802–676802–8, DOI 10.1117/12.751384.
- [198] Y. Wang, Y. Ma, X. Guo, L. Tong, *Optics Express* **2012**, *20*(17), 19006–15, DOI 10.1364/OE.20.019006.
- [199] M. Barbic, J. J. Mock, D. R. Smith, S. Schultz, *Journal of Applied Physics* **2002**, *91*(11), 9341, DOI 10.1063/1.1476071.

- [200] H. Kim, C. Xiang, A. G. Güell, R. M. Penner, E. O. Potma, *Journal of Physical Chemistry C* **2008**, *112*(33), 12721–12727, DOI 10.1021/jp8032758.
- [201] B. J. Wiley, D. J. Lipomi, J. Bao, F. Capasso, G. M. Whitesides, *Nano Letters* **2008**, *8*(9), 3023–3028, DOI 10.1021/nl802252r.
- [202] A. L. Pyayt, B. Wiley, Y. Xia, A. Chen, L. Dalton, *Nature Nanotechnology* **2008**, *3*(11), 660–5, DOI 10.1038/nnano.2008.281.
- [203] G. Schider, J. R. Krenn, W. Gotschy, B. Lamprecht, H. Ditlbacher, A. Leitner, F. R. Aussenegg, *Journal of Applied Physics* **2001**, *90*(8), 3825, DOI 10.1063/1.1404425.
- [204] K. Aydin, V. E. Ferry, R. M. Briggs, H. A. Atwater, *Nature Communications* **2011**, *2*, 517, DOI 10.1038/ncomms1528.
- [205] V. A. Podolskiy, A. K. Sarychev, V. M. Shalaev, *Journal of Nonlinear Optical Physics & Materials* **2002**, *11*(01), 65–74, DOI 10.1142/S0218863502000833.
- [206] V. Podolskiy, A. Sarychev, V. Shalaev, *Optics Express* **2003**, *11*(7), 735, DOI 10.1364/OE.11.000735.
- [207] A. R. Rathmell, S. M. Bergin, Y.-L. Hua, Z.-Y. Li, B. J. Wiley, *Advanced Materials* **2010**, *22*(32), 3558–63, DOI 10.1002/adma.201000775.
- [208] Y. H. Kim, doctoral thesis, TU Dresden, **2013**.
- [209] M. Hermenau, M. Riede, K. Leo, S. A. Gevorgyan, F. C. Krebs, K. Norrman, *Solar Energy Materials and Solar Cells* **2011**, *95*(5), 1268–1277, DOI 10.1016/j.solmat.2011.01.001.
- [210] M. Hermenau, S. Schubert, H. Klumbies, J. Fahlteich, L. Müller-Meskamp, K. Leo, M. Riede, *Solar Energy Materials and Solar Cells* **2012**, *97*, 102–108, DOI 10.1016/j.solmat.2011.09.026.
- [211] D. K. Schroder, *Semiconductor Material and Device Characterization*, 3rd ed., Wiley, **2006**.
- [212] L. J. van der Pauw, *Philips Research Reports* **1958**, *13*, 1–9.
- [213] NIST, Hall Effect Measurements Algorithm, http://www.nist.gov/pml/div683/hall_algorithm.cfm, accessed: 08/29/2013.
- [214] A. Vladimirescu, *The Spice Book*, John Wiley & Sons, Inc., **1994**.
- [215] C. Sachse, L. Müller-Meskamp, L. Bormann, Y. H. Kim, F. Lehnert, A. Philipp, B. Beyer, K. Leo, *Organic Electronics* **2012**, *14*(1), 143–148, DOI 10.1016/j.orgel.2012.09.032.
- [216] Cambrios Technologies Corporation, ClearOhm™ Silver Nanowire Coating Material, <http://www.cambrios.com>.

- [217] P.-M. Allemand, *US20120104374* **2012**.
- [218] R. Deegan, O. Bakajin, T. Dupont, G. Huber, S. Nagel, T. Witten, *Nature* **1997**, *389*(6653), 827–828, DOI 10.1038/39827.
- [219] R. Deegan, O. Bakajin, T. Dupont, G. Huber, S. Nagel, T. Witten, *Physical Review E* **2000**, *62*(1), 756–765, DOI 10.1103/PhysRevE.62.756.
- [220] S. Yang, H. Zhang, M. Nosonovsky, K.-H. Chung, *Langmuir : the ACS journal of surfaces and colloids* **2008**, *24*(3), 743–8, DOI 10.1021/la701900f.
- [221] M. P. Manoharan, M. A. Haque, *Journal of Physics D: Applied Physics* **2009**, *42*(9), 095304, DOI 10.1088/0022-3727/42/9/095304.
- [222] H. Dai, M. Heidecker, B. Ng, *WO2008147431* **2007**.
- [223] L. Landau, B. Levich, *Acta Physicochimica URSS* **1942**, *17*, 42–54.
- [224] R. Krechetnikov, G. M. Homsy, *Journal of Fluid Mechanics* **2006**, *559*, 429, DOI 10.1017/S0022112006000425.
- [225] H. C. Mayer, R. Krechetnikov, *Physics of Fluids* **2012**, *24*(5), 052103, DOI 10.1063/1.4703924.
- [226] J. Snoeijer, J. Ziegler, B. Andreotti, M. Fermigier, J. Eggers, *Physical Review Letters* **2008**, *100*(24), 244502, DOI 10.1103/PhysRevLett.100.244502.
- [227] P. Groenveld, *AIChE Journal* **1971**, *17*(2), 489–490, DOI 10.1002/aic.690170244.
- [228] C. Brinker, A. Hurd, P. Schunk, G. Frye, C. Ashley, *Journal of Non-Crystalline Solids* **1992**, *147-148*, 424–436, DOI 10.1016/S0022-3093(05)80653-2.
- [229] A. Schneider, *Zeitschrift Holz als Roh- und Werkstoff* **1960**, *18*(7), 269–272.
- [230] G. Vazquez, E. Alvarez, J. M. Navaza, *Journal of Chemical & Engineering Data* **1995**, *40*(3), 611–614, DOI 10.1021/je00019a016.
- [231] Z. Lei, H. Wang, R. Zhou, Z. Duan, *Chemical Engineering Journal* **2002**, *87*(2), 149–156, DOI 10.1016/S1385-8947(01)00211-X.
- [232] DDBST GmbH, Dortmund Data Bank, <http://www.ddbst.com/>.
- [233] Online Chemical Engineering Software, Binary Vapor Liquid Equilibrium, <http://www.chemsof.com/vle/vle.htm>, accessed: 09/03/2013.
- [234] C. Häfner, doctoral thesis, TU Dresden, **2012**.
- [235] M. E. Toimil Molares, A. G. Balogh, T. W. Cornelius, R. Neumann, C. Trautmann, *Applied Physics Letters* **2004**, *85*(22), 5337, DOI 10.1063/1.1826237.
- [236] B. V. L'vov, *Thermochimica Acta* **1999**, *333*(1), 13–19, DOI 10.1016/S0040-6031(99)00085-4.

- [237] SpecialChem S.A., PVP T_g , <http://www.specialchem4adhesives.com/tc/polyvinylpyrrolidone/?id=chemistry>, accessed: 07/25/2013.
- [238] L. Bormann, diploma thesis, TU Dresden, **2012**.
- [239] A. A. Zakhidov, J.-K. Lee, H. H. Fong, J. A. DeFranco, M. Chatzichristidi, P. G. Taylor, C. K. Ober, G. G. Malliaras, *Advanced Materials* **2008**, *20*(18), 3481–3484, DOI 10.1002/adma.200800557.
- [240] F. Lehnert, diploma thesis, TU Dresden, **2012**.
- [241] W. Gaynor, S. Hofmann, M. G. Christoforo, C. Sachse, S. Mehra, A. Salleo, M. D. McGehee, M. C. Gather, B. Lüssem, L. Müller-Meskamp, P. Peumans, K. Leo, *Advanced Materials* **2013**, 1–8, DOI 10.1002/adma.201300923.
- [242] D. R. Lide, *CRC handbook of chemistry and physics*, 85th ed., **2004**.
- [243] C. Sachse, N. Weiß, N. Gaponik, L. Müller-Meskamp, A. Eychmüller, K. Leo, *Advanced Energy Materials* **2013**, DOI 10.1002/aenm.201300737.
- [244] NanoForge Corp., <http://www.nanoforge.com/>.
- [245] M. Jin, G. He, H. Zhang, J. Zeng, Z. Xie, Y. Xia, *Angewandte Chemie (International ed. in English)* **2011**, *50*(45), 10560–4, DOI 10.1002/anie.201105539.
- [246] D. Zhang, R. Wang, M. Wen, D. Weng, X. Cui, J. Sun, H. Li, Y. Lu, *Journal of the American Chemical Society* **2012**, *134*(35), 14283–6, DOI 10.1021/ja3050184.
- [247] Y. Zhao, Y. Zhang, Y. Li, Z. He, Z. Yan, *RSC Advances* **2012**, *2*(30), 11544, DOI 10.1039/c2ra21224b.
- [248] Y. Shi, H. Li, L. Chen, X. Huang, *Science and Technology of Advanced Materials* **2005**, *6*(7), 761–765, DOI 10.1016/j.stam.2005.06.008.
- [249] M. Kevin, W. L. Ong, G. H. Lee, G. W. Ho, *Nanotechnology* **2011**, *22*(23), 235701, DOI 10.1088/0957-4484/22/23/235701.
- [250] Z. Lu, J. Goebel, J. Ge, Y. Yin, *Journal of Materials Chemistry* **2009**, *19*(26), 4597, DOI 10.1039/b903637g.
- [251] B. Lefez, K. Kartouni, M. Lenglet, D. Rönnow, C. G. Ribbing, *Surface and Interface Analysis* **1994**, *22*(1-12), 451–455, DOI 10.1002/sia.740220196.
- [252] S. Jeong, K. Woo, D. Kim, S. Lim, J. S. Kim, H. Shin, Y. Xia, J. Moon, *Advanced Functional Materials* **2008**, *18*(5), 679–686, DOI 10.1002/adfm.200700902.
- [253] A. Kamyshny, *The Open Applied Physics Journal* **2011**, *4*(1), 19–36, DOI 10.2174/1874183501104010019.
- [254] F. Meng, S. Jin, *Nano Letters* **2012**, *12*(1), 234–9, DOI 10.1021/nl203385u.
- [255] Y. Kobayashi, S. Ishida, K. Ihara, Y. Yasuda, T. Morita, S. Yamada, *Colloid and Polymer Science* **2009**, *287*(7), 877–880, DOI 10.1007/s00396-009-2047-7.

- [256] H. Wieder, A. W. Czanderna, *Journal of Physical Chemistry* **1962**, *66*(5), 816–821, DOI 10.1021/j100811a010.
- [257] J.-W. Han, A. Lohn, N. P. Kobayashi, M. Meyyappan, *Materials Express* **2011**, *1*(2), 176–180, DOI 10.1166/mex.2011.1022.
- [258] I. N. Kholmanov, S. H. Domingues, H. Chou, X. Wang, C. Tan, J.-Y. Kim, H. Li, R. Piner, A. J. G. Zarbin, R. S. Ruoff, *ACS Nano* **2013**, *7*(2), 1811–6, DOI 10.1021/nm3060175.
- [259] A. R. Rathmell, M. Nguyen, M. Chi, B. J. Wiley, *Nano Letters* **2012**, *12*(6), 3193–9, DOI 10.1021/nl301168r.
- [260] D. Y. Choi, H. W. Kang, H. J. Sung, S. S. Kim, *Nanoscale* **2013**, *5*(3), 977–83, DOI 10.1039/c2nr32221h.
- [261] Z. Hu, J. Zhang, Z. Hao, Y. Zhao, *Solar Energy Materials and Solar Cells* **2011**, *95*(10), 2763–2767, DOI 10.1016/j.solmat.2011.04.040.
- [262] F. C. Krebs, H. Spanggaard, *Chemistry of Materials* **2005**, *17*(21), 5235–5237, DOI 10.1021/cm051320q.
- [263] Y. Lu, R. Ganguli, C. Drewien, M. Anderson, C. Brinker, W. Gong, Y. Guo, H. Soyez, B. Dunn, M. Huang, I. Jeffrey, *Nature* **1997**, *389*(September), 364–368, DOI 10.1038/38699.
- [264] Y. Huang, X. Duan, Q. Wei, C. M. Lieber, *Science* **2001**, *291*(5504), 630–3, DOI 10.1126/science.291.5504.630.
- [265] J. W. Gipps, *Transactions of the Connecticut Academy of Arts and Sciences* **1879**, *3*.
- [266] J. Huang, R. Fan, S. Connor, P. Yang, *Angewandte Chemie (International ed. in English)* **2007**, *46*(14), 2414–7, DOI 10.1002/anie.200604789.
- [267] A. Javey, S. Nam, R. S. Friedman, H. Yan, C. M. Lieber, *Nano Letters* **2007**, *7*(3), 773–7, DOI 10.1021/nl063056l.
- [268] Z. Fan, J. C. Ho, Z. A. Jacobson, R. Yerushalmi, R. L. Alley, H. Razavi, A. Javey, *Nano Letters* **2008**, *8*(1), 20–5, DOI 10.1021/nl071626r.
- [269] R. Yerushalmi, Z. A. Jacobson, J. C. Ho, Z. Fan, A. Javey, *Applied Physics Letters* **2007**, *91*(20), 203104, DOI 10.1063/1.2813618.
- [270] G. Yu, A. Cao, C. M. Lieber, *Nature Nanotechnology* **2007**, *2*(6), 372–7, DOI 10.1038/nnano.2007.150.
- [271] F. Xu, J. W. Durham, B. J. Wiley, Y. Zhu, *ACS Nano* **2011**, *5*(2), 1556–63, DOI 10.1021/nm103183d.
- [272] A. Tao, F. Kim, C. Hess, J. Goldberger, R. He, Y. Sun, Y. Xia, P. Yang, *Nano Letters* **2003**, *3*(9), 1229–1233, DOI 10.1021/nl0344209.

- [273] M. C. Wang, B. D. Gates, *Materials Today* **2009**, *12*(5), 34–43, DOI 10.1016/S1369-7021(09)70158-0.
- [274] E. D. Palik, *Handbook of Optical Constants of Solids*, Academic Press, Boston, **1985**.
- [275] M. Born, E. Wolf, *Principles of Optics*, 12th ed., Cambridge University Press, **1999**.
- [276] N. E. Christensen, *physical status solidi (b)* **1972**, *54*, 551–563.
- [277] H. Ehrenreich, H. R. Philipp, *Physical Review* **1962**, *138*(4), 1622–1629.
- [278] P. Spinelli, M. Hebbink, R. de Waele, L. Black, F. Lenzmann, A. Polman, *Nano Letters* **2011**, *11*(4), 1760–5, DOI 10.1021/nl200321u.
- [279] S. H. Lim, W. Mar, P. Matheu, D. Derkacs, E. T. Yu, *Journal of Applied Physics* **2007**, *101*(10), 104309, DOI 10.1063/1.2733649.
- [280] M.-G. Kang, T. Xu, H. J. Park, X. Luo, L. J. Guo, *Advanced Materials* **2010**, *22*(39), 4378–83, DOI 10.1002/adma.201001395.
- [281] N. Pimparkar, C. Kocabas, J. Rogers, M. Alam, *IEEE Electron Device Letters* **2007**, *28*(7), 593–595, DOI 10.1109/LED.2007.898256.
- [282] J. Hicks, A. Behnam, A. Ural, *Physical Review E* **2009**, *79*(1), 1–4, DOI 10.1103/PhysRevE.79.012102.
- [283] A. Behnam, A. Ural, *Physical Review B* **2007**, *75*(12), 125432, DOI 10.1103/PhysRevB.75.125432.
- [284] F. Du, J. Fischer, K. Winey, *Physical Review B* **2005**, *72*(12), 1–4, DOI 10.1103/PhysRevB.72.121404.
- [285] L. J. Lanticse, Y. Tanabe, K. Matsui, Y. Kaburagi, K. Suda, M. Hoteida, M. Endo, E. Yasuda, *Carbon* **2006**, *44*(14), 3078–3086, DOI 10.1016/j.carbon.2006.05.008.
- [286] S. Phadke, J.-Y. Lee, J. West, P. Peumans, A. Salleo, *Advanced Functional Materials* **2011**, *21*(24), 4691–4697, DOI 10.1002/adfm.201100873.
- [287] I. Balberg, N. Binenbaum, *Physical Review B* **1983**, *28*(7), 3799–3812, DOI 10.1103/PhysRevB.28.3799.
- [288] A. Behnam, J. Guo, A. Ural, *Journal of Applied Physics* **2007**, *102*(4), 044313, DOI 10.1063/1.2769953.
- [289] M. A. Topinka, M. W. Rowell, D. Goldhaber-Gordon, M. D. McGehee, D. S. Hecht, G. Gruner, *Nano Letters* **2009**, *9*(5), 1866–71, DOI 10.1021/nl803849e.

List of Abbreviations and Symbols

α	absorption coefficient
β	cluster exponent for percolation systems
η	solar cell efficiency OR viscosity of the NW dispersion
γ	surface tension of the solvent
λ	wavelength
μ	charge carrier mobility OR conductivity exponent for percolation systems
Φ	work function OR alignment angle
Π	figure of merit for transparent conductive percolation networks
ρ	electrical resistivity OR density of the NW solvent
ρ_{bulk}	resistivity of bulk material
ρ_{wire}	resistivity of single nanowire
σ	electrical conductivity
σ_{bulk}	conductivity of bulk material
φ	barrier at metal-semiconductor interface
A	optical absorption
A_{abs}	absorbance
C	correction factor for van-der-Pauw method
D	diffusion constant
d	nanowire layer thickness
$D_e(E)$	density of states
d_m	metal structure thickness
E	energy
e	elementary charge
E_C	conduction band
E_F	Fermi energy
E_g	energy gap
E_V	valence band
$E_{F,V}/E_{F,C}$	quasi-Fermi level for holes/ electrons
EQE	external quantum efficiency
F	electrical field
f	critical percolation factor
FF	fill factor
g	gravity
h	liquid film thickness
I	electrical current OR light intensity
j	electrical current density

J_0	saturation current
J_{ph}	photo current
j_{sc}	short circuit current density
k	extinction coefficient (imaginary part of the refractive index)
k_B	Boltzmann constant
L	network film dimensions
l	nanowire length
l_{emfp}	electron mean free path
l_c	critical dimension regarding surface scattering
N	percolation object (nanowire) density
n	charge carrier density OR refractive index (real part)
n_1	ideality factor
N_C/N_V	effective density of states in the conduction/ valence band
n_w	nanowire density
N_c	critical percolation density
n_i	intrinsic charge carrier density
P	percolation strength
p	percolation propability OR charge carrier density (holes)
p_c	percolation threshold
q	electron scattering strength at nanowire surface
R	electrical resistance
r	recombination constant OR nanowire radius
R_j	junction resitance
R_p	shunt resistance
R_s	series resistance
R_w	wire resistance
$R_{ }$	(sheet) resistance measured parallel to alignment
R_{\perp}	(sheet) resistance measured perpendicular to alignment
R_{diff}	diffuse reflectance
R_{random}	resistance for random nanowire distributions
R_{spec}	specular reflectance
R_{total}	total reflectance
R_{sh}	sheet resistance
S_n/T_n	energy state (singlet/ triplet)
Sat	saturation factor
SR	spectral response
T	temperature OR optical transmittance
t	time
T_{diff}	diffuse transmittance
T_{spec}	specular transmittance
T_{total}	total transmittance
V	voltage
v	vibronic mode
v_{pull}	pull velocity for dip-coating process
V_{oc}	open circuit voltage
4PP	four point probe resistivity stand

AFM	atomic force microscopy
Ag	silver
AgNW	silver nanowire
Al	aluminum
BF-DPB	N,N'-((diphenyl-N,N'-bis)9,9,-dimethyl-fluoren-2-yl)-benzidine
BHJ	bulk heterojunction
BN	Bluenano Inc.
BPhen	4,7-diphenyl-1,10-phenanthroline
CNT	carbon nanotubes
Cu	copper
CuNW	copper nanowire
DI	deionized water
EA	electron affinity
EG	ethylene glycol
emfp	electron mean free path
ETL	electron transport layer
F ₄ ZnPc	tetrafluoro-zinc-phthalocyanine
F6-TCNNQ	2,2'-(perfluoronaphthalene-2,6-diyldiene)dimalononitrile
FoM	figure of merit
HOMO	highest occupied molecular orbital
HTL	hole transport layer
IP	ionization potention
ITO	indium tin oxide
LSPR	localized surface plasmon resonance
LUMO	lowest unoccupied molecular orbital
NW	nanowire
OSC	organic solar cell
PEDOT:PSS	poly(styrenesulfonate) doped poly(3,4-ethylenedioxythiophene)
PVA	polyvinyl alcohol
PVP	polyvinylpyrrolidone
RMS	root mean square
RT	room temperature
SC	semiconductor
SEM	scanning electron microscopy
SPP	surface plasmon polariton
TCO	transparent conductive oxide
TE	transverse electric
TEM	transmission electron microscopy
TM	transverse magnetic
ZnPc	zinc-phthalocyanine

Danksagung

Diese Arbeit wäre ohne die Unterstützung zahlreicher Personen nicht möglich gewesen. Im Folgenden möchte ich mich bei diesen bedanken und entschuldige mich falls ich einige unberechtigter Weise vergessen sollte.

Der erste Danke gebührt an dieser Stelle natürlich dem Vater dieser Arbeit und Erstgutachter, Professor Karl Leo. Das mir angebotene Thema war sowohl ob seiner Aktualität als auch seiner Vielseitigkeit interessant. Außerdem möchte ich die experimentelle Infrastruktur und die freundliche Atmosphäre am IAPP hervorheben, die das Arbeiten stets sehr angenehm gemacht haben.

Professor Alexander Eychmüller danke ich für die enge Kooperation mit seiner Gruppe in gemeinsamen Projekten und abseits davon. Weiterhin für das zur Verfügung stellen zahlreicher Geräte und die Übernahme des Zweitgutachtens. Ein Dankeschön auch an alle Mitarbeiter des Insituts für Physikalische Chemie für die unkomplizierte Hilfe, im Besonderen:

- Dr. Nelli Weiß, für die Kooperation im Projekt 'ZIM NEOS' für die Synthese der Nanodrähte, für die Erstellung von REM, TEM, XRD und FTIR Messungen, für Rat zu chemischen Fragen und für die Unterstützung bei der Charakterisierung bzw. Nachprozessierung der Elektroden
- Andreas Wolf, für seine Synthesearbeit an Nickel Nanodrähten
- Anne-Kristin Herrmann, für die chemischen Unterstützung am Anfang meiner Arbeit und für den Einsatz an 2D Silber-Paladium Netzwerken
- Paul Mundra, für hilfreiche Tips und Unterstützung bei ersten Versuchen zur Sprüh- und Tauchbeschichtung
- Susanne Goldberg und Ellen Kern für die teils kurzfristigen REM Aufnahmen.

Meinem Arbeitsgruppenleiter Dr. Lars Müller-Meskamp danke ich für die nette Betreuung, hilfreiche Tipps und Korrekturarbeit an dieser und an anderen Schriften. Das Gruppenklima war stets perfekt und ich bin dankbar Teil von E&E gewesen zu sein. In diesem Sinne auch vielen Dank an alle Gruppenmitglieder für die unterhaltsamen,

diskussionsfreudigen, familiären und lehrreichen Meetings, die vielen tollen Gruppenabende und die hilfsbereite Atmosphäre.

- Michael Machala, im Besonderen für die Begleitung in den ersten 6 Monaten und die zahlreichen Diskussionen auch abseits des Insituts
- Dr. Yong Hyun Kim, im Besonderen für die vielen Diskussionen zum und abseits des Elektrodenthemas und für Einblicke in die koreanischen Kultur
- Ludwig Bormann, im Besonderen für seine langjährige Begleitung während seiner Beleg, SHK, Diplom und Doktoranden-Zeit in der er ständig als Unterstützer zur Stelle war
- Fritz Lehnert, im Besonderen für seine Arbeiten zur Integration von Nanodraht Elektroden in OLEDs
- Carsten Häfner, im Besonderen für seine Arbeiten am Sprühroboter
- Sascha Ulbrich, im Besonderen für seine unterstützende Tätigkeit als SHK

Daneben auch ein Danke an die anderen Arbeitsgruppen des IAPP ohne die kein organisches Bauelement je zustandegekommen wäre.

- Dr. Christiane Falkenberg, im Besonderen für die häufige Unterstützung am UFOI und Nanoscope AFM
- Merve Anderson, im Besonderen für XPS Messungen
- Dr. Moritz Riede, im Besonderen für seinen unermüdlichen Einsatz für Regenerative Energien
- Dr. Simone Hofmann und Dr. Michael Thomschke, im Besonderen für das Knowhow im OLED Bereich und die Hilfe bei der Betreuung von Gastwissenschaftlern und Diplomanden
- Prof. Vadim Lyssenko und Dr. Rene Kullock, im Besonderen für die Unterstützung im Reich der Optik

Ich bedanke mich bei Tina und Annette für die Bereitstellung der Materialien, Daniel für die Betreuung der Werkstatt und dem Lesker-Team für die Herstellung der stets funktionstüchtigen ;o) Bauelemente. Besonderer Danke für die Nachsicht bei den häufigen kurzfristigen Änderungen im Ablaufplan. Weiterhin danke ich Kai Schmidt und Peter Leumer für die Pflege der IT ohne die ja heute nix mehr geht. Ich danke den Technikern Sven Kunze und Carsten Wolf für den Einsatz bei der Equipmentpflege und für Hilfe beim experimentellen Umsetzen von Ideen. Natürlich gab es neben den experimentellen auch bürokratische Fragestellung für deren Beantwortung danke ich Annette P., Annette W., Johanna, Julia, Christian, Fr. Hunger und Fr. Schmidt.

Ich danke meinen Bürokollegen (Carsten W., Merve, Yong Hyun, Rico, Paul, Max und Sven, Max und Peter) der BEY 127a, die sich mit mir das Technikerbüro und den Balkon teilten. Sven auch ein Dank für die Hartnäckigkeit bei der Organisation von zahlreichen ‘Meetings‘.

Der 12:30 Uhr Alte-Mensagruppe mit Fredi, Ludwig, Sven, Merve, Micha, Schobi, Sebastian, Daniel gebührt großer Dank. Wie am Institut gab es auch hier einen steten personellen Wandel, aber dennoch war ein unterhaltsames und vor allem langsames Essen immer möglich! Danke für das bereitchaftliche Warten!!!! Nach einem guten Essen darf ein Kaffee nicht fehlen. Deshalb ein Dank an die Personen der Kaffeefrastruktur und Fredi für die Coffee-Initiative.

Ich bedanke mich auch bei allen Kooperationspartnern und institutsfremden Unterstützern.

- Hr. Schrade und Hr. Schulz vom Institut für Textilmaschinen für TU Dresden, im Besonderen für Nutzung der Laborpresse
- André Philipp, Richard Pfeiffer und Beatrice Beyer vom Fraunhofer COMEDD, im Besonderen für die Strukturierungsexperimente, einige Messungen und zahlreiche Diskussionen
- Dr. Daniel Ernst vom IAVT der TU Dresden, im Besonderen für seine Expertise zum Sprühbeschichten
- Dr. Whitney Gaynor von der Stanford University, im Besonderen für die Kooperation und Einblicke in ihre Nanodraht-Forschung
- Dr. Benedikt Gburek von der Heliatek GmbH, im Besonderen für die Kooperation und Wissensaustausch im Projekt ‘ZIM NEOS‘

Zum Schluss noch mein Dank für die mentale Unterstützung an Freunde und Familie, die, obwohl nicht direkt beteiligt, oftmals sehr nah dran waren an Erfolg und Misserfolg ;o) An dieser Stelle sei auch die Hilfe bei der Korrektur meiner Arbeit erwähnt, im Besonderen Annelen, Michael und die liebe Gitti.

Obwohl schon zuvor genannt, möchte ich an dieser Stelle noch einmal Beatrice hervorheben. Von der experimentellen Messung, über Schreibunterstützung und Korrekturrunden bis zur neutralen fachlichen Meinung war sie stets zur Stelle. Toll, dass es dich gibt!